



Trawl-Door Shape Optimization Using Space-Mapping-Enhanced Kriging Surrogates

Ingi Mar Jónsson

Thesis of 60 ETCS credits

Master of Science in Mechanical Engineering

January 2016

This work was supported by the Orkusjóður of Orkustofnun under grant 14-2013.



Trawl-Door Shape Optimization Using Space-Mapping-Enhanced Kriging Surrogates

Ingi Mar Jónsson

Thesis of 60 ECTS credits submitted to the School of Science and Engineering
at Reykjavík University in partial fulfillment of
the requirements for the degree of
Master of Science in Mechanical Engineering

January 2016

Copyright
Ingi Mar Jónsson
January 2016

Trawl-Door Shape Optimization Using Space-Mapping-Enhanced Kriging Surrogates

Ingi Mar Jónsson

60 ECTS thesis submitted to the School of Science and Engineering
at Reykjavík University in partial fulfillment
of the requirements for the degree of
Master of Science in Mechanical Engineering.

January 2016

Student:

Ingi Mar Jónsson

Supervisors:

Leifur Þór Leifsson

Slawomir Koziel

Examiner:

Hlynur Stefánsson

The undersigned hereby grants permission to the Reykjavík University Library to reproduce single copies of this project report entitled **Trawl-Door Shape Optimization Using Space-Mapping-Enhanced Kriging Surrogates** and to lend or sell such copies for private, scholarly or scientific research purposes only.

The author reserves all other publication and other rights in association with the copyright in the project report, and except as herein before provided, neither the project report nor any substantial portion thereof may be printed or otherwise reproduced in any material form whatsoever without the author's prior written permission.

Date

Ingi Mar Jónsson
Master of Science

Trawl-Door Shape Optimization Using Space-Mapping-Enhanced Kriging Surrogates

Ingi Mar Jónsson

January 2016

Abstract

Trawl-doors are one of the main contributors of resistance produced by trawlers fishing gear, that has considerable effects on fuel consumption. A key factor in reducing that consumption is by implementing computational models in the design process. This study presents a robust two dimensional computational fluid dynamics models, that are able to capture the non-linear flow past multi-element hydrofoils. Efficient optimization algorithms are applied to the design of trawl-doors, using problem formulation that captures true characteristics of the design space where lift-to-drag ratio is maximized. Four to seven design variables are used in the optimization process depending on the model, they control angle of attack, position and orientation of a slat or slat and flap. The optimization process involves both multi-point space mapping, and mixed modelling techniques that utilizes space mapping to create a physics-based surrogate model. The results demonstrate that lift-to-drag maximization is more appropriate than lift-constraint drag minimization and that local search using multi-point space mapping can yield satisfactory design at low computational cost. By using Global search with mixed modelling a solution with higher quality will be obtained, but it is not as computationally efficient as multi-point space mapping

Bestun á lögun toghlera með rýmis-vörpuðum Kriging líkönum

Ingi Mar Jónsson

Janúar 2016

Útdráttur

Toghlerar eru einn af þeim meigin þáttum sem hafa áhrif á mótstöðu í veiðarfærum togara, og hafa þeir því talsverð áhrif á eldsneytiseiðslu þeirra. Lykilþáttur í að draga úr eldsneytiseyðslunni er að innleiða straumfræðileg tölvulíkön í hönnunarferlið. Í þessari ritgerð eru kynnt traust tvívíð tölvulíkön sem eru næm á ólínuleika í streymi yfir samsett vængsnið. Skilvirkum bestunar algrímum er beitt við hönnun á toghlerum, þar sem hönnunar forsendan er bætt hlutfall á milli lyfti- og mótstöðu stuðuls. Notast er við fjórar til sjö hönnunarbreytur í bestunar ferlinu eftir því hvaða lögun verið er að skoða, þar sem breyturnar stjórna aðfallshorni, staðsetningu og halla á slatta og/eða flappa. Við bestunarferlið er notast við fjölpunkta svæðis kortlagningu, og samsett líkan sem einnig notast við svæðis kortlagningu við gerð staðgöngu líkans. Niðurstöðurnar sýna fram á að bestun þar sem markmiðið er að hámarka hlutfallið á milli lyfti- og mótstöðu stuðuls á betur við en að lágmarka mótstöðu með skorður á lyfti stuðli ásamt því að aðferð fjölpunkta svæðis kortlagningar skilar ásættanlegum niðurstöðum mjög skilvirkt ef litið er til reiknitíma. Með blandaða líkaninu náðist hinsvegar betri lausn á vandamálinu, en ekki með jafn skilvirkum hætti og fyrri aðferð.

Acknowledgements

I would like to thank my supervisors Leifur Þór Leifsson and Slawomir Koziel, for their support and giving me the opportunity to take part in this research. I would also like to thank Yonatan Afework Tesfahunegn for his help on computer related issues. This work was supported by the Orkusjóður of Orkustofnun under grant 14-2013

Publications

Part of the material in this thesis was published by Procedia Computer Science, in relation to International Conference on Computational Science (ICCS)

- I. Jonsson, L. Leifsson, S. Koziel, Y. Tesfahunegn and A. Bekasiewicz, “Shape Optimization of Trawl-Doors Using Variable Fidelity Models and Space Mapping,” *Procedia Computer Science*, vol. 51, pp. 905-913, 2015.
- [ACCEPTED] I. Jonsson, L. Leifsson, S. Koziel and Y. Tesfahunegn, “Trawl-Door Shape Optimization by Space-Mapping-Corrected CFD Models and Kriging Surrogates,” *Procedia Computer Science*, 2016.

Contents

List of Figures	xi
List of Tables	xvii
List of Abbreviations	xix
List of Symbols	xxi
1 Introduction	1
1.1 Motivation and Background	1
1.2 Research Objectives and Contributions	3
1.3 Thesis Outline	4
2 Problem Formulation	5
3 Computational Fluid Dynamics Modeling	7
3.1 Governing Equations	7
3.2 Flow Solver	9
3.3 Computational Grid	9
3.4 Convergence Study	10
3.5 Validation	16
3.6 Numerical Noise Analysis	23
3.7 Sensitivity Analysis	27
4 Optimization Methodology	29
4.1 Formulation of the Optimization Problem	29
4.2 Surrogate-Based Optimization	30
4.3 Surrogate Modeling	31
4.3.1 Approximation-Based Surrogates	31
4.3.2 Physics-Based Surrogates	32

4.4	Approximation-Based Surrogates via Kriging Interpolation	34
4.5	Physics-Based Surrogates via Multi-Point Space Mapping	36
4.6	Surrogates via Mixed Modeling	38
5	Results	39
5.1	Local Search Using Multi-Point Space Mapping	39
5.1.1	Lift-Constrained Drag Minimization with Main Element and Leading-Edge Slat	39
5.1.2	Lift-to-Drag Maximization with Main Element and Leading-Edge Slat	44
5.1.3	Lift-to-Drag Maximization With Main Element, Leading Edge Slat, and Trailing-Edge Flap	48
5.2	Global Search Using Mixed Modeling	52
5.2.1	Lift-to-Drag Maximization With Main Element and Leading-Edge Slat	52
5.3	Discussion	57
6	Conclusion	59
	Appendices	65
A	Initial Optimization Results Using Multi-Point Space Mapping	67
A.1	Main Element With Trailing Edge Flap	67
A.2	Main Element With Trailing Edge Flap Using Multi-step Approach	72
A.3	Main Element With Leading Edge Slat	80
A.4	Main Element with Leading Edge Slat Using Multi-Step Approach	84
B	Grid Convergence Studies	91
B.1	Main Element and Trailing Edge Flap	91
B.2	Main Element With Leading Edge Slat and Trailing Edge Flap	95
C	Noise Analysis	99
D	Additional Validation Data	107
D.1	Model NASA A L1N1WT	107

List of Figures

1.1	Typical assembly of trawlers fishing gear	2
1.2	Typical trawl-door manufactured from highly cambered steel plates . . .	2
2.1	Two dimensional view of multi-element trawl-door constructed from air-foil shaped elements	5
3.1	Configuration of the solution domain and boundary conditions. The leading edge of the trawl-door main element is located in the centre, and the box is extended 100 chord lengths c in all directions.	10
3.2	Example grid for multi-element trawl-door with leading edge slat and trailing edge flap	11
3.3	Convergence of lift coefficient C_l for ten grids with variable density . . .	12
3.4	Convergence of drag coefficient C_d for ten grids with variable density . .	12
3.5	Solution residuals for ten grids used in the grid convergence study	13
3.6	Trawl-door geometry used for the grid convergence study	14
3.7	Grid convergence study for a trawl-door with uncertainty estimation . . .	15
3.8	Computational time as a function of grid density	16
3.9	Model validation for NACA 0012 airfoil at $Re = 3.0e6$ showing C_l as a function of α . The red line represents the lift slope according to the Thin Airfoil Theory. The blue dots represent the CFD data and the black triangles are wind tunnel data obtained by Abbott et.al. [1]. The magenta boxes represent the Ladson data where the boundary layer transition were fixed at $0.05c$ [2].	17
3.10	Difference in lift coefficient symmetry about $\alpha = 0$ and $C_l = 0$ for NACA 0012 airfoil at $Re = 3.0e6$. The red circles represents CFD data for $\alpha \leq 0$, while the black circles represent data for $\alpha \geq 0$	18

3.11	Model validation drag polar for NACA 0012 airfoil at $Re = 3.0e6$. The blue dots represent the CFD data and the black triangles are wind tunnel data obtained by Abbott et.al. [1]. The magenta boxes represent the Ladson data where the boundary layer transition were fixed at $0.05 c$ [2]. The red triangle is an estimation of C_d over a flat plate at $\alpha = 0$	19
3.12	Geometry of NASA Model B N1WC1F1 airfoil used for the validation process	20
3.13	C_l as a function of α comparison between experimental data using NASA Model B N1WC1F1 airfoil and the CFD model	20
3.14	Drag polar plot comparison between experimental data of NASA Model B N1WC1F1 airfoil and the CFD model	21
3.15	Comparison between experimental data and the CFD model on pressure coefficient C_p over surface of a NASA Model B N1WC1F1 airfoil, consisting of a main element and a flap at three angles of attack	22
3.16	Low-fidelity model computational time example, obtained in the noise analysis process	24
3.17	Noise in lift-to-drag ratio of the low-fidelity model chosen for the optimization process	25
3.18	Noise in lift-to-drag ratio of the high-fidelity model chosen for the optimization process	26
3.19	Sensitivity in design variables of a low-fidelity model at various grid densities	28
4.1	SBO work flow. [3]	31
4.2	Approximation-based surrogate model construction flowchart [3]	32
4.3	Popular design of experiments techniques [3].	33
4.4	Simplified Pattern Search Optimization process [3]	35
5.1	Comparison of initial and optimized trawl-door shape of a trawl-door with main element and leading edge slat. The objective is to minimize C_d subject to constraint on the section lift coefficient using multi-point space mapping. The flow is parallel to the x/c axis	41
5.2	Optimization history of a trawl-door with main element and a leading edge slat. The objective is to minimize C_d subject to constraint on the section lift coefficient using multi-point space mapping.	41

5.3	Flow velocity contour plots for initial and optimized wing configurations of a trawl-door with main element and leading edge slat. The objective is to minimize C_d subject to constraint on the section lift coefficient using multi-point space mapping.	42
5.4	Pressure distribution comparison between initial and optimized shapes of a trawl-door with main element and leading-edge slat. The objective is to minimize C_d subject to constraint on the section lift coefficient using multi-point space mapping.	42
5.5	Comparison of initial and optimized trawl-door shape of a trawl-door with main element and leading edge slat. The objective is to maximize C_l/C_d with no additional constraints, using multi-point space mapping. The flow is parallel to the x/c axis	45
5.6	Lift-to-Drag optimization history of a trawl-door with main element and leading-edge slat. The objective is to maximize C_l/C_d with no additional constraints, using multi-point space mapping.	46
5.7	Flow velocity contour plots for initial and optimized wing configurations of a trawl-door with main element and leading-edge slat. The objective is to maximize C_l/C_d with no additional constraints, using multi-point space mapping.	47
5.8	Pressure distribution comparison between initial and optimized shapes of a trawl-door with main element and leading-edge slat. The objective is to maximize C_l/C_d with no additional constraints, using multi-point space mapping.	47
5.9	Comparison of initial and optimized trawl-door shape of a trawl-door with main element, leading edge slat and trailing edge flap. The objective is to maximize C_l/C_d with no additional constraints, using multi-point space mapping. The flow is parallel to the x/c axis	49
5.10	Lift-to-Drag optimization history of a trawl-door with main element, leading-edge slat and trailing edge flap. The objective is to maximize C_l/C_d with no additional constraints, using multi-point space mapping.	50
5.11	Pressure distribution comparison between initial and optimized shapes of a trawl-door with main element, leading-edge slat and trailing edge flap. The objective is to maximize C_l/C_d with no additional constraints, using multi-point space mapping.	51
5.12	Slice parallel to the $x_{slat}/c, y_{slat}/c$ surface of the Kriging model at optimum location of $\theta = 20.5$ and $\alpha = 10.7$	53

5.13	Slices parallel to the $x_{slat}/c, y_{slat}/c$ surface of the Kriging model at proximity of optimum design of θ and α	54
5.14	Optimized trawl-door shape of a trawl-door with main element and leading edge slat. The objective is to maximize C_l/C_d with no additional constraints, using mixed modeling. The flow is parallel to the x/c axis	55
5.15	Pressure distribution over optimized shape of trawl-door with main element and leading-edge slat. The objective is to maximize C_l/C_d with no additional constraints, using mixed modeling.	55
5.16	Velocity contour plot of the optimized design of trawl-door with main element and leading-edge slat. The objective is to maximize C_l/C_d with no additional constraints, using mixed modeling.	56
A.1	Comparison of initial and optimized trawl-door shape of a trawl-door with main element and leading edge slat. The objective is to maximize C_l/C_d with no additional constraints, using multi-point space mapping. The flow is parallel to the x/c axis	69
A.2	Lift-to-Drag optimization history of a trawl-door with main element and trailing-edge flap. The objective is to maximize C_l/C_d with no additional constraints, using multi-point space mapping.	69
A.3	Velocity contour comparison between the initial and optimized design of a trawl-door shape with main element and a trailing edge flap	70
A.4	Pressure distribution comparison between initial and optimized shapes of a trawl-door with main element and trailing edge flap. The objective is to maximize C_l/C_d with no additional constraints, using multi-point space mapping.	71
A.5	Comparison of initial and optimized trawl-door shape of a trawl-door with main element and trailing edge flap. The objective is to maximize C_l/C_d with no additional constraints, using multi-point space mapping. The flow is parallel to the x/c axis	74
A.6	Lift-to-Drag optimization history of a trawl-door with main element and leading-edge slat. The objective is to maximize C_l/C_d with no additional constraints, using multi-point space mapping.	75
A.7	Velocity contour comparison between the initial and optimized designs of each step in sequential approach.	76
A.8	Pressure distribution comparison between initial and optimized shapes of a trawl-door with main element and trailing edge flap. The objective is to maximize C_l/C_d with no additional constraints, using multi-point space mapping.	77

A.9	Optimizers path for step 1 using multi-step approach	79
A.10	C_l/C_d performance as a function of angle of attack for the optimized trawl-door geometries with main element and trailing edge flap	79
A.11	Comparison of initial and optimized trawl-door shape of a trawl-door with main element with leading edge slat. The objective is to maximize C_l/C_d with no additional constraints, using multi-point space mapping. The flow is parallel to the x/c axis	81
A.12	Lift-to-Drag optimization history of a trawl-door with main element and leading-edge slat. The objective is to maximize C_l/C_d with no additional constraints, using multi-point space mapping.	82
A.13	Pressure distribution comparison between initial and optimized shapes of a trawl-door with main element and leading-edge slat. The objective is to maximize C_l/C_d with no additional constraints, using multi-point space mapping.	83
A.14	Comparison of initial and optimized trawl-door shape of a trawl-door with main element and leading edge slat. The objective is to maximize C_l/C_d with no additional constraints, using multi-point space mapping. The flow is parallel to the x/c axis	86
A.15	Lift-to-Drag optimization history of a trawl-door with main element and leading-edge slat. The objective is to maximize C_l/C_d with no additional constraints, using multi-point space mapping.	87
A.16	Pressure distribution comparison between initial and optimized shapes of a trawl-door with main element and leading-edge slat. The objective is to maximize C_l/C_d with no additional constraints, using multi-point space mapping.	88
A.17	Lift-to-drag contour plot obtained by the low fidelity model	89
A.18	C_l/C_d performance as a function of angle of attack for the optimized trawl-door geometries with main element and leading edge slat	90
B.1	Convergence of lift coefficient C_l for ten grids with variable density . . .	92
B.2	Convergence of lift coefficient C_d for ten grids with variable density . . .	92
B.3	Solution residuals for ten grids used in the grid convergence study . . .	93
B.4	Grid convergence study for a trawl-door with uncertainty estimation . . .	93
B.5	Computational time as a function of grid density	94
B.6	Convergence of lift coefficient C_l for ten grids with variable density . . .	95
B.7	Convergence of lift coefficient C_d for ten grids with variable density . . .	96
B.8	Solution residuals for ten grids used in the grid convergence study . . .	96
B.9	Grid convergence study for a trawl-door with uncertainty estimation . . .	97

B.10	Computational time as a function of grid density	97
C.1	Noise in design variable x/c of the low fidelity model at different grid discretization, the model is considered converged after 1500 iterations or when residuals have reached $5e-3$	99
C.2	Noise in design variable y/c of the low fidelity model at different grid discretization, the model is considered converged after 1500 iterations or when residuals have reached $5e-3$	100
C.3	Noise in design variable θ of the low fidelity model at different grid discretization, the model is considered converged after 1500 iterations or when residuals have reached $5e-3$	101
C.4	Noise in design variable α of the low fidelity model at different grid discretization, the model is considered converged after 1500 iterations or when residuals have reached $5e-3$	102
C.5	Noise in design variable x/c of the low fidelity model at different grid discretization, the model is considered converged after 2.000 iterations or when residuals have reached $5e-4$	103
C.6	Noise in design variable y/c of the low fidelity model at different grid discretization, the model is considered converged after 2.000 iterations or when residuals have reached $5e-4$	104
C.7	Noise in design variable θ of the low fidelity model at different grid discretization, the model is considered converged after 2.000 iterations or when residuals have reached $5e-4$	105
C.8	Noise in design variable α of the low fidelity model at different grid discretization, the model is considered converged after 2.000 iterations or when residuals have reached $5e-4$	106
D.1	Geometry of NASA Model A L1N1WT airfoil used for the validation . .	107
D.2	C_l as a function of α comparison between experimental data using NASA Model A L1N1WT airfoil and the CFD model	108
D.3	Drag polar plot comparison between experimental data of NASA Model A L1N1WT airfoil and the CFD model	108
D.4	Comparison between experimental data and the CFD model on pressure coefficient C_p over surface of a NASA Model A L1N1WT airfoil, consisting of a main element and slat at three angles of attack	109

List of Tables

3.1	Results of the grid convergence study for variables C_l and C_d , uncertainty estimation and conversion ratio for all grid triplets	15
3.2	Estimated noise in C_l/C_d for each design variable of a low-fidelity model	24
5.1	Comparison of initial and optimized results of a trawl-door with a main element and leading edge slat. The objective is to minimize C_d subject to constraint on the section lift coefficient using multi-point space mapping .	40
5.2	Comparison of SM optimization results with approach using local surrogates	43
5.3	Comparison of initial and optimized results of a trawl-door with a main element and leading edge slat. The objective is to maximize C_l/C_d with no additional constraints using multi-point space mapping	45
5.4	Comparison of initial and optimized results of a trawl-door with a main element, leading edge slat and trailing edge flap. The objective is to maximize C_l/C_d with no additional constraints using multi-point space mapping	49
5.5	Optimized results of a trawl-door with a main element and leading edge slat. The objective is to maximize C_l/C_d with no additional constraints using mixed modeling	54
5.6	Comparison of all optimum designs of a trawl-door with main element and leading-edge slat	58
A.1	Comparison of initial and optimized results of a trawl-door with a main element and trailing edge flap. The objective is to maximize C_l/C_d with no additional constraints using multi-point space mapping	68
A.2	Comparison of initial and optimized results of a trawl-door with a main element and trailing edge flap. The objective is to maximize C_l/C_d with no additional constraints using multi-point space mapping with multi-step approach	73

A.3	Optimization result comparison for trawl-door with main element and flap with both using the single- and multi-level approaches	78
A.4	Comparison of initial and optimized results of a trawl-door with a main element and leading edge slat. The objective is to maximize C_l/C_d with no additional constraints using multi-point space mapping	81
A.5	Comparison of initial and optimized results of a trawl-door with a main element and leading edge slat. The objective is to maximize C_l/C_d with no additional constraints using multi-point space mapping	85
A.6	Optimization result comparison for trawl-door with main element and slat between the single- and multi-level approaches	90
B.1	Location of flap during grid convergence study	91
B.2	Location of slat and flap during grid convergence study	95

List of Abbreviations

2D	Two-Dimensional
3D	Three-dimensional
CFD	Computational Fluid Dynamics
ME	Main Element
TE	Trailing Edge
LE	Leading Edge
RSA	Response Surface Approximation
SM	Space Mapping
LF	Low-Fidelity
HF	High-Fidelity
LSH	Latin Hypercube sampling
SM	Space Mapping
V&V	Verification and Validation

List of Symbols

α	Angel of attack
α_{stall}	Stall angle of attack
α_0	Zero lift angle of attack
c	Chord length
c_{ME}	Chord length of main element
c_{slat}	Chord length of slat
c_{flap}	Chord length of flap
V_∞	Free stream velocity
θ_{flap}	Flap angle
θ_{slat}	Slat angle

Chapter 1

Introduction

1.1 Motivation and Background

Rising fuel prices have a significant impact on fisheries operating costs. Fuel consumed by the European Union fishing fleet alone was over 1,6 billion liters in 2011, and the second largest independent item of expenditure with 24 % share of fisheries total operating cost [4].

The fisheries mobile gear segments are the heaviest fuel consumers. The trawlers have to tow the fishing gear which generates a large flow resistance. Therefore these vessels are equipped with high power engines that consume large amounts of fuel during towing. This fuel consumption is depends on the efficiency of the fishing gear, engines, and the vessels itself. Even though trawlers often travel greater distances to fishing grounds, the fuel consumed during trawling is up to 80 % of the total consumption [5]. Thus, the design of the fishing gear is key for reducing the overall fuel consumption.

Typical trawlers fishing gear assembly consist of a large net, a pair of trawl doors (that serve the purpose of keeping the net open during trawling), and cables (which connect the net and the trawl doors to the trawler) as seen on Fig. 1.1. The net alone can be up to 160 m deep and 240 m wide [6] , and the size of the trawl doors varies from 1 – 20 m² depending on how much force is needed to keep the net open [7]. The cables on each side of the trawl gear varies in length from 150 – 2.000 m depending on the size of the fishing gear and method [8].

Recent work by Jonsson *et al.* [9] and Leifsson *et al.* [10] has demonstrated that hydrodynamic efficiency of modern trawl doors can be improved considerably using computational fluid dynamics (CFD) models and automated optimization techniques. CFD

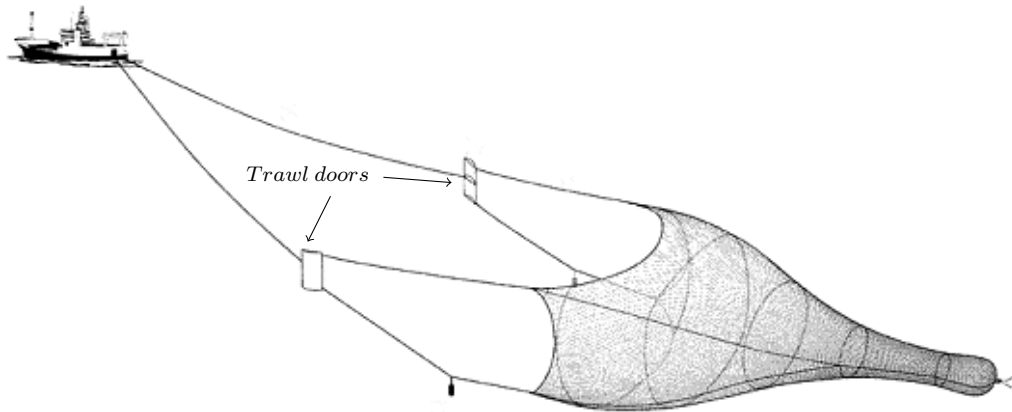


Figure 1.1: Typical assembly of trawlers fishing gear (Figure source from website¹).



Figure 1.2: Typical trawl-door manufactured from highly cambered steel plates (Figure source from website²).

offers the capability of accurately analyzing the fluid flow past the trawl-door shapes to predict their performance characteristics. However, high-fidelity CFD models are computationally expensive. Since the design of trawl-door shapes involves a moderately large design space (typically, less than 10 design parameters), using CFD models directly with conventional optimization techniques (such as gradient-based ones) can be impractical. Therefore, prior work on trawl-door shape optimization [9, 10] has investigated the use of surrogate-based optimization (SBO) techniques [11, 12, 13, 14], to accelerate the design process.

¹ Source: http://njscuba.net/artifacts/ship_fishing.html

² Source: <http://thyboron-trawldoor.dk/products/semipelagic-trawldoors/el-casador-xstream>

In Jonsson *et al.* [9], a variable-fidelity optimization method is used to speed up the design process. In particular, the method utilizes space mapping and low-fidelity CFD models to construct fast and reliable surrogates of computationally heavy high-fidelity CFD models. Satisfactory designs are obtained at low computational cost. However, the approach can be sensitive to numerical noise associated with the low-fidelity CFD model (the numerical noise levels are typically low in the high-fidelity models). Significant numerical noise present in the computational models may impact the optimization process since the design space will be multi-modal, and the low-fidelity model will not follow the overall trend of the high-fidelity model. In both these situations, the optimized designs may be different than the ones obtained by optimizing the high-fidelity model directly.

Leifsson *et al.* [10] used an iterative scheme with local response surface approximation (RSA) models of the expensive CFD trawl-door model constructed in each iteration. The RSA models are constructed using CFD data sparsely sampled in the vicinity of the current design, and a low-order polynomial approximation (to reduce the influence of the CFD model numerical noise on the optimization, as well as minimizing the number of required data samples). The size of the vicinity (i.e., the RSA model domain) is automatically adjusted in each iteration based on the performance of the model. The approach is efficient and yields good results at a relatively low cost. Nevertheless, the method utilizes only high-fidelity CFD model evaluations. There should be room for improving the optimization cost by utilizing variable-fidelity models.

1.2 Research Objectives and Contributions

The objectives of this research work are to address the following areas of trawl-door shape optimization:

1. **Improve the CFD simulations:** A major part of this work is to enhance the grid generation of the CFD modeling to more accurately capture the nonlinearity of the flow past multi-element trawl-door shapes. This will yield more accurate and robust CFD analysis of trawl-door shapes. The enhanced CFD model will be validated against experimental data of the flow past multi-element airfoil shapes since data for trawl-door shapes is not publicly available.
2. **Investigate an alternative problem formulation:** Prior work in this area have used the drag coefficient as the figure of merit and used the lift coefficient as a constraint, i.e., lift-constrained drag minimization. In this work, we will improve

the performance of trawl-door shapes by maximizing the lift-to-drag ratio. Thus, the optimization problem is converted from being constrained to unconstrained.

3. **Improve the surrogate modeling:** Use a mixed surrogate-based modeling approach to trawl-door shape optimization, i.e., construct a function approximation surrogate using physics-based models of varying fidelity. This approach has been successfully applied to simulation-based optimization in other areas such as microwave antenna and filter design [14]. In this thesis work, the space mapping technique is utilized to create a fast surrogate based on high- and low-fidelity model data. Then, the variable-fidelity surrogate is used to construct a global surrogate model of the design space using a function approximation technique, in this case kriging interpolation. This approach should alleviate some of the limitations of using only space mapping without compromising computational cost.

The contributions of the research are the combined outcomes of objectives 1, 2 and 3 and will yield a more robust and reliable SBO approach for design of trawl-door shapes.

1.3 Thesis Outline

The formulation of the design problem (Objective 2) is given in Chapter 2. In Chapter 3, the computational fluid dynamics modeling and validation results are described (Objective 1). Chapter 4 presents the optimization and surrogate modeling approach (Objective 3). Results of applications of the optimization approaches are given in Chapter 5 (Objectives 1, 2, and 3). Chapter 6 concludes the thesis. Further details and results of several aspects of the work are given in the Appendices.

Chapter 2

Problem Formulation

The objective of this work is to optimize the shape and configuration of trawl-doors, where they are treated as an independent system. The conventional trawl-doors are not considered since recent studies have revealed that airfoil-shaped trawl-doors, as proposed by Jonsson [15] and Hermannsson [16] are much more efficient than the conventional shape. Here we consider trawl-doors that are constructed from airfoil-shaped elements with multi-element configurations. Three sets of configurations are presented, main element with leading-edge slat, trailing edge flap or both as shown in 2.1.

In this study there are two separate objective functions. First we minimize the drag coefficient for given lift. The problem is formulated as in study performed by Leifsson *et al.* [10]. That study is used as a comparative benchmark for the computational efficiency and quality of the solution acquired in this study. The subsequent objective function is to maximize the ratio between lift and drag, without any additional constraints.

Then the optimization problem is formulated as

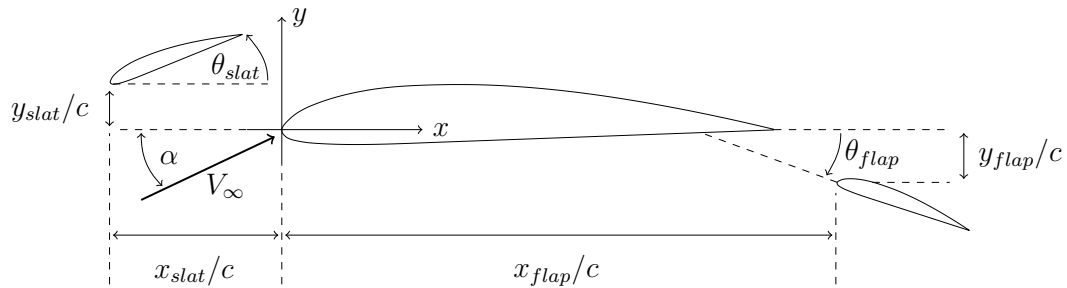


Figure 2.1: Two dimensional view of multi-element trawl-door constructed from airfoil shaped elements

$$\max C_l(\mathbf{x})/C_d(\mathbf{x}), \quad (2.1)$$

where C_l is the lift coefficient, C_d is the drag coefficient, and \mathbf{x} is the vector of design variables.

Here the shape of each element and the free-stream velocity V_∞ is held constant through the optimization process. The inclination and position of the leading-edge flap and the trailing-edge slat, as well as angle of attack are designable parameters. Then the vector of design variables for multi element trawl-door with leading-edge slat and trailing-edge flap can be written as

$$\mathbf{x} = [x_{slat}/c \quad y_{slat}/c \quad \theta_{slat} \quad x_{flap}/c \quad y_{flap}/c \quad \theta_{flap} \quad \alpha]^T, \quad (2.2)$$

where x_{slat}/c is the slat leading-edge position on the x-axis, y_{slat}/c is the slat leading-edge position on the y-axis, θ_{slat} is the inclination of the slat relative to the x-axis, x_{flap}/c is the flap leading edge position on the x-axis, y_{flap}/c is the flap leading-edge position on the y-axis, θ_{flap} is the inclination of the flap relative to the x-axis, α is the angle of attack relative to the x-axis and c is the chord length of the main element. Through this study the shape of the elements are normalized, so that $c = 1$. All design variables are subjected to bounds, that is $\mathbf{l} \leq \mathbf{x} \leq \mathbf{u}$, where \mathbf{u} is the upper bound of the design variable vector and \mathbf{l} is the lower bound.

Then the problem can be re-written as

$$\mathbf{x}^* = \arg \min_{\mathbf{x}} H(\mathbf{f}(\mathbf{x})), \quad (2.3)$$

where \mathbf{f} is the high-fidelity model response, described in Chapter 4, and H is the objective function. The model response $\mathbf{f}(\mathbf{x}) = [C_{l,f} \quad C_{d,f}]^T$ where $C_{l,f}$ and $C_{d,f}$ are the lift and drag coefficients obtained by the high-fidelity model. Then for lift over drag maximization the objective function takes the form $H(\mathbf{f}(\mathbf{x})) = -C_{l,f}(\mathbf{x})/C_{d,f}(\mathbf{x})$.

Chapter 3

Computational Fluid Dynamics Modeling

This chapter describes the computational fluid dynamics (CFD) modeling for trawl-door flow analysis in two-dimensions. In particular, the governing equations, computational grid, and flow solver are described. Furthermore, the chapter gives results of grid independence studies, validation studies, and numerical noise analysis.

3.1 Governing Equations

The flow is assumed steady, incompressible, and viscous. Governing equations are the Reynolds-Averaged Navier-Stokes (RANS) equations, derived from the conservation of mass and momentum principles.

The mass conservation (continuity) equation can be written as [17]

$$\frac{\partial \rho}{\partial t} + \nabla(\rho u) = 0 \quad (3.1)$$

where ρ is the fluid density, u is the velocity and ∇ is the Nabla operator ($\partial/\partial y, \partial/\partial x, \partial/\partial z$). Since the working fluid is water the flow is considered incompressible, then equation 3.1 reduces to

$$\nabla u = 0. \quad (3.2)$$

The conservations of momentum equation can be written as

$$\frac{\partial(\rho u)}{\partial t}(\rho \vec{u}) + \nabla(\rho \vec{u} \vec{u}) = -\nabla p + \nabla \bar{\tau} \quad (3.3)$$

$$\frac{\partial}{\partial t}(\rho \vec{u}) + \nabla(\rho \vec{u} \vec{u}) = -\nabla p + \nabla \bar{\tau} \quad (3.4)$$

where p is the fluid pressure, and $\bar{\tau}$ is the stress tensor given by

$$\bar{\tau} = \mu \left[(\nabla \vec{u} + \nabla \vec{u}^T) - \frac{2}{3} \nabla \vec{u} I \right]. \quad (3.5)$$

Here μ is the dynamic viscosity and I is the unit tensor. Since compressibility and heat transfer is not considered in this study, the energy conservation equation is not solved.

To be able to effectively model the effect of turbulence, equations 3.1 and 3.1 are split-up to mean and fluctuating components $u_i = \bar{u}_i + u'_i$, where \bar{u}_i and u'_i are the mean and fluctuating components resulting in the Reynolds-averaged Navier-Stokes equations [18].

$$\frac{\partial \bar{u}_i}{\partial x_i} = 0 \quad (3.6)$$

$$\frac{\partial}{\partial t}(\rho \bar{u}_i) + \frac{\partial}{\partial x_j}(\rho \bar{u}_i \bar{u}_j) = -\frac{\partial p}{\partial x_i} + \frac{\partial}{\partial x_j} \left[\mu \left(\frac{\partial \bar{u}_i}{\partial x_j} + \frac{\partial \bar{u}_j}{\partial x_i} \right) - \rho \overline{u'_i u'_j} \right] \quad (3.7)$$

The term $-\rho \overline{u'_i u'_j}$ represents the Reynolds stresses, that has to be modelled with a turbulence model.

The Menter's Shear-Stress Transport (SST) $k - \omega$ turbulence model was used to model this turbulence. The model is considered more accurate and reliable for flow over airfoils than the standard $k - \omega$ model. The transport equations used to obtain the turbulence kinetic energy k and the specific dissipation rate ω are written as [18]

$$\frac{\partial}{\partial t}(\rho k) + \frac{\partial}{\partial x_i}(\rho k u_i) = \frac{\partial}{\partial x_j} \left(\Gamma_k \frac{\partial k}{\partial x_j} \right) + G_k - Y_k + S_k \quad (3.8)$$

and

$$\frac{\partial}{\partial t}(\rho \omega) + \frac{\partial}{\partial x_j}(\rho \omega u_j) = \frac{\partial}{\partial x_j} \left(\Gamma_\omega \frac{\partial \omega}{\partial x_j} \right) + G_\omega - Y_\omega + D\omega + S_\omega. \quad (3.9)$$

Here the term G_k stands for production of turbulence kinetic energy, Y_k and Y_ω is the dissipation of k and ω caused by turbulence, G_ω represents generation of ω , S_k and S_ω are source terms defined by the user and D_ω is the cross-diffusion term, Γ_k and Γ_ω are the effective diffusivity of k and ω . Refer to Tannehil *et al.* [19] for further details on the SST $k - \omega$ turbulence model.

3.2 Flow Solver

For solving the governing equations in 3.1 the commercial computer code ANSYS Fluent 14.0 [20] is used. The solver is coupled velocity-pressure-based formulation. The spatial discretization schemes are second order for all flow variables and the gradient is found by node based Green-Gauss method [18]. Due to complex flow condition at high angles of attack a pseudo-transient option and high-order relaxation terms are used to obtain stable convergence.

The working fluid were water, set with density of 998.2 kg/m^3 and dynamic viscosity $1.003 \times 10^{-3} \text{ Pa s}$. The free-stream flow velocity for all optimization processes were set to 2 m/s with Reynolds number $Re = 2 \times 10^6$ to simulate the trawl-doors expected flow conditions [16].

The solution controls were set with Flow Courant number CFL as 40, momentum and pressure relaxation factors were 0.10. The under relaxation factors for both turbulent kinetic energy and specific dissipation rate were set to 0.8, while higher order term relaxation factor for flow variables were set to 0.25.

3.3 Computational Grid

The goal was to have a grid with good quality, that could be generated both automatically and robustly according to updated geometries proposed by an optimizer. The far-field was configured with a box-topology, extending 100 main element chord-lengths c in all directions from the leading edge of the main element that was located in the center of the box, as seen on figure 3.1. The far-field has to be located relatively far away from the trawl-door so that the flow generated by the boundary conditions is fully developed at the trawl-door for consistency of the flow solution.

The grid was generated with the commercial code ICEM CFD [21]. Unstructured triangular grid was chosen, it is generated more automatically and robustly when dealing with complex geometries than structured grids [22]. The triangular grid is clustered around the trawl-door geometry, and grows in size as it gets closer to the far-field where the maximum size is defined as $10c$. The initial size of the triangular grid, closest to the trawl-door is defined by the spacing between elements of the prismatic inflation layer that is extruded from all geometry surfaces. The inflation layer is to capture characteristics of the boundary-layer and spacing between elements in stream-wise direction is determined by performing a grid convergence study, as described in chapter 3.4. 10 prismatic layers

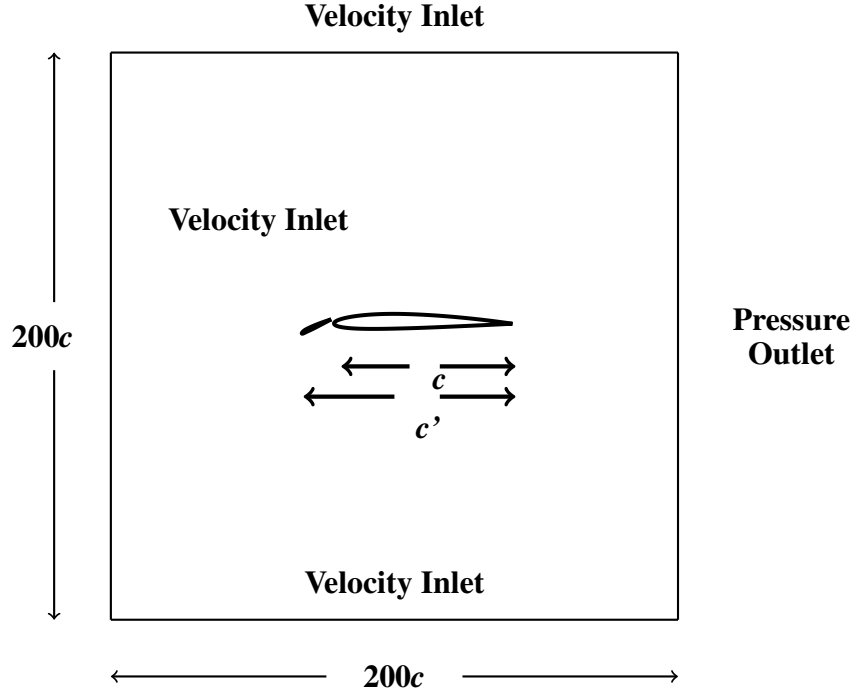


Figure 3.1: Configuration of the solution domain and boundary conditions. The leading edge of the trawl-door main element is located in the centre, and the box is extended 100 chord lengths c in all directions.

were extruded from the geometry with exponential growth ratio of 1.2 and the initial layer height were set to $2.5e-5$ for the optimized geometries so that the non-dimensional wall distance $y^+ < 1$.

Both upper and lower curves of each element of the airfoil-shaped geometry are split in two curves, so that high quality inflation layer can be generated robustly at the leading-edge where there is high curvature and around the sharp trailing edge. In addition the spacing between nodes at both the leading and trailing edges are 0.5 times the general spacing, resulting in denser regions where the flow is more complex. an example grid can be seen on figure 3.2.

3.4 Convergence Study

Iterative convergence were monitored by examining convergence history of the lift coefficient C_l , drag coefficient C_d and the residuals that are the sum of the L2 norms of the governing equations summed over all nodes. The convergence criteria were that the solution was converged after it had reached 6,000 iterations, or if the residuals had dropped by six orders in magnitude. After the solution were converged according to the criteria, the

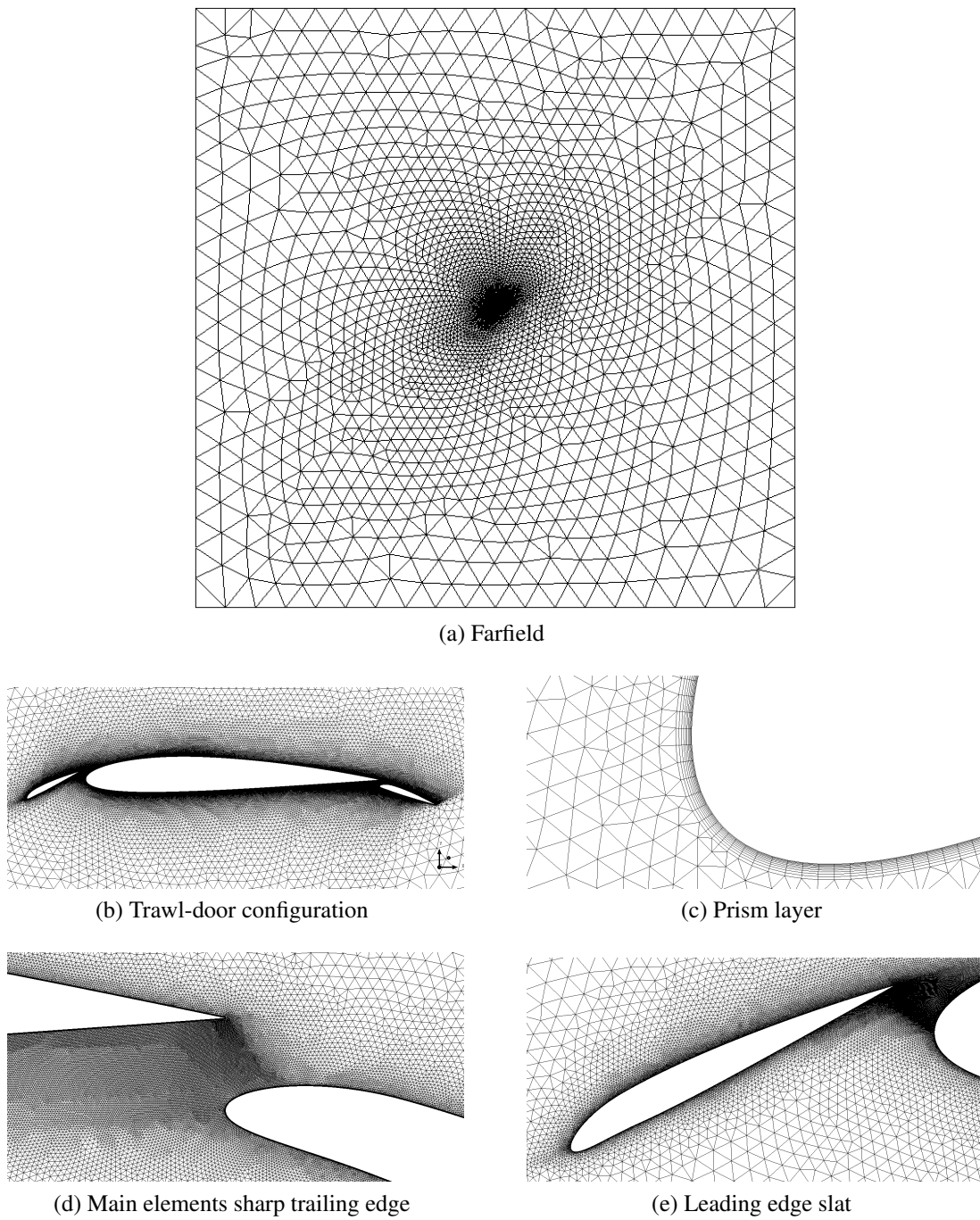


Figure 3.2: Example grid for multi-element trawl-door with leading edge slat and trailing edge flap

solution were considered acceptable if the residuals had dropped by 4 orders in magnitude and visual inspection of C_l and C_d had confirmed that the solution were stable. Figures 3.3 to 3.5 show an example of how the solution changes over number of iterations for grids with variable density.

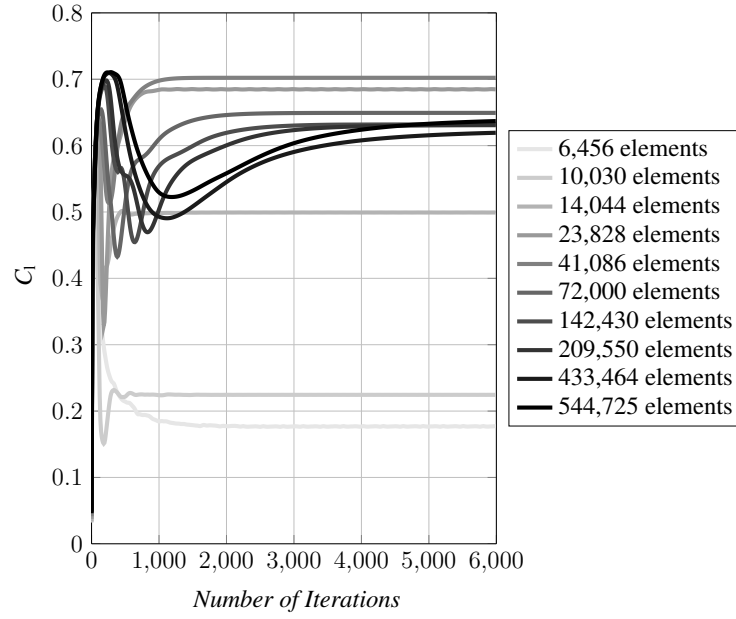


Figure 3.3: Convergence of lift coefficient C_l for ten grids with variable density

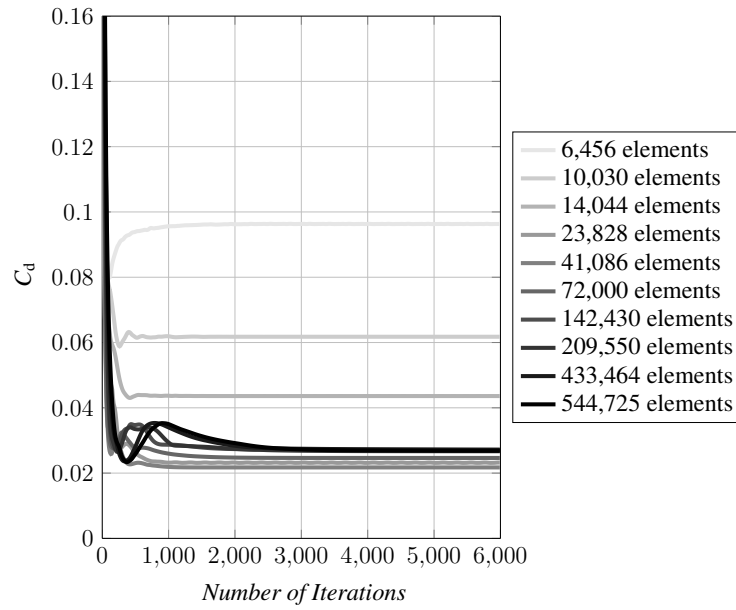


Figure 3.4: Convergence of drag coefficient C_d for ten grids with variable density

A grid convergence study were performed for all optimized geometries. At lest three grids were required to perform a convergence study. A representative cell size h for two dimensional grid is defined as [23]

$$h = \left[\frac{1}{N} \sum_{i=1}^N (\Delta A_i) \right]^{1/2}, \quad (3.10)$$

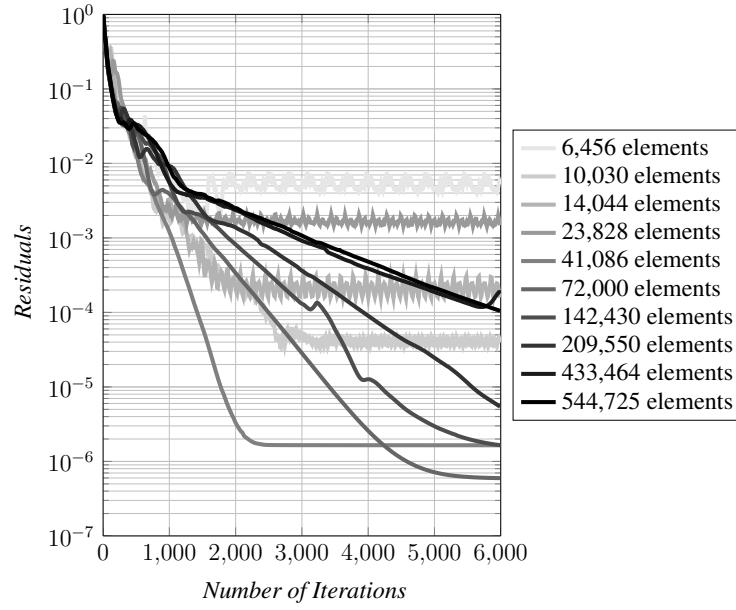


Figure 3.5: Solution residuals for ten grids used in the grid convergence study

where N is the total number of cells in the grid and ΔA_i is the area of the i -th cell. Then the grid refinement factor r between two computational grids can be calculated with,

$$r = \frac{h_{coarse}}{h_{fine}} \quad (3.11)$$

where h_{coarse} stands for the coarser grid and h_{fine} represents the finer grid. The value of r close to 1 are inconvenient since the changes in the solution will be very small, and r close to 2 can be too large. Stern et.al [24] suggest $r = \sqrt{2}$, while Celik et.al [23] suggests $r > 1.3$ based on experience. Since the grid used in this study is unstructured a constant r between grids that is $r_{12} = r_{23} = r_{n+1}$ where n is the n -th grid is not feasible, since the number of cells in each grid were dependant of number of stream-wise nodes on the main element, as seen in section 3.3. In this study, number of stream-wise nodes on main element were doubled between each grid refinement starting on a coarse grid. The grid were refined until variables of interest C_l and C_d appeared stable, resulting in an refinement factor on the range $1.2 < r < 1.4$ that were considered acceptable.

To identify the solution convergence condition, the solution change ε , defined as

$$\begin{aligned} \varepsilon_{k21} &= S_{k2} - S_{k1} \\ \varepsilon_{k32} &= S_{k3} - S_{k2} \end{aligned} \quad (3.12)$$

where S_k is the simulated solution for the k 'th grid triplet and the subscript 1 represents the finest grid, 2 the medium grid and 3 the coarsest. Then the convergence condition R_k

is the ratio between the solution change, defined [23]

$$R_k = \frac{\varepsilon_{21}}{\varepsilon_{32}} \quad (3.13)$$

The convergence ratio indicates the convergence conditions [23]:

1. Monotonic convergence, $0 < R_k < 1$
2. Oscillatory convergence, $R_k < 0$
3. Divergence, $R_k > 1$

In this study all solutions experienced oscillatory convergence somewhere in the grid refinement process, that is due to slight noise in the unstructured grid. An uncertainty estimation were performed as proposed by Celik et.al [23] for oscillatory convergence, where uncertainties U_k are estimated with

$$U_k = \frac{1}{2}(S_U - S_L), \quad (3.14)$$

where S_U is the upper bound and S_L is the lower bound of the oscillating solutions. In this case the sign and magnitude of the error can not be estimated [23].

Figure 3.7 shows a grid convergence study performed with a grid generated as described in chapter 3.3, for a trawl-door with a main element and a leading edge slat as seen on figure 3.6. The main element is NACA 2412 and the leading edge slat is NACA 3210 placed at $x = -0.18$ $y = -0.08$. The length of the slat were 20% of the length of the main element and at an angle of 35° . The assembly were placed at an angle of attack of 5° and the velocity were set at $2m/s$. The uncertainty for each grid triplet were estimated with the procedure above.

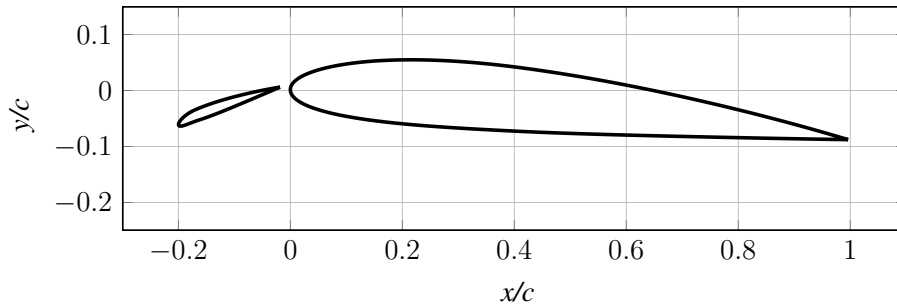


Figure 3.6: Trawl-door geometry used for the grid convergence study

Table 3.1 summarizes the result of the convergence study. It can be seen that the first three grid triplets consists of coarse and unreliable grids inheriting high uncertainties. The uncertainty reduces as the grids get finer and the solution more stabled, until it reaches

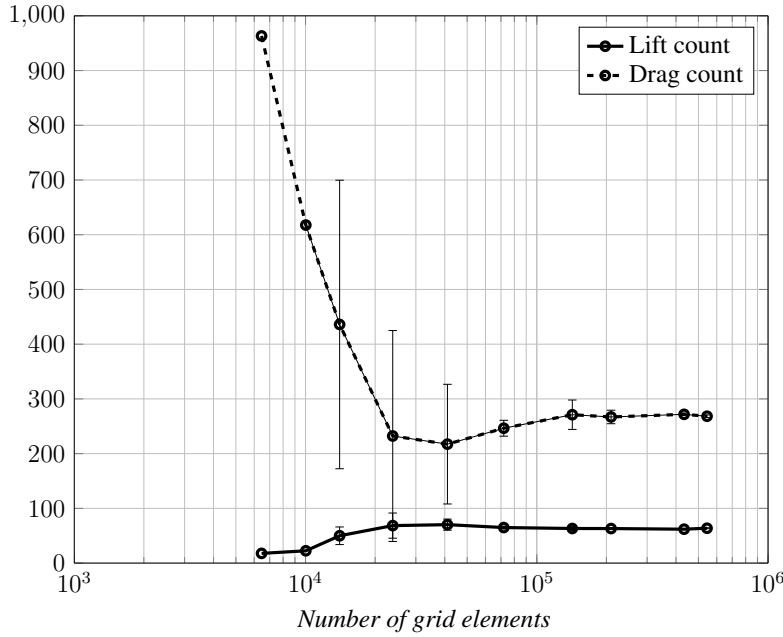


Figure 3.7: Grid convergence study for a trawl-door with uncertainty estimation

a minimum at grid triplet seven where the solution is considered converged. For that reason grid number 9 with 4,800 elements distributed over the main element in stream-wise direction, resulting in total number of approximately 517,000 elements were chosen for the optimization process for this geometry. Additional convergence studies for other trawl-door geometries can be found in appendix B.

Table 3.1: Results of the grid convergence study for variables C_l and C_d , uncertainty estimation and conversion ratio for all grid triplets

k	R_{lift}	Lift count	U_{Lc}	R_{drag}	Drag count	U_{Dc}
Grids 1 - 3	5.8	49.92	$\pm 16,10$	0.53	436.0	$\pm 263,6$
Grids 2 - 4	0.68	68.47	$\pm 23,01$	1.1	232.2	$\pm 192,7$
Grids 3 - 5	0.094	70.22	$\pm 10,15$	0.073	217.4	$\pm 109,3$
Grids 4 - 6	-3.0	64.93	$\pm 2,644$	-1.9	246.4	$\pm 14,54$
Grids 5 - 7	0.33	63.19	$\pm 3,515$	0.85	271.1	$\pm 26,87$
Grids 6 - 8	0.063	63.08	$\pm 0,926$	-0.17	267.0	$\pm 12,33$
Grids 7 - 9	10	61.93	$\pm 0,627$	-1.2	271.8	$\pm 2,398$
Grids 8 - 10	-1.5	63.70	$\pm 0,882$	-0.27	268.3	$\pm 2,398$

Since efficient computational time is one of the objectives of this research the grid convergence study can be used to evaluate the efficiency of the grid chosen, and demonstrates the importance of limiting high fidelity evaluations in the optimization process. Figure 3.8 shows how the computational time increases as the total number of elements grow,

resulting in a computational time of 170 minutes for the grid chosen, with convergence criteria as explained in chapter 3.4.

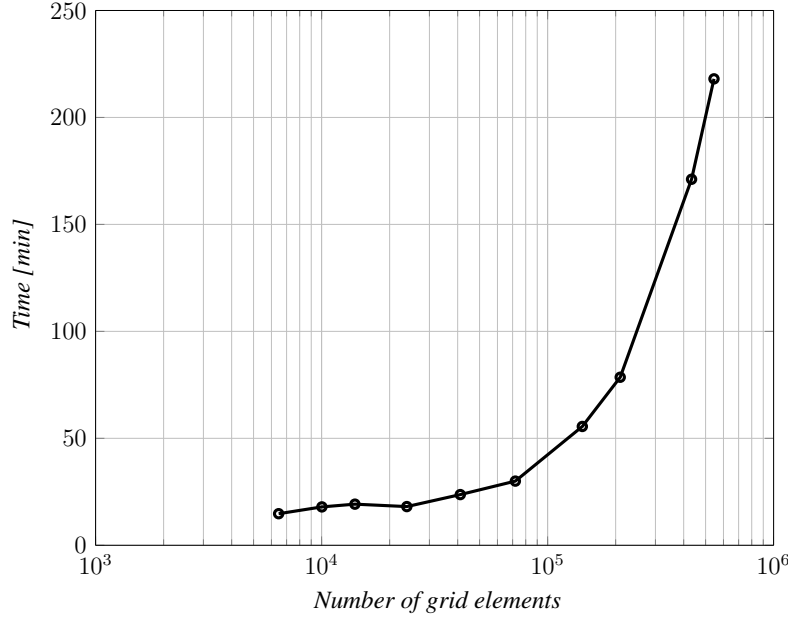


Figure 3.8: Computational time as a function of grid density

3.5 Validation

The purpose of the model validation is to estimate how the CFD model performs compared analytical or physical data. The first comparison were made using only one element, NACA 0012 since it has simple geometry being symmetric over the chord line and well documented [1, 25, 2]. The grid were structured according to section 3.3 and a grid convergence study were performed as seen in section 3.4. The CFD model were compared to wind tunnel data from Abbot and Von Doenhoff from Theory of Wing Sections [1], and data from Ladson [2]. The Ladson data is for $Re = 4.0e6$ instead of $Re = 3.0e6$ like the other cases. His data for $Re = 2.0e6$ show that the effect of Re in this region is negligible, therefore the results for $Re = 4.0e6$ were considered comparable in the validation process. In the Ladson data the transition were fixed at $0.05 c$ at both the upper and lower surfaces of the airfoil, the data used for comparison in this study are with grit No. 60-W. Figure 3.9 shows comparison on the lift coefficient C_l as a function of α between the CFD data and the wind tunnel data. The Thin Airfoil Theory lift curve is plotted for comparison as well.

There is a good agreement between the CFD model and the experimental data. Ladson experiences stalling at slightly lower α , the difference is under one degree while the CFD

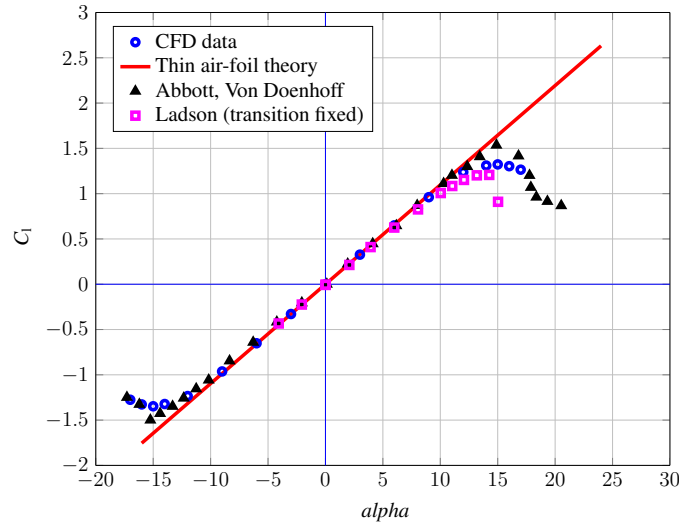


Figure 3.9: Model validation for NACA 0012 airfoil at $Re = 3.0e6$ showing C_l as a function of α . The red line represents the lift slope according to the Thin Airfoil Theory. The blue dots represent the CFD data and the black triangles are wind tunnel data obtained by Abbott et.al. [1]. The magenta boxes represent the Ladson data where the boundary layer transition were fixed at $0.05c$ [2].

model stall angle is similar to the Abbot and Von Doenhoff data. The main difference is in $C_{l,max}$, where that Abbot and Von Doenhoff measure $C_{l,max}$ over 1.54 compared to 1.21 in Ladsons study, while the CFD model lies between the two experiments with $C_{l,max} = 1.32$.

Thin Airfoil Theory tell us that symmetric airfoils have zero lift at $\alpha = 0$, and the lift slope should be symmetric about the origin. The CFD model should show these characteristics in the case of NACA 0012 airfoil, if the model is correctly implemented. At $\alpha = 0$ the CFD model estimates $C_l = 0.0009498$ that is close to zero and shows sign of numerical noise at third to fourth decimal point. Figure 3.10 shows the difference in symmetry about $\alpha = 0$ and $C_l = 0$, by comparing the absolute values of C_l and α . The model shows signs of negligible noise while the flow is attached at third to fourth decimal point, similar to $\alpha = 0$. When the flow starts to separate near α_{stall} , the lift curves show more sign of numerical noise. Still the difference in Cl is within 0.025 where it is the most at $\alpha = 15$.

If the drag coefficient is examined as seen in figure 3.11, that shows a drag polar comparison between the CFD model, Ladson and Abbot, Von Doenhoff experimental data. For comparison a solution for C_d were calculated for a flat plate at zero angle of attack with

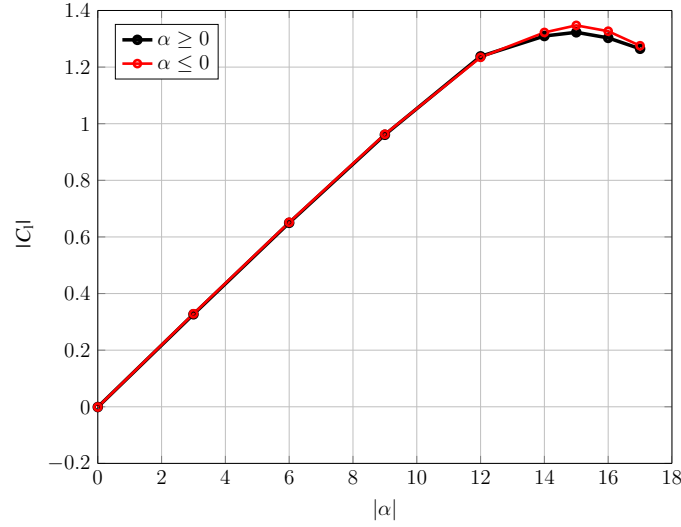


Figure 3.10: Difference in lift coefficient symmetry about $\alpha = 0$ and $C_l = 0$ for NACA 0012 airfoil at $Re = 3.0e6$. The red circles represents CFD data for $\alpha \leq 0$, while the black circles represent data for $\alpha \geq 0$.

equation 3.15 that estimates the frictional drag coefficient [26]

$$C_f = \frac{x_{cr}}{c} \frac{1.328}{\sqrt{Re_{cr}}} + \frac{0.074}{Re^{1/5}} - \frac{x_{cr}}{c} \frac{0.074}{Re_{cr}^{1/5}}. \quad (3.15)$$

Here Re_{cr} is the critical Reynolds number where the transition as said to occur and x_{cr} is the point of transition between the laminar and the turbulent flow, estimated with

$$x_{cr} = \frac{\mu Re_{cr}}{\rho V_{\infty}}. \quad (3.16)$$

Re_L is the Reynolds number for flow over flat plate defined,

$$Re = \frac{\rho V_{\infty} L}{\mu}. \quad (3.17)$$

where ρ is the fluid density, V_{∞} is the free stream velocity and L is the plate length.

The critical Reynolds number used were $Re = 1.0e6$ [17]. The pressure drag coefficient C_{pd} were considered to be 15% of C_f , as found out in Lombardi *et al.* [25] results for the NACA 0012 airfoil, that is considered reasonable for a blunt object at zero angle of attack [17]. Abbot and Von Doenhoff measure C_d considerably lower than the CFD model and Ladson, and even lower than in case of the flat plate. The location of boundary layer transition is hard to predict and can vary between experiments. Since Ladson fixed the location of transition it can be assumed from this comparison that Abbot and Von Doenhoff experience boundary layer transition further down the wing, even further than

in case of the flat plate where the transition occurs at $0.16c$. The CFD model lies between Abbot and Von Doenhoff results and ladsons, where the CFD model lies near ladsons results at lower angles of attack where the lift is moderate and then deviates towards Abbot and Von Doenhoff results as α increases.

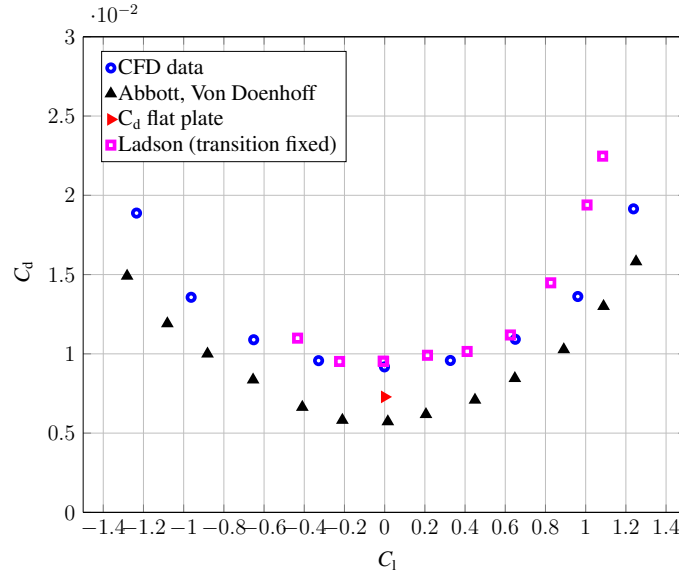


Figure 3.11: Model validation drag polar for NACA 0012 airfoil at $Re = 3.0e6$. The blue dots represent the CFD data and the black triangles are wind tunnel data obtained by Abbott et.al. [1]. The magenta boxes represent the Ladson data where the boundary layer transition were fixed at $0.05 c$ [2]. The red triangle is an estimation of C_d over a flat plate at $\alpha = 0$.

The CFD model is more extensively validated by comparing its results to wind tunnel tests of a NASA supercritical airfoils, performed by the Boeing Company for the National Aeronautics and Space Administration NASA [27]. The report contains extensive collection of 2D wind tunnel data for several models at various angles of attack and Reynolds numbers. The models of interest in this study is single ME, ME with flap, ME with slat and ME with slat and flap since they resemble the trawl door geometry the most.

The example validation presented here consists of a main element with a trailing edge flap as seen on figure 3.12, or Model B N1WC1F1 as named in the NASA report. The CFD model were constructed with a mesh as described in chapter 3.3, the convergence criteria were according to chapter 3.4 and convergence study performed according to same chapter. The grid were considered converged after stream-wise nodes on the main element had reached 4,800 nodes, resulting in a total of 603,880 elements. Comparable data were lift coefficient C_l as a function of angle of attack as seen on figure 3.13, lift coefficient as a function of the drag coefficient C_d as senn on figure 3.14 and the pressure coefficient C_p over both the main element and the flap for -10° , 0° and 9° angle of attack as seen on

figure D.4. Experimental results obtained at $Re = 2.01 \times 6$ were chosen for the validation process, since it close to the flow conditions used for the optimization process where the free stream velocity V_∞ is $2m/s$.

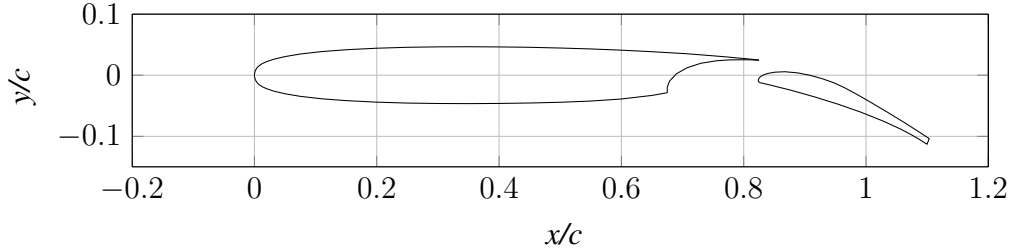


Figure 3.12: Geometry of NASA Model B N1WC1F1 airfoil used for the validation process

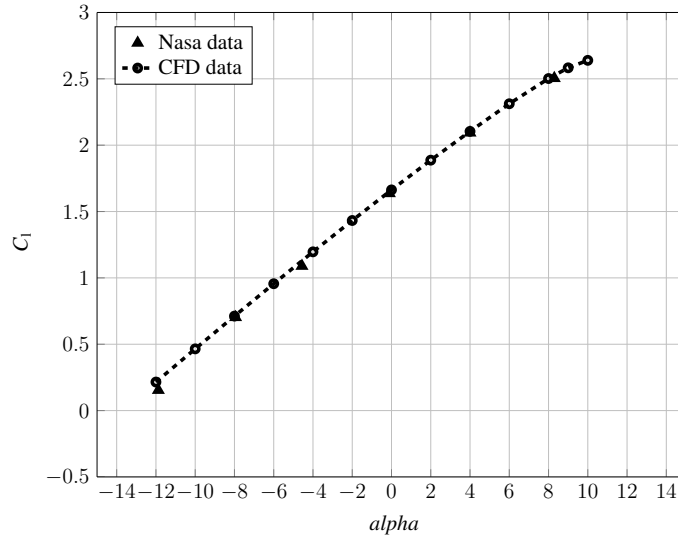


Figure 3.13: C_l as a function of α comparison between experimental data using NASA Model B N1WC1F1 airfoil and the CFD model

Agreement between the experimental data and the CFD model is good. The lift curve slope is shows minor deviations at $\alpha \leq -10^\circ$, that will not affect the optimization since it is at negative angle. The polar plot shows slightly more deviations. Since C_d is close to zero, the lift and drag ratio C_l/C_d is sensitive to minor changes in the drag coefficient. Drag forces can be hard to predict accurately, and the deviation considered to be within acceptable bounds. The C_p plots show excellent agreement whether the angle of attack is at a negative, zero or positive angle, that supports the decision that the quality of the CFD model is within acceptable bounds. More validation runs can be found in appendix D.

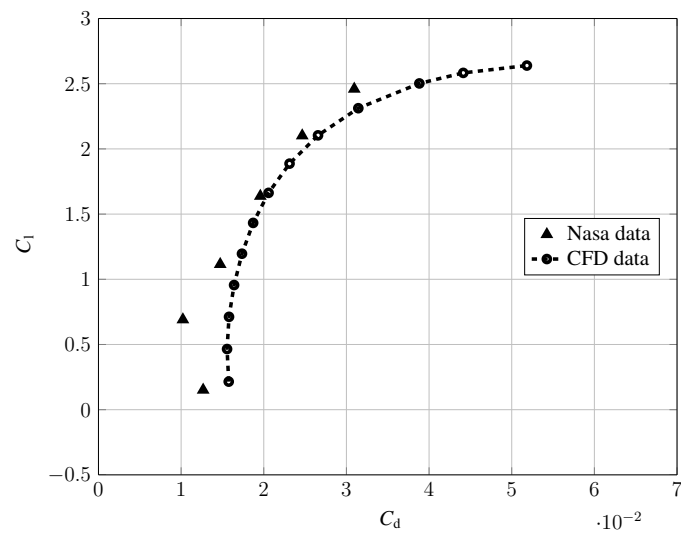


Figure 3.14: Drag polar plot comparison between experimental data of NASA Model B N1WC1F1 airfoil and the CFD model

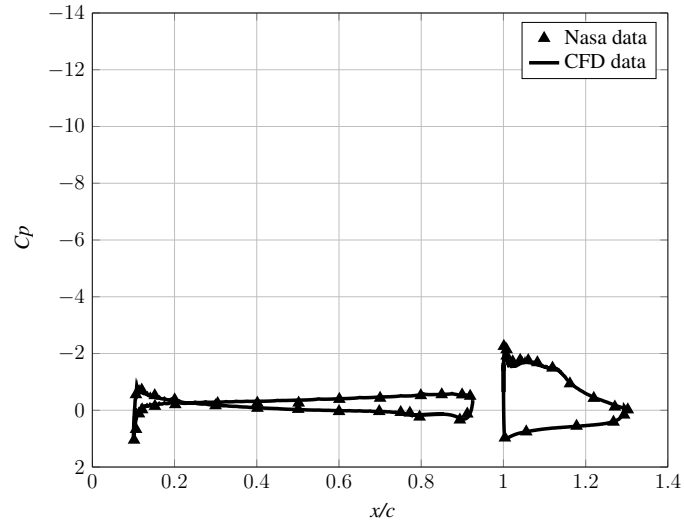
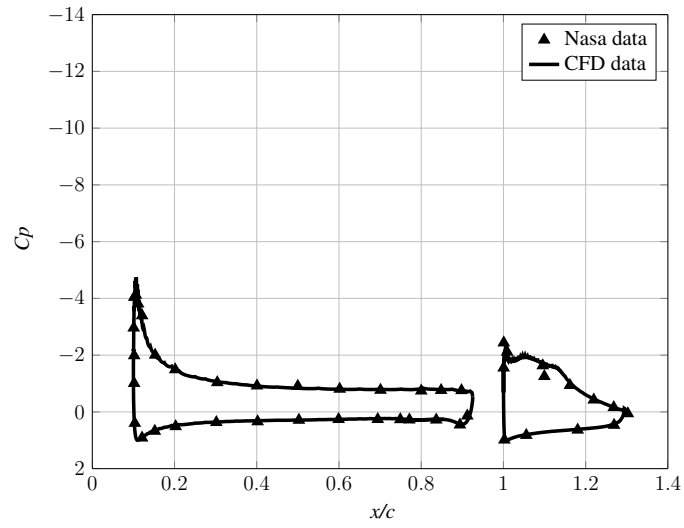
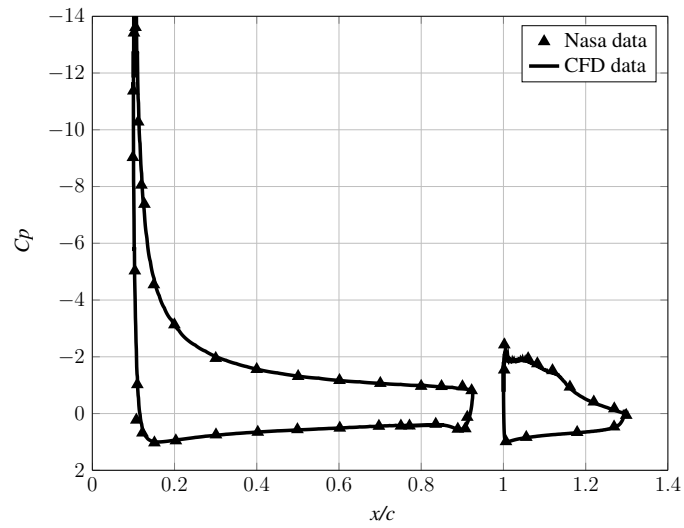
(a) $\alpha = -8^\circ$ (b) $\alpha = 0^\circ$ (c) $\alpha = 9^\circ$

Figure 3.15: Comparison between experimental data and the CFD model on pressure coefficient C_p over surface of a NASA Model B N1WC1F1 airfoil, consisting of a main element and a flap at three angles of attack

3.6 Numerical Noise Analysis

A numerical noise analysis was performed on the same trawl-door model as the grid convergence study in 3.4. The purpose was to determine the quality of the solution obtained by the optimization process, choose a low-fidelity CFD model that fulfilled the quality needed and verify that the noise in the high-fidelity model were negligible compared to the low-fidelity one.

The noise in value of merit C_l/C_d were investigated in terms of design variables x_{slat}/c , y_{slat}/c , θ_{slat} and α . Noise in each design variable is examined for eight potential low-fidelity models with 24, 000, 33, 000, 42, 000, and 50, 000 elements where the model were considered converged after 1, 500 iterations, or when residuals had dropped by 5×10^{-3} . And for the same grids where the model were considered converged after 2, 000 iterations, or when residuals had dropped by 5×10^{-4} . In addition the noise were examined for the high-fidelity model chosen in chapter 3.4.

The noise study is performed by varying each design variable independently while monitoring the lift-to-drag ratio. Changes in design variables have to be small enough so that the analysis captures the noise in the model instead of the overall trend. Configuration of the trawl-door were chosen to be in close proximity of an optimized configuration of an initial optimization run (see appendix A). The baseline configuration and range for each design variables were $x_{slat}/c = -0.200 \pm 0.020$, $y_{slat}/c = -0.0467 \pm 0.020$, $\theta_{slat} = 25.33 \pm 0.25$ deg and $\alpha = 9.33 \pm 0.25$ deg. 40 simulation points were then distributed evenly over the range for all variables.

Noise results for the low-fidelity models are presented in table 3.2, and comparison of computational time for the models are shown in figure 3.16. The coarsest grids contain high level of noise, or up to 9 C_l/C_d . Even though the computational time is shortest for the coarsest grids they were considered infeasible for the optimization process. The improved convergence criteria also reduces the noise level, implying that the relaxed convergence criteria is not suitable. Only one case did not converge before reaching maximum number of iterations. Almost 6 minute peak in computational time figure 3.16, can be explained by poor quality of the grid that leads to inadequate solution convergence where the residuals oscillate between 5×10^{-3} and 5×10^{-3} .

The model chosen as a low-fidelity model for the optimization process were the finest one, with 50, 000 elements and the model were considered converged after 2, 000 iterations, or when residuals had dropped by 5×10^{-4} , with highest noise level in variable x/c of 1.2 C_l/C_d . Figure 3.17 shows the noise of each design variable for the model chosen and

figure 3.18 for the high-fidelity model, that had maximum noise level at design variable x/c of approximately $0.8 C_l/C_d$. Other results for models simulated in this study can be found in appendix C.

Table 3.2: Estimated noise in C_l/C_d for each design variable of a low-fidelity model

Design Variable	Number of elements			
	24.000	33.000	42.000	50.000
Converged after 2,000 iteration or residuals $\leq 5 \times 10^{-4}$				
\mathbf{x}/c	4.464	4.616	2.064	1.213
\mathbf{y}/c	9.079	4.120	1.973	1.312
θ	2.772	3.495	1.005	1.150
α	1.803	0.373	0.093	0.304
Converged after 1,500 iteration or residuals $\leq 5 \times 10^{-3}$				
\mathbf{x}/c	3.963	4.883	2.979	1.619
\mathbf{y}/c	8.239	4.999	2.012	1.660
θ	3.448	4.012	1.356	0.907
α	1.968	0.311	0.969	0.210

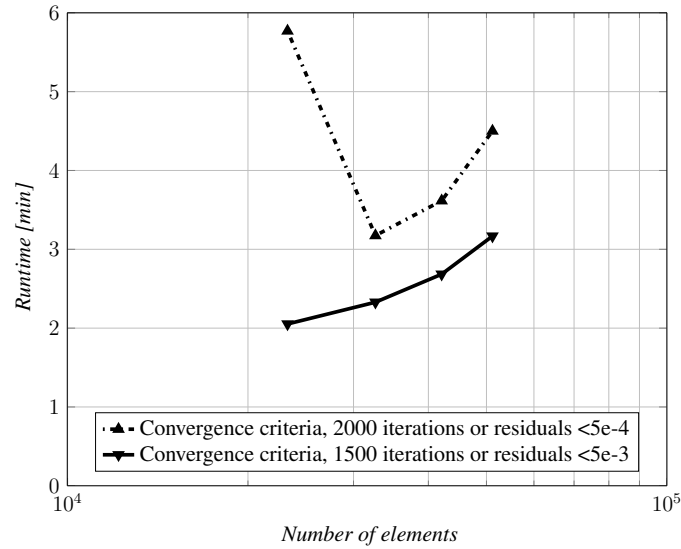


Figure 3.16: Low-fidelity model computational time example, obtained in the noise analysis process

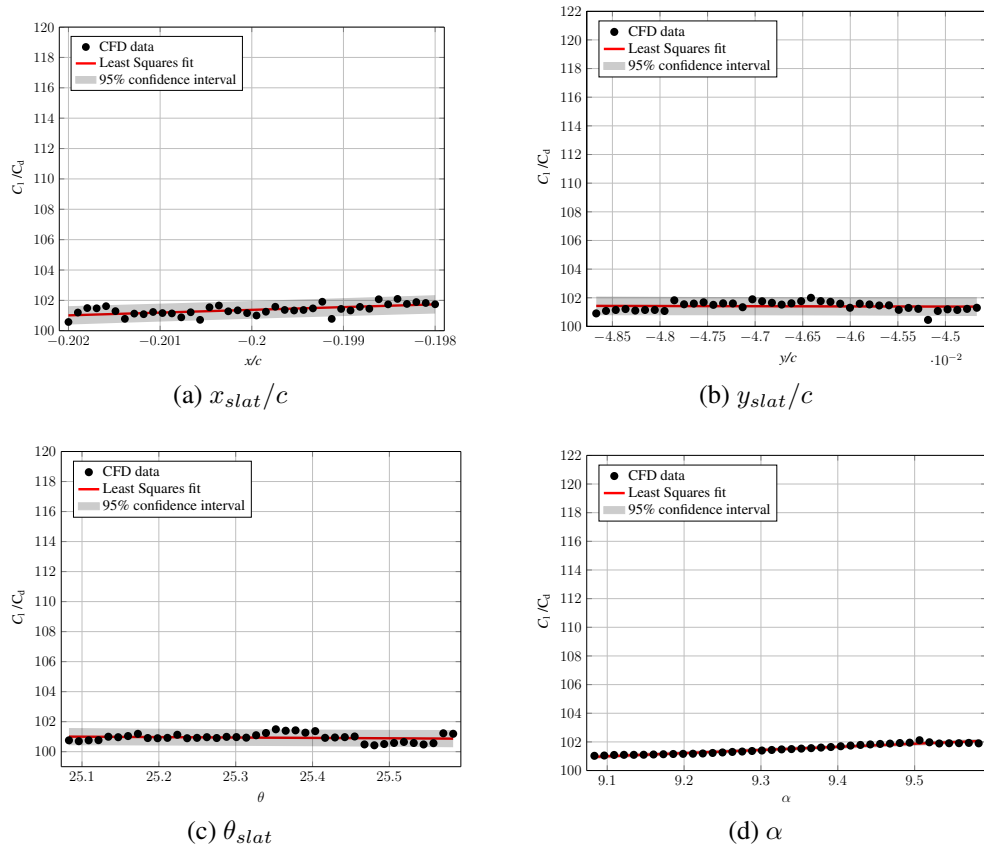


Figure 3.17: Noise in lift-to-drag ratio of the low-fidelity model chosen for the optimization process

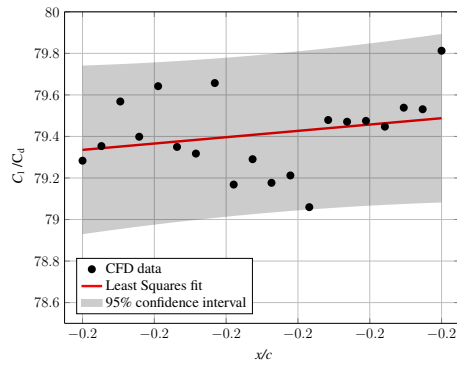
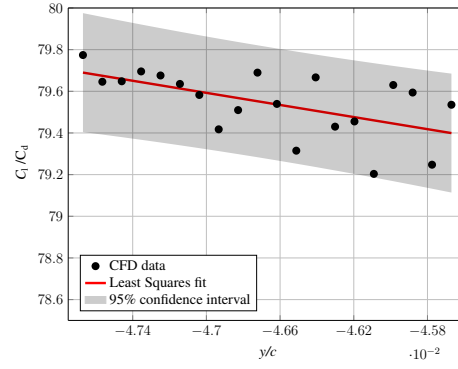
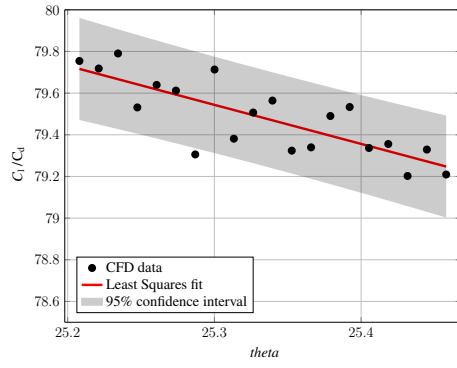
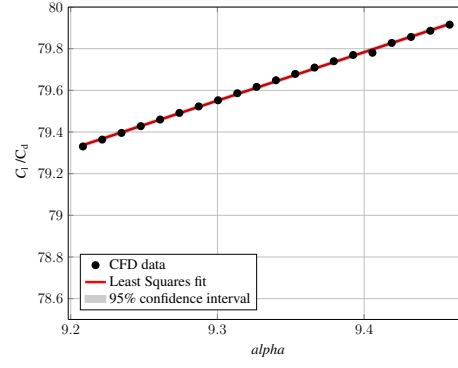
(a) Design variable x/c (b) Design variable y/c (c) Design variable θ (d) Design variable α

Figure 3.18: Noise in lift-to-drag ratio of the high-fidelity model chosen for the optimization process

3.7 Sensitivity Analysis

Sensitivity analysis were performed to estimate the effect (sensitivity) of each design variable on the lift-to-drag ratio, as well as to give an idea on how the design space close to optimum looks like. The sensitivity analysis is performed similar to the noise analysis in 3.6, except that the range of each design variables is much larger to capture the trend of the C_l/C_d curve.

Here the baseline configuration is the same as before, but the range were $x_{slat}/c = -0.200 \pm 0.050$, $y_{slat}/c = -0.0467 \pm 0.050$, $\theta_{slat} = 25.33 \pm 0.50$ deg and $\alpha = 9.33 \pm 0.50$ deg and the simulation points were reduced down to 10. Four models were sampled with the same grids as before, but only one convergence criteria were tested, that is convergence after 2,000 iterations or when residuals have reached 5×10^{-4} .

Figure 3.19 shows the results of the sensitivity analysis, where the noise in the coarser models is apparent, confirming the results of the noise analysis. Design variable α is the most sensitive of the design variables, it should be noted that abrupt changes in lift-over-drag is expected near α_{stall} after flow separation occurs. Solutions for the finest grid, used as a low-fidelity model gives relatively smooth solution in the interval chosen, with no signs of unexpected local min- or maximums.

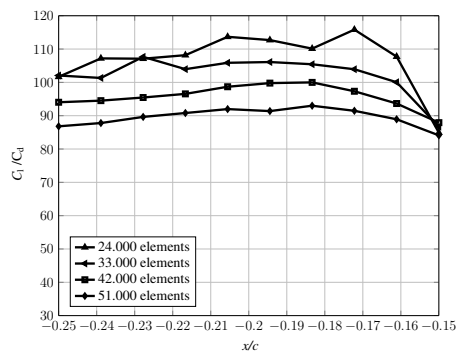
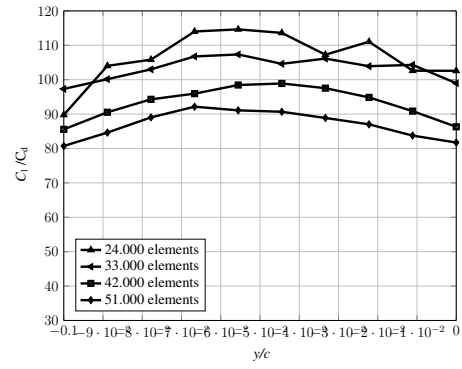
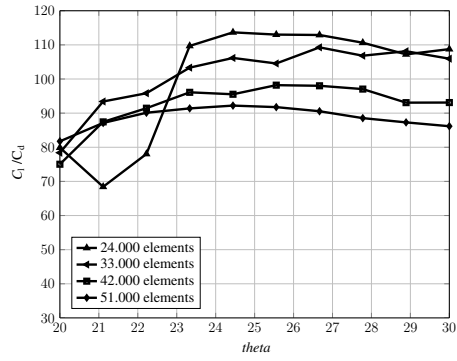
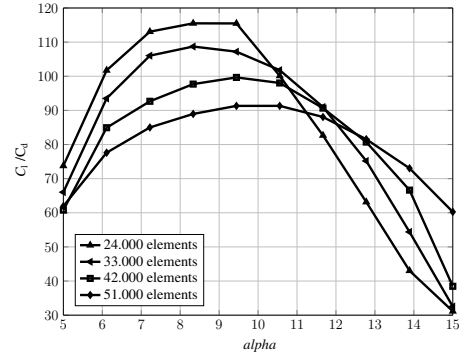
(a) Sensitivity in design variable x/c (b) Sensitivity in design variable y/c (c) Sensitivity in design variable θ (d) Sensitivity in design variable α

Figure 3.19: Sensitivity in design variables of a low-fidelity model at various grid densities

Chapter 4

Optimization Methodology

In this chapter, optimization methodology for trawl-door shape design is described. The chapter starts by describing the problem formulation and the surrogate-based optimization (SBO) approach. A general discussion of surrogate modeling is given, including the approximation- and physics-based approaches. The details of approximation-based surrogate modeling using kriging interpolation as well as physics-based surrogate modeling with multi-points space mapping. The chapter concludes with a description of a mixed surrogate modeling approach.

4.1 Formulation of the Optimization Problem

We will denote the response of the high-fidelity computational fluid dynamics (CFD) simulation model by $\mathbf{f}(\mathbf{x})$. \mathbf{f} represents an evaluation of the performance characteristics of interest, and the vector $\mathbf{x} = [x_1 \ x_2 \ \dots \ x_n]^T$ represents the designable parameters to be adjusted (see Chapter 2 for the definitions of the characteristics and design variables). The simulation-driven design task is usually formulated as a nonlinear minimization problem of the following form (same equation as in 2, renumbered for fullnesses of this chapter)

$$\mathbf{x}^* = \arg \min_{\mathbf{x}} H(\mathbf{f}(\mathbf{x})) \quad (4.1)$$

where H is the scalar merit function encoding the design specifications, whereas \mathbf{x}^* is the optimum design to be found. The composition $H(\mathbf{f}(\mathbf{x}))$ will be referred to as the objective function. The function H is implemented so that a better design \mathbf{x} corresponds

to a smaller value of $H(\mathbf{f}(\mathbf{x}))$. It is assumed that obtaining $H(\mathbf{f}(x))$ is computationally expensive.

4.2 Surrogate-Based Optimization

Conventional numerical optimization techniques, such as gradient-based search, are well established and robust methods. However, their applicability for solving contemporary design problems is limited due to the fundamental challenge of the high computational cost of accurate, high-fidelity simulations. Difficulties of the conventional optimization techniques, in the context of simulation-driven design, were the main incentives for developing alternative design methods. Perhaps the most promising way to address these issues, in particular, to conduct parametric optimization of expensive simulation models in a reasonable timeframe, is surrogate-based optimization (SBO) [11, 12, 13, 14].

The main concept behind SBO is to replace direct optimization of an expensive computational model by an iterative process in which a sequence of designs approximating the solution to the original optimization problem equation 4.1 is generated by means of optimizing a fast yet reasonably accurate representation of the high-fidelity model, referred to as a surrogate. In each iteration, the surrogate model is updated using the high-fidelity model evaluation at the most recent design (and, sometimes, some other suitably selected designs). Formally speaking, the surrogate-based optimization process can be written as [28]

$$\mathbf{x}^{(i+1)} = \arg \min_{\mathbf{x}} H(\mathbf{s}^{(i)}(\mathbf{x})) \quad (4.2)$$

where $\mathbf{x}^{(i)}$, $i = 0, 1, \dots$, is a sequence of approximate solutions to the original problem (1), whereas $\mathbf{s}^{(i)}$ is the surrogate model at the i th iteration. $\mathbf{x}^{(0)}$ is the initial design. Figure 4.1 shows the SBO process graphically using a high-fidelity CFD model.

The main prerequisite for the process 4.2 to be computationally efficient is the surrogate model \mathbf{s} being significantly faster than the high-fidelity model \mathbf{f} . At the same time, the surrogate has to be sufficiently accurate (in terms of representing the high-fidelity model). In case of local search methods, reasonable accuracy is only requested in the vicinity of the current design $\mathbf{x}^{(i)}$. If both conditions are satisfied, the algorithm 4.2 is likely to quickly converge to the high-fidelity model optimum \mathbf{x}^* .

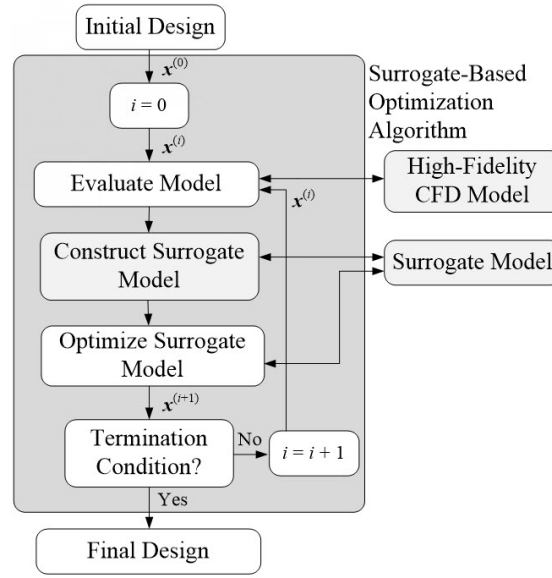


Figure 4.1: SBO work flow. [3]

4.3 Surrogate Modeling

Surrogate models can be roughly divided into two categories: (i) approximation (or functional) and (ii) physics-based ones. Approximation-based surrogate models are constructed through approximations of the high-fidelity model data obtained in the process of sampling the design space using appropriate design of experiments (DOE) methodologies. Approximation-based surrogates can be considered as generic models that are independent of the physics or any other knowledge about the problem at hand. The other class of models is based on exploitation of some knowledge about the system under consideration, usually embedded in a physics-based low-fidelity model. In the case of aero/hydrodynamic problems, the low-fidelity model can be obtained using simplified analytical description of the structure under design or from coarse-discretization CFD simulations. The surrogate itself is constructed by appropriate correction of the low-fidelity model, usually based on limited amount of high-fidelity model data.

4.3.1 Approximation-Based Surrogates

Approximation-based surrogates are constructed from sampled high-fidelity model data. Figure 4.2 shows the modeling flowchart for this type of models. The first stage is design of experiments (DOE) [29, 30, 31], which is essentially a strategy of allocating required number of samples in the design space. Having acquired high-fidelity model data, the model identification is performed using a selected approximation method. The surrogate

has to be verified to ensure sufficient accuracy, particularly its generalization capability, i.e., the quality of model predictions at the designs not seen during the identification stage. For that reason, model testing is normally performed using a separate set of testing samples. In practice, the modeling process may be iterative with the flow depicted in Fig. 4.2 constituting a single iteration. Upon validation of the surrogate, new set up samples together with the corresponding high-fidelity model data is then used to re-identify the model and such an adaptive sampling scheme is continued until the accuracy goals are met. In an optimization context, the surrogate model update may also be oriented towards finding better designs rather than towards ensuring global accuracy.

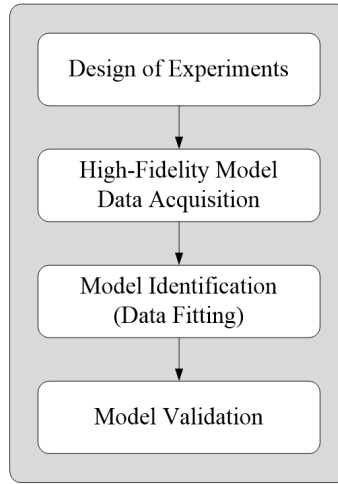


Figure 4.2: Approximation-based surrogate model construction flowchart [3]

Probably the most popular DOE for (relatively) uniform sample distributions is Latin Hypercube Sampling (LHS) [32]. In order to allocate p samples with LHS, the range for each parameter is divided into p bins, which for n design variables, yields a total number of p^n bins in the design space. The samples are randomly selected in the design space so that (i) each sample is randomly placed inside a bin, and (ii) for all one-dimensional projections of the p samples and bins, there is exactly one sample in each bin. Figure 4.3d shows an example LHS realization of 20 samples for two design variables ($n = 2$). It is worth noticing that the standard LHS may lead to non-uniform distributions (for example, samples allocated along the design space diagonal satisfy both the condition (i) and (ii)).

4.3.2 Physics-Based Surrogates

The main idea behind physics-based surrogates is the exploitation of the knowledge about the system of interest embedded in an underlying low-fidelity model, denoted here as $\mathbf{c}(\mathbf{x})$.

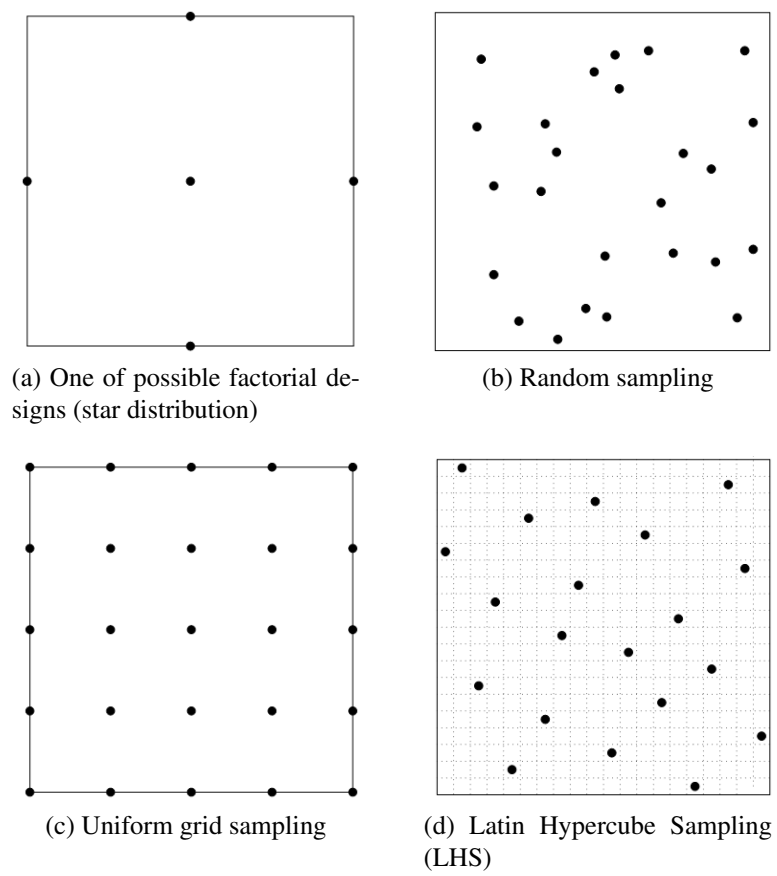


Figure 4.3: Popular design of experiments techniques [3].

The latter is a simplified representation of the system. It is computationally cheaper but, at the same time, less accurate than the high-fidelity model. The low-fidelity model can be obtained, for example, from the same simulator as the one used for the high-fidelity model but using a coarse discretization. Alternatively, the low-fidelity model can be based on simplified physics, or on a significantly different physical description; in some cases formulated using analytical or semi-empirical formulas. Because of its limited accuracy, the low-fidelity model has to be corrected to create a reliable surrogate.

The main advantage of physics-based models is that because of exploiting some knowledge embedded in the low-fidelity model a limited amount of high-fidelity data is necessary to ensure decent accuracy. For the same reason, physics-based surrogates are characterized by good generalization capability, i.e., they can provide reliable prediction of the high-fidelity model response at the designs not used in the training process. These advantages are normally translated into better efficiency (in particular, lower CPU cost) when physics-based surrogates are used in the design optimization process. It should be noted that the evaluation of a physics-based surrogate may involve, for example, the numerical solution of partial differential equations, or even actual measurements of the physical system.

Here we use Pattern search optimization, that is a derivative-free method, based on assessing the objective function within a bounded area exploring it with a structured set of points. The initial area is then modified during the optimization. This method is considered robust and relatively immune to numerical noise[3]. Figure 4.4 shows a simplified process of pattern search optimization where the structured set of points has been simplified to rectangular grid around the initial design. Once a more feasible solution compared to the initial one has been found, the optimizer moves to the improved solution and defines a new search area. The process is iterated until the optimizer fails to find improved solution, then the search area is reduced allowing smaller steps. The determination criteria is typically user defined, here the optimisation process was terminated once the search area had reduced under the numerical noise level of the CFD simulations used for the process.

4.4 Approximation-Based Surrogates via Kriging Interpolation

Kriging is a widely used technique to construct approximation-based surrogates [33, 34, 35]. Kriging is a Gaussian process based modeling method, which is compact and cheap

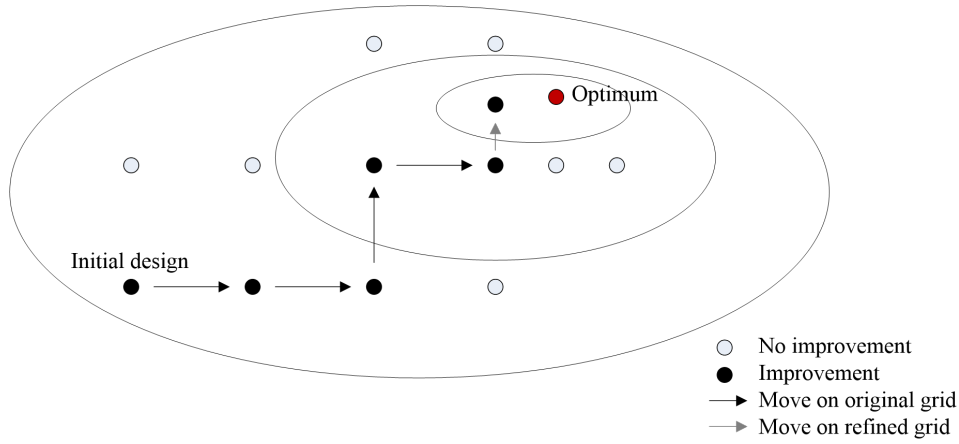


Figure 4.4: Simplified Pattern Search Optimization process [3]

to evaluate [36]. In its basic formulation, kriging assumes that the function of interest is of the following form [33, 34]:

$$\mathbf{f}(\mathbf{x}) = \mathbf{g}(\mathbf{x})^T \boldsymbol{\beta} + Z(\mathbf{x}), \quad (4.3)$$

where $\mathbf{g}(\mathbf{x}) = [g_1(\mathbf{x}) \ g_2(\mathbf{x}) \ \dots \ g_K(\mathbf{x})]^T$ are known (e.g., constant) functions, $\boldsymbol{\beta} = [\beta_1 \beta_2 \ \dots \ \beta_k]^T$ are the unknown model parameters (hyperparameters), and $Z(\mathbf{x})$ is a realization of a normally distributed Gaussian random process with zero mean and variance σ^2 . The regression part $\mathbf{g}(\mathbf{x})^T \boldsymbol{\beta}$ is a trend function for \mathbf{f} , and $Z(\mathbf{x})$ takes into account localized variations. The covariance matrix of $Z(\mathbf{x})$ is given as

$$\text{Cov} [Z(\mathbf{x}^{(i)}) (\mathbf{x}^{(j)})] = \sigma^2 \mathbf{R} ([R(\mathbf{x}^{(i)}, \mathbf{x}^{(j)})]), \quad (4.4)$$

where \mathbf{R} is a $p \times p$ correlation matrix with $R_{ij} = R(\mathbf{x}^{(i)}, \mathbf{x}^{(j)})$. Here, $R(\mathbf{x}^{(i)}, \mathbf{x}^{(j)})$ is the correlation function between sampled data points $\mathbf{x}^{(i)}$ and $\mathbf{x}^{(j)}$. The most popular choice is the Gaussian correlation function

$$R(\mathbf{x}, \mathbf{y}) = \exp \left[- \sum_{k=1}^n \theta_k |x_k - y_k| \right], \quad (4.5)$$

where θ_k are the unknown correlation parameters, and x_k and y_k are the k th components of the vectors x and y , respectively. The kriging predictor is defined as

$$\mathbf{s}(\mathbf{x}) = \mathbf{g}(\mathbf{x})^T \boldsymbol{\beta} + \mathbf{r}^T(\mathbf{x}) \mathbf{R}^{-1} (\mathbf{f} - \mathbf{G} \boldsymbol{\beta}), \quad (4.6)$$

where $\mathbf{r}(\mathbf{x}) = [R(\mathbf{x}, \mathbf{x}^{(1)}) \dots R(\mathbf{x}, \mathbf{x}^{(p)})]^T$, $\mathbf{f} = [f(\mathbf{x}^{(1)}) f(\mathbf{x}^{(2)}) \dots f(\mathbf{x}^{(p)})]^T$, and \mathbf{G} is a $p \times K$ matrix with $G_{ij} = g_j(\mathbf{x}^{(i)})$. The vector of model parameters $\boldsymbol{\beta}$ can be computed as $\boldsymbol{\beta} = (\mathbf{G}^T \mathbf{R}^{-1} \mathbf{G})^{-1} \mathbf{G}^T \mathbf{R}^{-1} \mathbf{f}$. Model fitting is accomplished by maximum likelihood for θ_k [33]. An important property of kriging is that the random process $\mathbf{Z}(\mathbf{x})$ gives information on the approximation error that can be used for improving the surrogate, e.g., by allocating additional training samples at the locations where the estimated model error is the highest [12, 33].

4.5 Physics-Based Surrogates via Multi-Point Space Mapping

A generic space mapping surrogate at iteration i in (4.2)

$$\mathbf{s}^{(i)}(\mathbf{x}) = s(\mathbf{x}, \mathbf{p}^{(i)}), \quad (4.7)$$

where the parameters \mathbf{p} are found by parameter extraction by solving a nonlinear minimization problem of the form

$$\mathbf{p}^{(i)} = \arg \min_{\mathbf{p}} \sum_{k=0}^i w_{i,k} \| \mathbf{f}(\mathbf{x}^{(k)}) - \mathbf{s}(\mathbf{x}^{(k)}, \mathbf{p}) \|^2, \quad (4.8)$$

where $w_{i,k}$ are weighting coefficients. For aero/hydrodynamic responses from CFD models, Koziel and Leifsson [37] suggested the following output space mapping surrogate form

$$\mathbf{s}^{(i)}(\mathbf{x}) = \mathbf{A}^{(i)} \circ \mathbf{c}(\mathbf{x}) + \mathbf{D}^{(i)} + \mathbf{q}^{(i)} = \begin{bmatrix} a_l^{(i)} C_{l,c}(\mathbf{x}) + d_l^{(i)} + q_l^{(i)} & a_d^{(i)} C_{d,c}(\mathbf{x}) + d_d^{(i)} + q_d^{(i)} \end{bmatrix}^T, \quad (4.9)$$

where \circ denotes component-wise multiplication, \mathbf{c} is the low-fidelity model, and the response correction parameters $\mathbf{A}^{(i)}$ and $\mathbf{D}^{(i)}$ are obtained by solving [38]

$$[\mathbf{A}^{(i)}, \mathbf{D}^{(i)}] = \arg \min_{[\mathbf{A}, \mathbf{D}]} \sum_{k=0}^i \| \mathbf{f}(\mathbf{x}^{(k)}) - \mathbf{A} \circ \mathbf{c}(\mathbf{x}^{(k)}) + \mathbf{D} \|^2. \quad (4.10)$$

The response scaling improves the matching for all points previously iterated. The additive response correction term $\mathbf{q}^{(i)}$ is defined as

$$\mathbf{q}^{(i)} = \mathbf{f}(\mathbf{x}^{(i)}) - \left[\mathbf{A}^{(i)} \circ \mathbf{c}(\mathbf{x}^{(i)}) + \mathbf{D}^{(i)} \right] \quad (4.11)$$

to make sure that there is perfect matching between the surrogate and the high-fidelity model at zero order consistency condition $\mathbf{x}^{(i)}, \mathbf{s}^{(i)}(\mathbf{x}^{(i)}) = \mathbf{f}(\mathbf{x}^{(i)})$.

The response correction parameters $\mathbf{A}^{(i)}, \mathbf{D}^{(i)}$ and the response scaling $\mathbf{q}^{(i)}$ can be calculated analytically

$$\begin{bmatrix} a_l^{(i)} \\ d_l^{(i)} \end{bmatrix} = (\mathbf{C}_l^T \mathbf{C}_l)^{-1} \mathbf{C}_l^T \mathbf{F}_l \quad (4.12)$$

$$\begin{bmatrix} a_d^{(i)} \\ d_d^{(i)} \end{bmatrix} = (\mathbf{C}_d^T \mathbf{C}_d)^{-1} \mathbf{C}_d^T \mathbf{F}_d$$

where

$$\mathbf{C}_l = \begin{bmatrix} C_{l,c}(\mathbf{x}^{(0)}) & C_{l,c}(\mathbf{x}^{(1)}) & \cdots & C_{l,c}(\mathbf{x}^{(i)}) \\ 1 & 1 & \cdots & 1 \end{bmatrix}^T \quad (4.13)$$

$$\mathbf{F}_l = \begin{bmatrix} C_{l,f}(\mathbf{x}^{(0)}) & C_{l,f}(\mathbf{x}^{(1)}) & \cdots & C_{l,f}(\mathbf{x}^{(i)}) \\ 1 & 1 & \cdots & 1 \end{bmatrix}^T$$

and

$$\mathbf{C}_d = \begin{bmatrix} C_{d,c}(\mathbf{x}^{(0)}) & C_{d,c}(\mathbf{x}^{(1)}) & \cdots & C_{d,c}(\mathbf{x}^{(i)}) \\ 1 & 1 & \cdots & 1 \end{bmatrix}^T \quad (4.14)$$

$$\mathbf{F}_d = \begin{bmatrix} C_{d,f}(\mathbf{x}^{(0)}) & C_{d,f}(\mathbf{x}^{(1)}) & \cdots & C_{d,f}(\mathbf{x}^{(i)}) \\ 1 & 1 & \cdots & 1 \end{bmatrix}^T$$

That is the least-square optimal solution to the linear regression problem $\mathbf{C}_l a_l^{(i)} + d_l^{(i)} = \mathbf{F}_l$ and $\mathbf{C}_d a_d^{(i)} + d_d^{(i)} = \mathbf{F}_d$, equivalent to equation 4.17

4.6 Surrogates via Mixed Modeling

The surrogate model constructed for the mixed modeling approach were the same as in 4.5, except the low-fidelity model $\mathbf{c}(\mathbf{x})$ is replaced by the approximation Kriging model $\tilde{\mathbf{s}}$. Then the output space mapping surrogate, equivalent to equation 4.15 will be

$$\mathbf{s}^{(i)}(\mathbf{x}) = \mathbf{A}^{(i)} \circ \tilde{\mathbf{s}}(\mathbf{x}) + \mathbf{D}^{(i)} + \mathbf{q}^{(i)} = \begin{bmatrix} a_l^{(i)} C_{l.c}(\mathbf{x}) + d_l^{(i)} + q_l^{(i)} & a_d^{(i)} C_{d.c}(\mathbf{x}) + d_d^{(i)} + q_d^{(i)} \end{bmatrix}^T, \quad (4.15)$$

and the response correction parameters $\mathbf{A}^{(i)}$ and $\mathbf{D}^{(i)}$ are obtained by solving

$$\left[\mathbf{A}^{(i)}, \mathbf{D}^{(i)} \right] = \arg \min_{[\mathbf{A}, \mathbf{D}]} \sum_{k=0}^i \left\| \mathbf{f}(\mathbf{x}^{(k)}) - \mathbf{A} \circ \tilde{\mathbf{s}}(\mathbf{x}^{(k)}) + \mathbf{D} \right\|^2. \quad (4.16)$$

Then the additive response correction term $\mathbf{q}^{(i)}$ is defined as

$$\mathbf{q}^{(i)} = \mathbf{f}(\mathbf{x}^{(i)}) - \left[\mathbf{A}^{(i)} \circ \tilde{\mathbf{s}}(\mathbf{x}^{(i)}) + \mathbf{D}^{(i)} \right]. \quad (4.17)$$

The response correction parameters $\mathbf{A}^{(i)}$ and $\mathbf{D}^{(i)}$ are obtained analytically as in 4.5.

Chapter 5

Results

This chapter gives the results of numerical optimization of trawl-door shapes using the methodology presented in Chapter 4. The first section gives results of performing local search using the multi-point space mapping algorithm (Chapter 4.5) for lift-constrained drag minimization, and lift-to-drag maximization. The second section gives results of global search using mixed modeling (Chapter 4.6) for lift-to-drag maximization. The chapter ends with discussion and comparison of the approaches.

5.1 Local Search Using Multi-Point Space Mapping

5.1.1 Lift-Constrained Drag Minimization with Main Element and Leading-Edge Slat

In following optimization run consisting of a main element and leading edge slat, the high-fidelity model were selected with about 517,000 elements (grid 9). The flow solver convergence criteria were set to 5,000 iterations, or when residuals had dropped by six orders of magnitude. The low-fidelity model were the same as the high-fidelity one, but with coarser mesh discretization and relaxed convergence criteria. The selected grid had about 15,000 elements (grid 4) and the model were considered converged after fixed number of 500 iterations. The low fidelity model resulted in being around 78 times faster than the high-fidelity one.

The objective is to minimize the drag coefficient C_d subject to constraint on the section lift coefficient, $C_l \geq 1.2$. The design variables are x_{slat}/c and y_{slat}/c locations of the leading edge of the slat with respect to the main element leading edge, rotation of the slat

θ with respect to the main-element chord line and the angle attack α . The search domain were set as: $-0.35 \leq x_{flap}/c \leq -0.17$, $-0.08 \leq y_{flap}/c \leq 0.07$, $10 \leq \theta_{flap} \leq 40$ deg, $5.0 \leq \alpha \leq 35$ deg. The initial design were $x_{flap}/c = -0.2$, $y_{flap}/c = -0.08$, $\theta_{flap} = 25$ deg and $\alpha = 8$ deg.

The optimization results are shown in table 5.1, and the initial and optimized trawl-door shapes are shown in figure 5.1. The optimized design has $x_{slat}/c = -0.200$, $y_{slat}/c = -0.0633$, $\theta_{slat} = 24.1$ deg, and $\alpha = 8.4$ deg, with $C_l = 1.20$ and $C_d = 0.0153$ giving a lift-to-drag ratio of 78.4. Compared to the initial design that has $C_l = 1.13$ and $C_d = 0.015$ giving a lift-to-drag ratio of 74.4, the lift coefficient has increased about 6.2% and the drag coefficient stays similar between the designs, resulting in an increase of approximately 5.2% of the lift-to-drag ratio. The SM optimizer required 14 high-fidelity model evaluations and 400 low-fidelity ones, yielding a total runtime of approximately 55 hours. Figure 5.2 shows convergence history of the optimization process. Initially the design is infeasible but the optimizer quickly approaches the lift constraint value and finally converges on the objective value change after 11 iterations.

Table 5.2 shows the optimized results compared to previous study of this particular problem from Leifsson *et al.* [10] using local surrogates, constructed from high-fidelity models. The previous design is improved significantly, where the drag coefficient is reduced by 12.2 % while the lift coefficient is held similar due to constraints, resulting in a increase of the lift-to-drag ratio of approximately 12.2%. Previous study required 110 high-fidelity evaluations to converge compared to 14 high-fidelity and 400 low-fidelity ones by the SM algorithm, resulting in reduction of the optimization cost by 79%.

Table 5.1: Comparison of initial and optimized results of a trawl-door with a main element and leading edge slat. The objective is to minimize C_d subject to constraint on the section lift coefficient using multi-point space mapping

	Initial	Optimized	Relative difference
x/c_{slat}	-0,200	-0,200	-
y/c_{slat}	-0,080	-0,063	-
θ	25,00	24,11	-
α	8,000	8,375	-
C_l	1,126	1,200	6.2%
C_d	0,015	0,015	0%
C_l/C_d	74,38	78,44	5.2%
Evaluations HF/LF	-	14/400	-
Runtime gain ratio	-	≈ 78	-
Total runtime [hours]	-	≈ 55	-

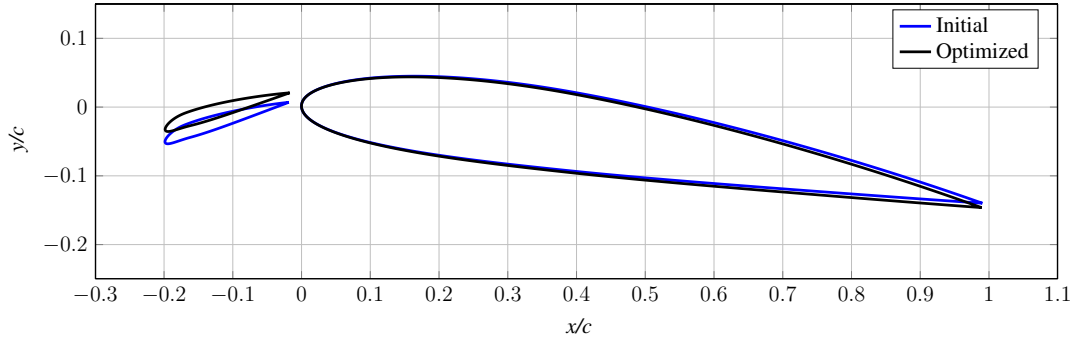
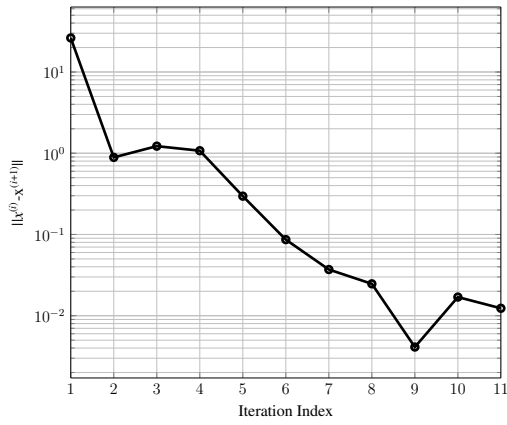
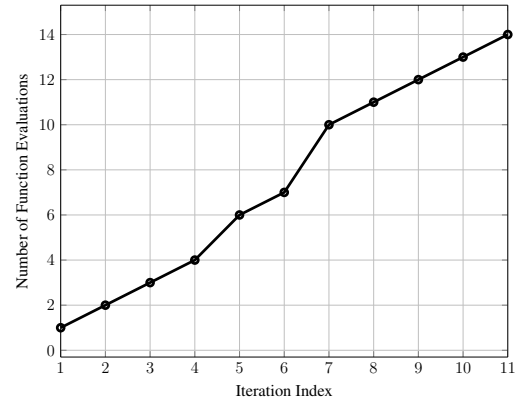


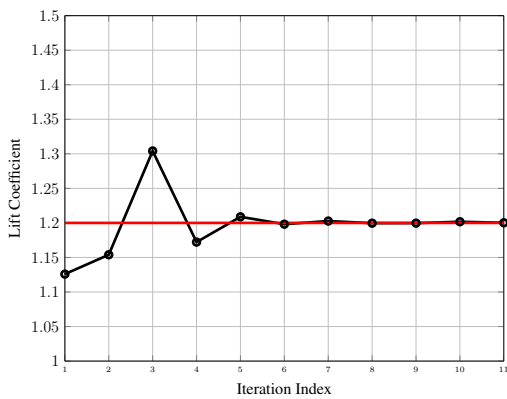
Figure 5.1: Comparison of initial and optimized trawl-door shape of a trawl-door with main element and leading edge slat. The objective is to minimize C_d subject to constraint on the section lift coefficient using multi-point space mapping. The flow is parallel to the x/c axis



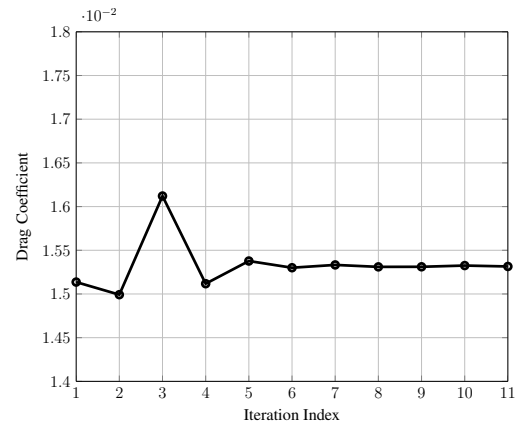
(a) Argument convergence



(b) Number of high-fidelity function evaluations



(c) Evolution of the lift coefficient and the constraint bound



(d) Evolution of the drag coefficient

Figure 5.2: Optimization history of a trawl-door with main element and a leading edge slat. The objective is to minimize C_d subject to constraint on the section lift coefficient using multi-point space mapping.

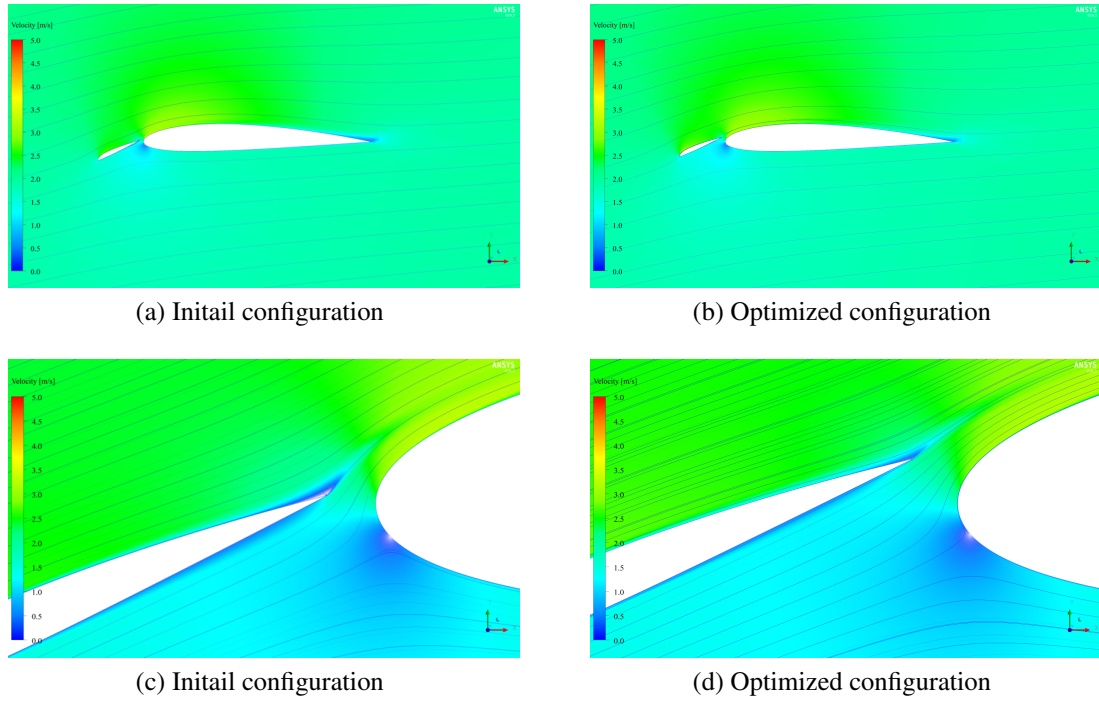


Figure 5.3: Flow velocity contour plots for initial and optimized wing configurations of a trawl-door with main element and leading edge slat. The objective is to minimize C_d subject to constraint on the section lift coefficient using multi-point space mapping.

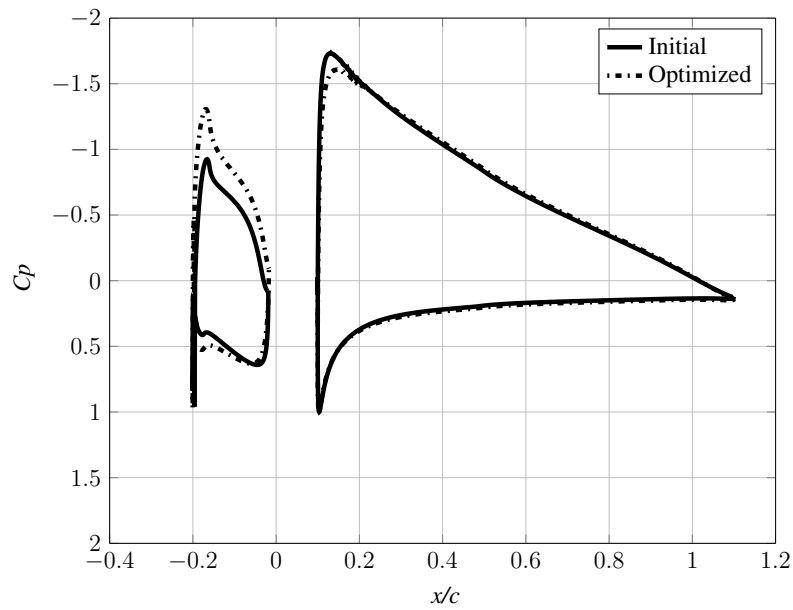


Figure 5.4: Pressure distribution comparison between initial and optimized shapes of a trawl-door with main element and leading-edge slat. The objective is to minimize C_d subject to constraint on the section lift coefficient using multi-point space mapping.

Table 5.2: Comparison of SM optimization results with approach using local surrogates

	Previous study [39]	Current results	Relative difference
$\mathbf{x}/\mathbf{c}_{\text{slat}}$	-0,2289	-0,200	-
$\mathbf{y}/\mathbf{c}_{\text{slat}}$	-0,0066	-0,063	-
θ	20,4968	24,11	-
α	8,2758	8,375	-
C_l	1,1985	1,200	0.1%
C_d	0,0174	0,015	-13,7%
C_l/C_d	68,8793	78,44	12,2%
Iterations	9	11	-
Evaluations HF/LF	110	14/400	-
Total runtime [hours]	≈ 262	≈ 55	-79.0%

5.1.2 Lift-to-Drag Maximization with Main Element and Leading-Edge Slat

Following optimization run has the same trawl-door geometry as the case before. The high-fidelity model were selected with about 517,000 elements (grid 9). The flow solver convergence criteria were set to 5,000 iterations, or when residuals had dropped by six orders of magnitude. The low-fidelity model were the same as the high-fidelity one, but with coarser mesh discretization and relaxed convergence criteria. The selected grid had about 50,000 elements (located between grid points 5 and 6) and the model were considered converged after 2,000 iterations, or when residuals had dropped by 4 orders in magnitude. The low fidelity model resulted in being around 18 times faster than the high-fidelity one.

The objective is to maximize the lift-to-drag ratio C_l/C_d with no additional constraints. The design variables are x_{slat}/c and y_{slat}/c locations of the leading edge of the slat with respect to the main element leading edge, rotation of the slat θ with respect to the main-element chord line and the angle attack α . The search domain were set as: $-0.40 \leq x_{slat}/c \leq -0.20$, $-0.08 \leq y_{slat}/c \leq 0.03$, $20 \leq \theta_{slat} \leq 50$ deg, $0.0 \leq \alpha \leq 20$ deg. The initial design were $x_{slat}/c = -0.2$, $y_{slat}/c = -0.08$, $\theta_{slat} = 25$ deg and $\alpha = 5$ deg.

The optimization results are shown in table 5.3, and the initial and optimized trawl-door shapes are shown in figure 5.5. The optimized design has $x_{slat}/c = -0.200$, $y_{slat}/c = -0.0800$, $\theta_{slat} = 29.3$ deg, and $\alpha = 12.3$ deg, with $C_l = 1.67$ and $C_d = 0.0204$ giving a lift-to-drag ratio of 81.8. Compared to the initial design that has $C_l = 0.699$ and $C_d = 0.0185$ giving a lift-to-drag ratio of 37.8, the lift coefficient has increased about 58.1% and the drag coefficient increased about 9.31%, resulting in an increase of approximately 53.8% of the lift-to-drag ratio. The SM optimizer required 4 high-fidelity model evaluations and 83 low-fidelity ones, yielding a total runtime of approximately 19 hours. Figure 5.7 shows convergence history of the optimization process. Initially the design is infeasible but the optimizer approaches more feasible solution after only two iterations and converges on the objective value after 4 iterations.

Table 5.3: Comparison of initial and optimized results of a trawl-door with a main element and leading edge slat. The objective is to maximize C_l/C_d with no additional constraints using multi-point space mapping

	Initial	Optimized	Relative difference
$\mathbf{x}/c_{\text{slat}}$	-0.200	-0.200	-
$\mathbf{y}/c_{\text{slat}}$	-0.0800	-0.0800	-
θ	25.0	29.3	-
α	5.00	12.3	-
C_l	0.699	1.67	58.1%
C_d	0.0185	0.0204	9.31%
C_l/C_d	37.8	81.8	53.8%
Iterations	-	4	-
Evaluations HF/LF	-	4/83	-
Runtime gain ratio	-	≈ 18	-
Total runtime [hours]	-	≈ 19	-

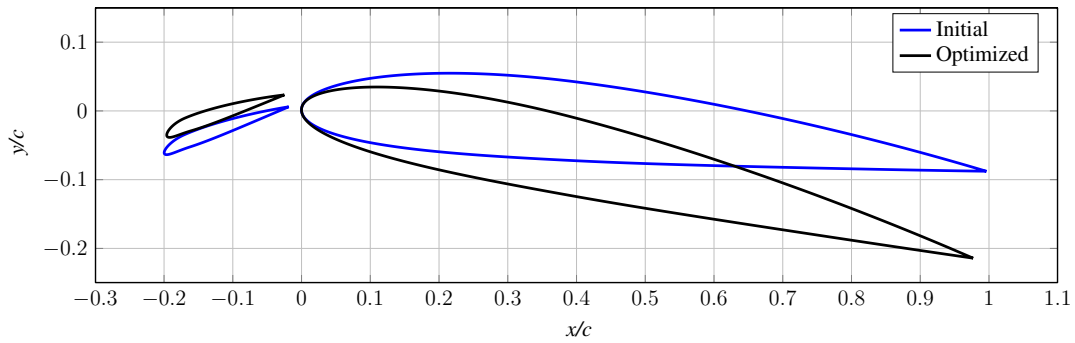
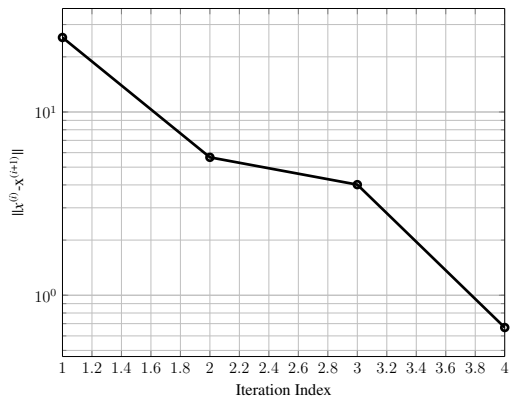
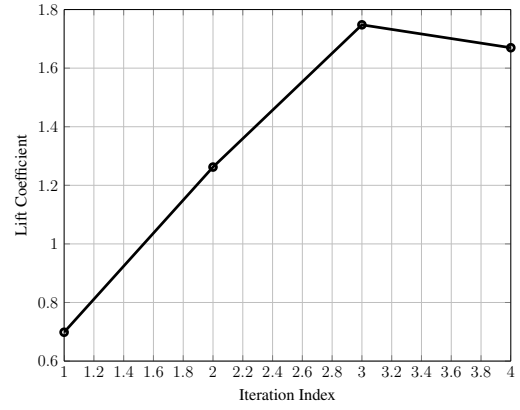


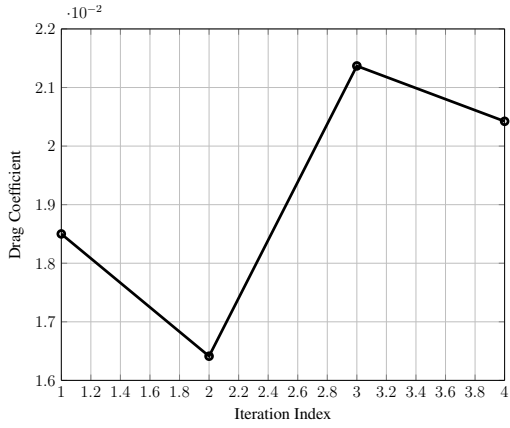
Figure 5.5: Comparison of initial and optimized trawl-door shape of a trawl-door with main element and leading edge slat. The objective is to maximize C_l/C_d with no additional constraints, using multi-point space mapping. The flow is parallel to the x/c axis



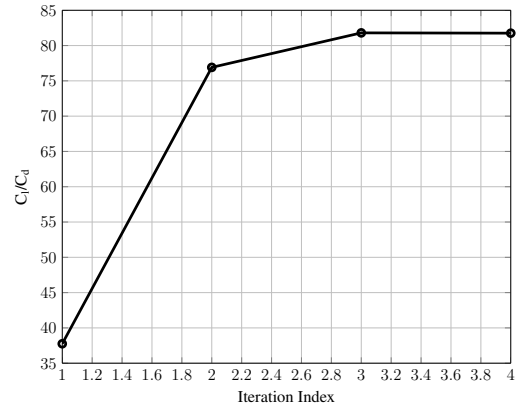
(a) Argument convergence



(b) Evolution of the lift coefficient



(c) Evolution of the drag coefficient



(d) Evolution of lift over drag

Figure 5.6: Lift-to-Drag optimization history of a trawl-door with main element and leading-edge slat. The objective is to maximize C_l/C_d with no additional constraints, using multi-point space mapping.

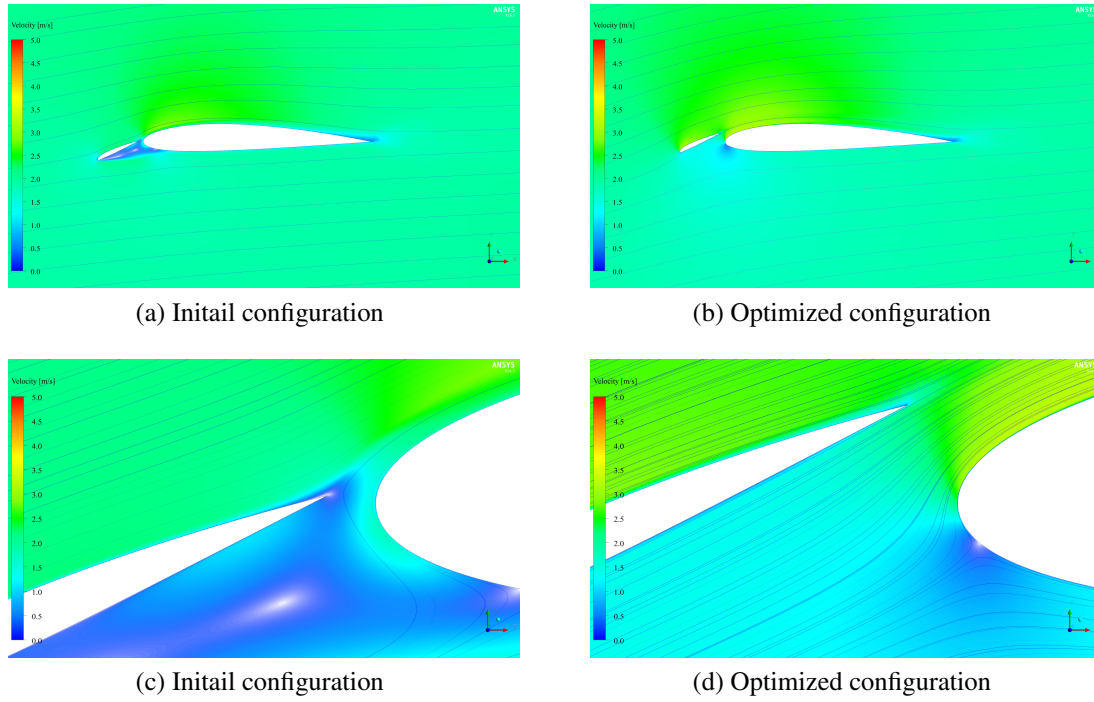


Figure 5.7: Flow velocity contour plots for initial and optimized wing configurations of a trawl-door with main element and leading-edge slat. The objective is to maximize C_l/C_d with no additional constraints, using multi-point space mapping.

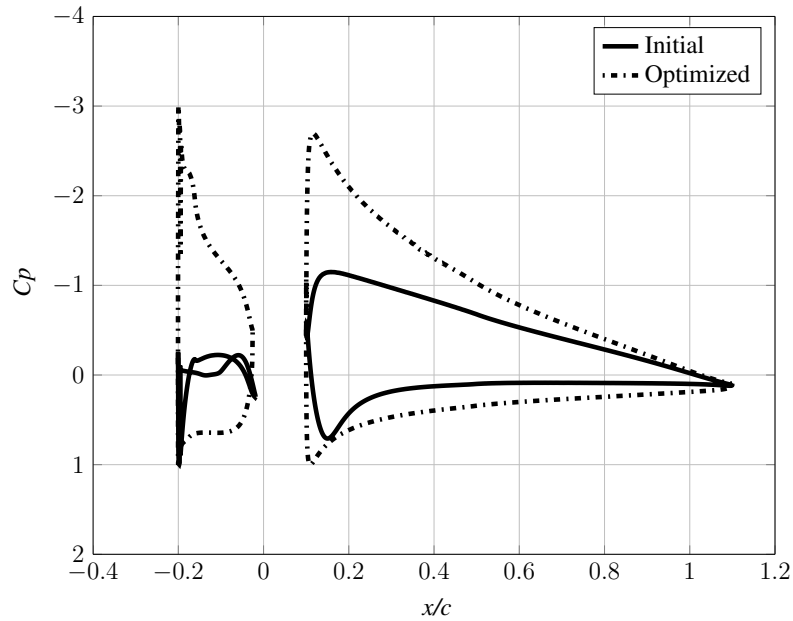


Figure 5.8: Pressure distribution comparison between initial and optimized shapes of a trawl-door with main element and leading-edge slat. The objective is to maximize C_l/C_d with no additional constraints, using multi-point space mapping.

5.1.3 Lift-to-Drag Maximization With Main Element, Leading Edge Slat, and Trailing-Edge Flap

Following optimization run consists of a trawl-door with main element, leading edge slat and trailing-edge flap. The High-fidelity model selected were with approximately 315,000 elements (grid 8). The flow solver convergence criteria were set to 6,000 iterations, or when residuals had dropped by five orders of magnitude. The low-fidelity model were the same as the high-fidelity one, but with coarser mesh discretization and relaxed convergence criteria. The selected grid had about 60,000 elements (located between grid points 5 and 6) and the model were considered converged after 2,000 iterations, or when residuals had dropped by 4 orders in magnitude. The low fidelity model resulted in being around 15 times faster than the high-fidelity one.

The objective is maximize the lift-to-drag ratio C_l/C_d with no additional constraints. The design variables are x_{slat}/c and y_{slat}/c locations of the leading edge of the slat with respect to the main element leading edge, rotation of the slat θ_{slat} with respect to the main-element chord line, x_{flap}/c and y_{flap}/c locations of the leading edge of the flap with respect to the main element leading edge, rotation of the flap θ_{flap} with respect to the main-element chord line, and the angle attack α .

The search domain were set as: $-0.40 \leq x_{slat}/c \leq -0.20$, $-0.30 \leq y_{slat}/c \leq 0.30$, $20 \leq \theta_{slat} \leq 50$ deg, $0.90 \leq x_{flap}/c \leq 1.20$, $-0.20 \leq y_{flap}/c \leq 0.00$, $-30 \leq \theta_{flap} \leq 0$ deg, $0.0 \leq \alpha \leq 15$ deg. The initial design were based on previously optimized results where the configuration of the flap and slat were optimized independently. The were chosen as: $x_{slat}/c = -0.20$, $y_{slat}/c = -0.0633$, $\theta_{slat} = 24.1$ deg, $x_{flap}/c = 1.00$, $y_{flap}/c = -0.0222$, $\theta_{flap} = -17.3$ deg, $\alpha = 8$ deg.

The optimization results are shown in table 5.4, and the initial and optimized trawl-door shapes are shown in figure 5.9. The optimized design has $x_{slat}/c = -0.200$, $y_{slat}/c = -0.0630$, $\theta_{slat} = 27.1$ deg, $x_{flap}/c = 1.00$, $y_{flap}/c = -0.0222$, $\theta_{flap} = -18.3$ deg and $\alpha = 6.00$ deg, with $C_l = 2.23$ and $C_d = 0.0230$ giving a lift-to-drag ratio of 97.2. Compared to the initial design that has $C_l = 2.46$ and $C_d = 0.0275$ giving a lift-to-drag ratio of 89.6, the lift coefficient has decreased about 10.3% and the drag coefficient decreased even more, or about 10.6% resulting in an increase of approximately 7.82% of the lift-to-drag ratio. The SM optimizer required 4 high-fidelity model evaluations and 90 low-fidelity ones, yielding a total runtime of approximately 22 hours. Figure 5.10 shows convergence history of the optimization process. The lift-to-drag ratio increases gradually as the optimizer approaches more feasible solution. After only 4 iterations the optimizer converges after the objective value falls within numerical noise level.

Table 5.4: Comparison of initial and optimized results of a trawl-door with a main element, leading edge slat and trailing edge flap. The objective is to maximize C_l/C_d with no additional constraints using multi-point space mapping

	Initial	Optimized	Relative difference
x/c_{slat}	-0.200	-0,200	-
y/c_{slat}	-0.0633	-0,0633	-
θ_{slat}	24.1	27,1	-
x/c_{flap}	1.00	1,00	-
y/c_{flap}	-0.0222	-0.0222	-
θ_{flap}	-17.3	-18.3	-
α	8,000	6.00	-
C_l	2.46	2.23	-10.3%
C_d	0.0275	0.0230	-19.6%
C_l/C_d	89.6	97.2	7.82%
Iterations	-	4	-
Evaluations HF/LF	-	4/90	-
Runtime gain ratio	-	≈ 15	-
Total runtime [hours]	-	≈ 22	-

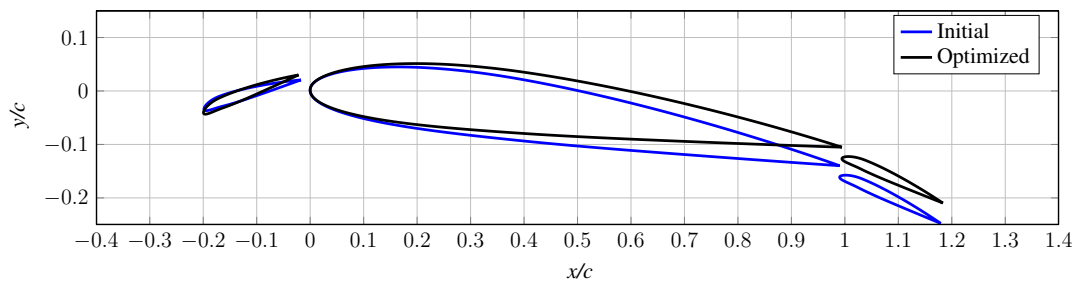
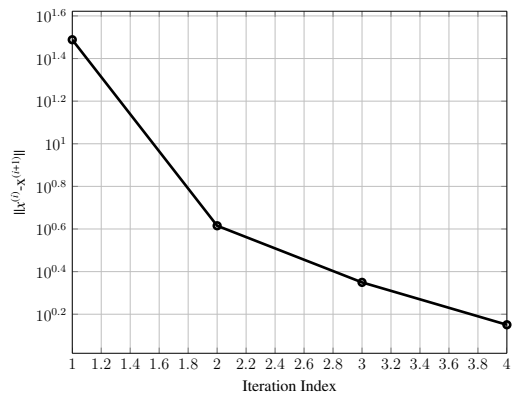
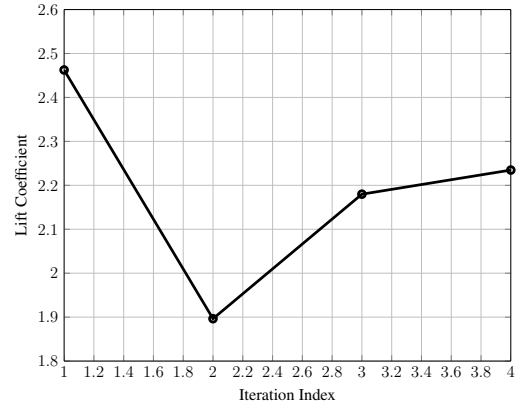


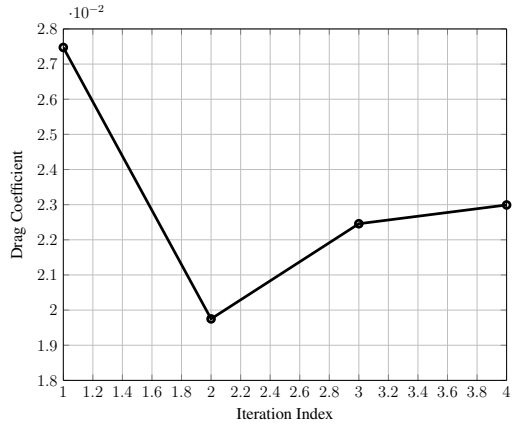
Figure 5.9: Comparison of initial and optimized trawl-door shape of a trawl-door with main element, leading edge slat and trailing edge flap. The objective is to maximize C_l/C_d with no additional constraints, using multi-point space mapping. The flow is parallel to the x/c axis



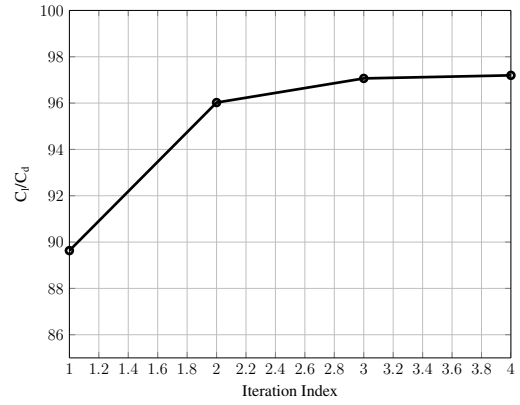
(a) Argument convergence



(b) Evolution of the lift coefficient



(c) Evolution of the drag coefficient



(d) Evolution of lift over drag

Figure 5.10: Lift-to-Drag optimization history of a trawl-door with main element, leading-edge slat and trailing edge flap. The objective is to maximize C_l/C_d with no additional constraints, using multi-point space mapping.

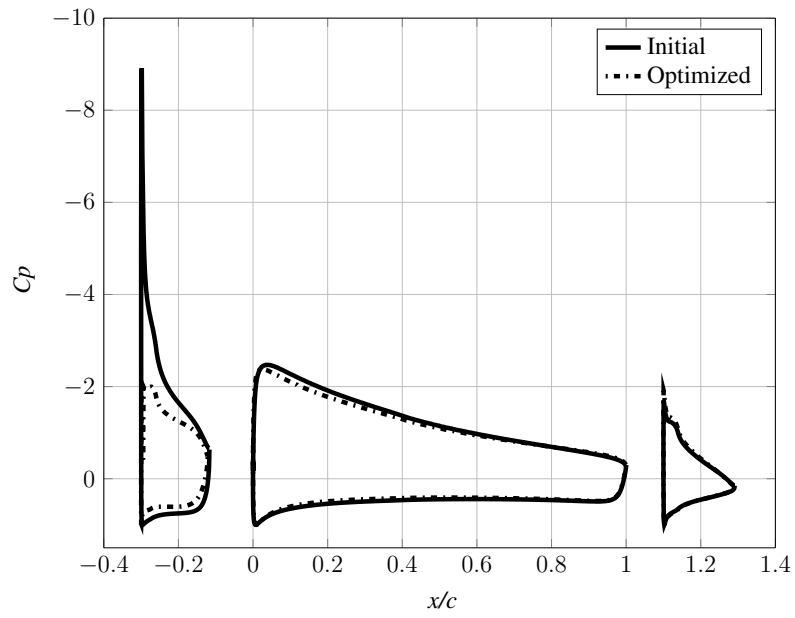


Figure 5.11: Pressure distribution comparison between initial and optimized shapes of a trawl-door with main element, leading-edge slat and trailing edge flap. The objective is to maximize C_l/C_d with no additional constraints, using multi-point space mapping.

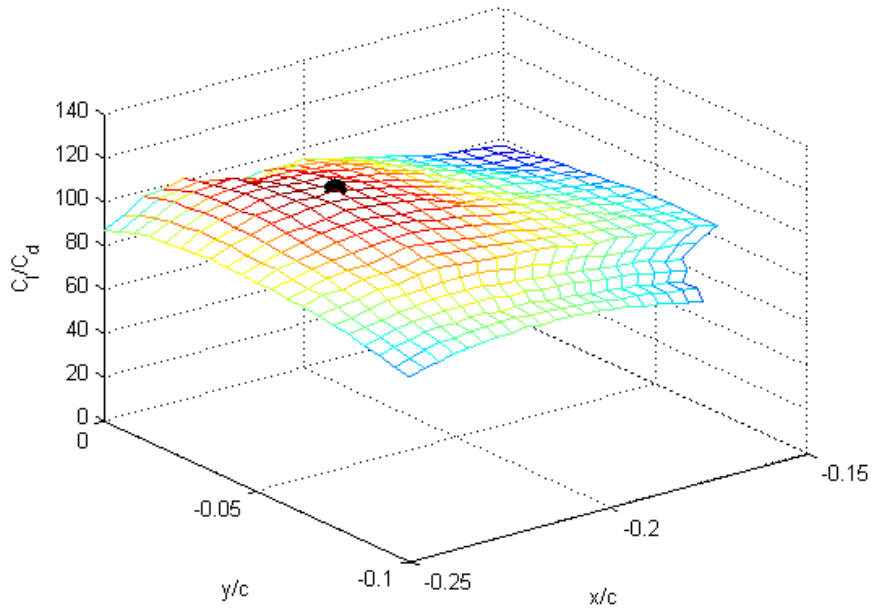
5.2 Global Search Using Mixed Modeling

5.2.1 Lift-to-Drag Maximization With Main Element and Leading-Edge Slat

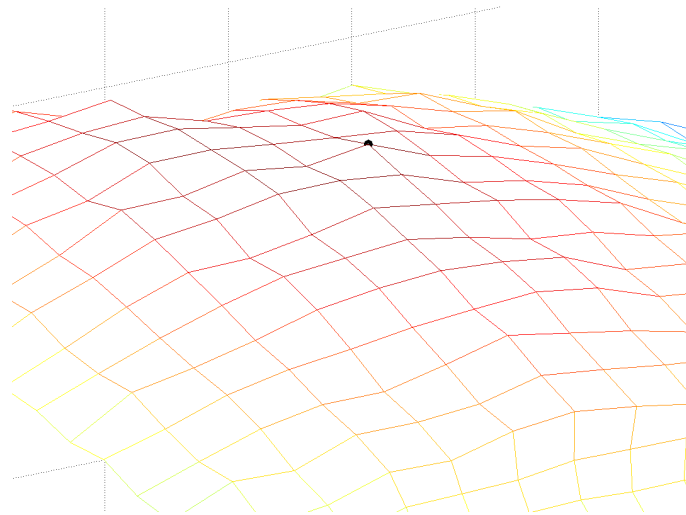
One trawl-door geometry consisting of a main element and leading edge slat were optimized using Kriging interpolation as a surrogate model. The low-fidelity model used to construct the kriging model were the same as used in chapter 5.1.2, with approximately 50,000 elements, and considered converged after 2,000 iterations or after the residuals have dropped by 4 orders in magnitude. 900 low-fidelity evaluations were used to construct the model.

The objective is to maximize the lift-to-drag ratio C_l/C_d with no additional constraints. The design variables are x_{slat}/c and y_{slat}/c locations of the leading edge of the slat with respect to the main element leading edge, rotation of the slat θ with respect to the main-element chord line and the angle attack α . The model were constructed within upper and lower bounds of $-0.25 \leq x_{slat}/c \leq -0.15$, $-0.10 \leq y_{slat}/c \leq 0.00$, $20 \leq \theta_{slat} \leq 30$ deg, $5.0 \leq \alpha \leq 15$ deg.

The optimization results are shown in table 5.5 and figure 5.12 shows a slice parallel to the x_{slat}/c , y_{slat}/c surface of the Kriging model at optimum location of θ and α , where a black dot represents the optimum design on the surface. The optimized design has $x_{slat}/c = -0.205$, $y_{slat}/c = -0.0558$, $\theta_{slat} = 25.5$ deg, and $\alpha = 10.7$ deg, with $C_l = 1.48$ and $C_d = 0.0180$ giving a lift-to-drag ratio of 82.8 and the optimum trawl-door shape can be seen on figure 5.14. Figure 5.13 shows similar slices through the Kriging model as before, but at proximity of the optimum design.



(a) The black dot represents the optimum solution

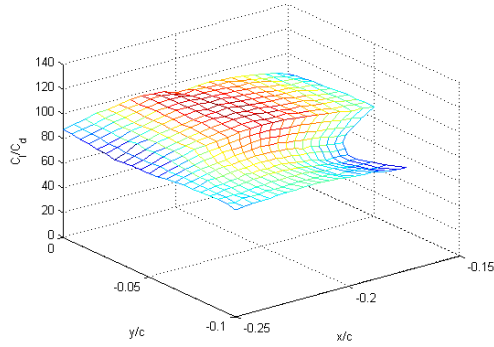


(b) Closer view

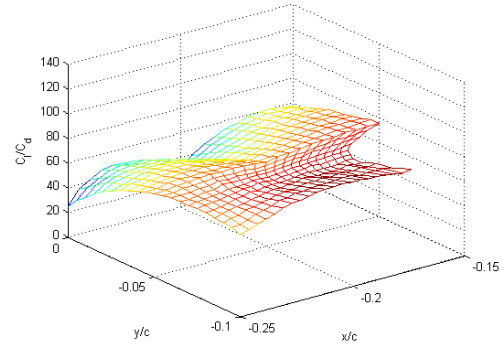
Figure 5.12: Slice parallel to the $x_{slat}/c, y_{slat}/c$ surface of the Kriging model at optimum location of $\theta = 20.5$ and $\alpha = 10.7$.

Table 5.5: Optimized results of a trawl-door with a main element and leading edge slat. The objective is to maximize C_l/C_d with no additional constraints using mixed modeling

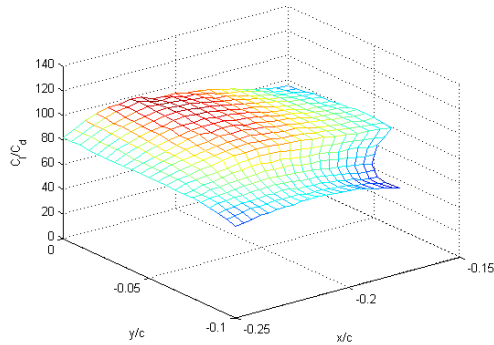
Optimized	
x/c_{slat}	-0.205
y/c_{slat}	-0.0558
θ_{slat}	25.5
α	10,7
C_l	1.48
C_d	0.0180
C_l/C_d	82.1
Evaluations HF/LF	1/900
Total runtime [hours]	67



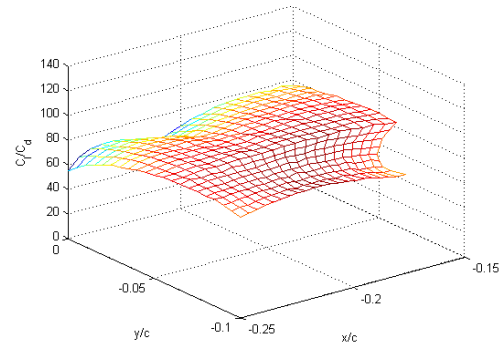
(a) $\theta = 25, \alpha = 8$



(b) $\theta = 25, \alpha = 14$



(c) $\theta = 28, \alpha = 8$



(d) $\theta = 28, \alpha = 14$

Figure 5.13: Slices parallel to the $x_{\text{slat}}/c, y_{\text{slat}}/c$ surface of the Kriging model at proximity of optimum design of θ and α

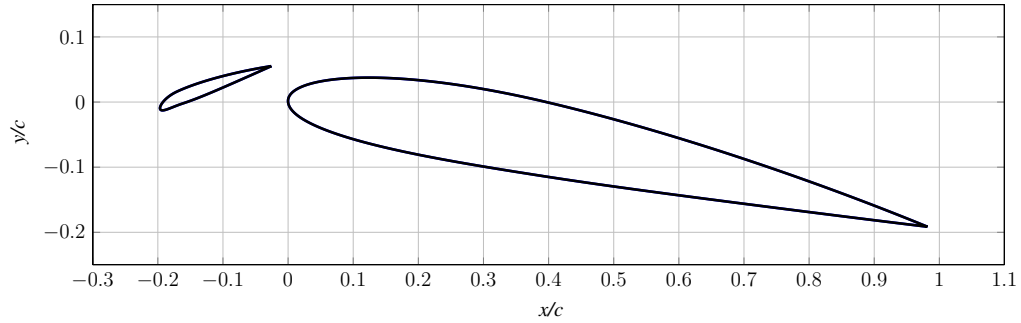


Figure 5.14: Optimized trawl-door shape of a trawl-door with main element and leading edge slat. The objective is to maximize C_l/C_d with no additional constraints, using mixed modeling. The flow is parallel to the x/c axis

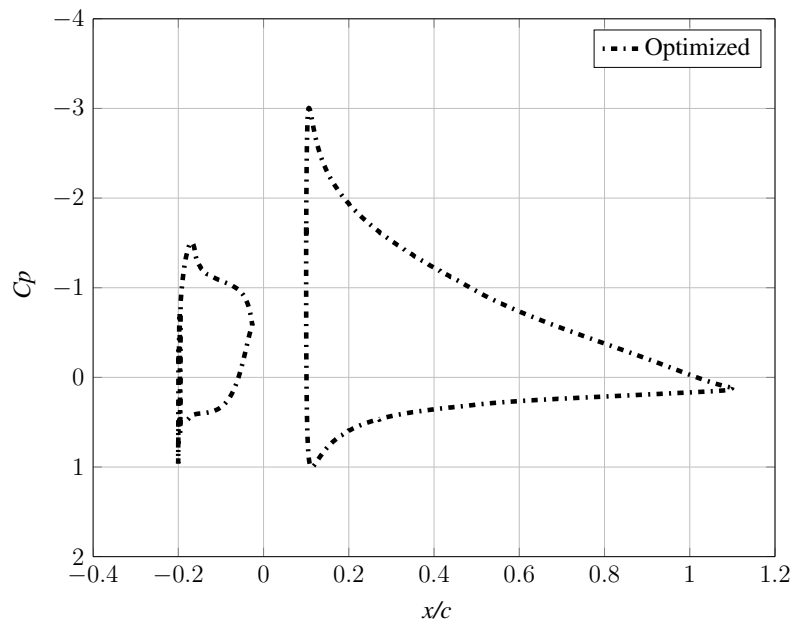


Figure 5.15: Pressure distribution over optimized shape of trawl-door with main element and leading-edge slat. The objective is to maximize C_l/C_d with no additional constraints, using mixed modeling.

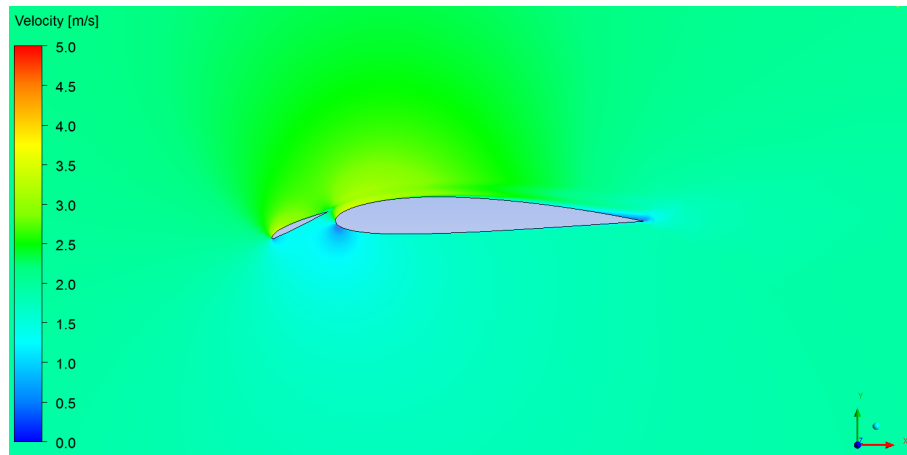


Figure 5.16: Velocity contour plot of the optimized design of trawl-door with main element and leading-edge slat. The objective is to maximize C_l/C_d with no additional constraints, using mixed modeling.

5.3 Discussion

When all optimization results for a trawl-door with main element and leading edge slat are examined, they all yield satisfactory results. In all of the cases, optimum result for design variable x_{slat}/c is within the range of $-0.200 \leq x_{slat}/c \leq -0.205$ and y_{slat}/c within $-0.0558 \leq x_{slat}/c \leq -0.0800$ whether the objective is to maximize C_l/C_d or minimize C_d . Even though the consistency is not as good between simulation results for design variables θ and α , the solutions are considered valid. The reason is that there are more than one equally good solutions for the problem being solved. Table 5.6 summarizes the optimization results.

The highest lift-to-drag ratio of 82.1 is obtained by using mixed modelling methods. However the difference between the two methods is negligible considering the noise analysis conducted in chapter 3.6, where the noise in the high-fidelity model was found to be up to $0.80 C_l/C_d$ in design variable x_{slat}/c . The case where the objective is to minimize C_d for given lift is not considered comparable in context of lift-to-drag values. Even though the nature of the problem requires the solution to be on top part of the lift-to-drag curve it is not constraint to the highest point. If case of a trawl-door with both leading-edge slat and trailing-edge flap is taken into account it, as expected obtains the highest lift-to-drag ratio of 97.2.

If computational efficiency of the optimization runs is examined, the Kriging model needs the longest computational time. Then reason is the high number of low-fidelity evaluations, even though the low-fidelity model is computationally inexpensive compared to the high-fidelity one the high number of 900 evaluations take over 63 hours to compute. The advantages to this method are that number of evaluations are directly related to the size of the design space (i.e. Smaller design space equals fewer evaluations). Another advantage is that only one high-fidelity evaluation is needed after the Kriging model has been constructed.

There is also much difference in computational time of the optimization process using multi-point SM. The case that minimizes C_d needs much higher number of both low- and high-fidelity evaluations. In that optimization run the low-fidelity model is of poorer quality than in other cases, but instead the computational time for each low-fidelity evaluation is much smaller. This difference is also effected by the objective value needed for the model to be converged. The objective is to minimize C_d that is a value, very close to zero and does not inherit much noise. That means that the solution value change has to be set to very small value (0.001) for the optimization process to be converged. When maximizing C_l/C_d , the objective value convergence criteria has to be relaxed so that the value is

Table 5.6: Comparison of all optimum designs of a trawl-door with main element and leading-edge slat

	Local Search I	Local Search II	Global Search
Objective	$\min C_d, Cl \geq 1.2$	$\max C_l/C_d$	$\max C_l/C_d$
$\mathbf{x}/\mathbf{c}_{\text{slat}}$	-0.200	-0.200	-0.205
$\mathbf{y}/\mathbf{c}_{\text{slat}}$	-0.0630	-0.0800	-0.0558
θ	24.1	29.3	-25.5
α	8.38	12.3	-10.7
C_l	1.20	1.67	1.48
C_d	0.0150	0.0204	0.0180
C_l/C_d	78.4	81.8	82.1
Evaluations HF/LF	14/400	4/83	1/900
Runtime gain ratio	≈ 78	≈ 18	-
Total runtime [hours]	≈ 55	≈ 19	≈ 67

close to the noise in C_l/C_d . According to noise analysis of the low-fidelity used in case of C_l/C_d maximization, the numerical noise is around 1.3 C_l/C_d making the model easier to converge.

Chapter 6

Conclusion

Robust and efficient optimization framework for the hydrodynamic design of multi-element trawl-door shapes using accurate high-fidelity two-dimensional computational fluid dynamics (CFD) models are presented in this thesis. The particular contributions of the work are as follows:

- Robust grid generation for multi-element hydrofoils has been developed. Thus, the CFD analysis becomes stable and accurate enough to capture the nonlinear fluid flow past the hydrofoils. Moreover, the robust CFD analysis makes the surrogate-based optimization (SBO) process smoother.
- A problem formulation capturing the true characteristics of the design space has been presented. The objective function is transformed from a constrained one to an unconstrained one by maximizing the lift-to-drag ratio in place of minimizing the drag for a given lift. The proposed formulation creates a design space which is easier to search using SBO.
- Surrogate construction using mixed modeling has been applied to the global optimization of trawl-door shapes. The approach utilizes space mapping to create a fast physics-based surrogate model using low- and high-fidelity data. The surrogate is then used to build an approximation-based surrogate model using kriging to search the design space globally.

Numerical design studies of multi-element trawl-door shapes using the framework illustrate the following:

- Lift-to-drag maximization is more appropriate than lift-constrained drag minimization for trawl-door shape optimization.

- Local search using multi-point space mapping very efficient and can yield satisfactory design at a low cost.
- Global search using mixed modeling is more computationally expensive than local search using multi-point space mapping but is capable of yielding designs with higher quality. The mixed modeling approach, however, provides a cost-effective way of performing global search. Using only high-fidelity data would be impractical.

Future work in this research area could consider the following:

- Three-dimensional CFD models need to be developed to capture more accurately the nonlinear flow physics of trawl-doors, especially due to the tip vortex shedding.
- Rigorous model validation is needed. In particular, experimental data for trawl-door shapes is required for the validation. A combination of wind tunnel experiments (which can be cheap and fast using the wind tunnels at Reykjavik University and rapid prototyping using, for example, three-dimensional printing) and tow-tank experiments (which are more time consuming and expensive since a such facility is not available in Iceland) can be used.
- The three-dimensional CFD model simulation time is expected to be at least an order of magnitude higher. Thus, search using multi-point space mapping would be promising, especially if faster low-fidelity models can be developed. Simplified physics models, such as panel methods, should be considered. The mixed modeling approach can be used, but it should be used in a quasi-global-way, i.e., when a promising design has been identified the mixed modeling approach can be used to build a surrogate to investigate the vicinity and accurately find the optimum design.
- Adjoint sensitivity information can be used to build more accurate surrogate models (both for local and global search) as well as accelerating the optimization process. Additionally, larger design spaces can be handled. The Stanford University Unstructured code, which is open-source, can be used for the flow simulations and calculating the adjoints.
- Unsteady CFD simulations should be considered to capture more accurately loads acting on the trawl-doors. This will support more accurate structural design when it comes to manufacturing.

References

- [1] I. Abbot and A. Von Doenhoff, *Theory of Wing Sections, Including a Summary of Airfoil Data*. Dover Publications, 1959.
- [2] C. Ladson, “Effects of independent variation of mach and reynolds numbers on the low-speed aerodynamic characteristics of the naca 0012 airfoil section,” NASA, Tech. Rep., 1988.
- [3] L. Leifsson and S. Koziel, *Simulation-Driven Aerodynamic Design using Variable-Fidelity Models*. Imperial Collage Press, 2015.
- [4] “The 2013 annual economic report on the eu fishing fleet (STECF-13-15),” Scientific, Technical and Economic Committee for Fisheries (STECF), Tech. Rep., 2013.
- [5] A. Campos, T. Pilar-Fonseca, J. Parente, and P. Fonseca, “Fuel efficiency in trawlers under different fishing tactics using a consumption model and vms data: A case-study for the Portuguese fleet,” in *Martech - International Conference on Maritime*, 2011.
- [6] *Basic Fishing Methoods*, Seafish, Fisheries Development Centre, 2005. [On-line]. Available: http://www.seafish.org/media/Publications/Basic_Fishing_Gear_Booklet_May05.pdf
- [7] Injector, “Creating value trough innovative trawl door technology.”
- [8] R. D. Galbraith, A. Rice, and E. S. Strange, “An introduction to commercial fishing gear and methods used in scotland,” 2004.
- [9] E. Jónsson, E. Hermansson, M. Juliusson, L. Leifsson, and S. Koziel, “Computational fluid dynamic analysis and shape optimization of trawl-doors,” in *51st AIAA Aerospace Sciences Meeting including the New Horizons Forum and Aerospace Exposition*, 2013.

- [10] L. Leifsson, E. Hermansson, and S. Koziel, “Optimal shape design of multi-element trawl-doors using local surrogate models,” *Journal of Computational Science*, vol. 10, pp. 55–62, 2015.
- [11] N. Queipo, R. Haftka, W. Shyy, T. Goel, R. Vaidynathan, and P. Tucker, “Surrogate-based analysis and optimization,” *Progress in Aerospace Sciences*, vol. 41, pp. 1 – 28, 2006.
- [12] J. Forrester and A. Keane, “Recent advances in surrogate-based optimization,” *Progress in Aerospace Sciences*, vol. 45, pp. 50–79, 2009.
- [13] S. Koziel, “Reliable design optimization of microwave structures using multipoint-response-correction space mapping and trust regions,” *International Journal of RF and Microwave Computer-Aided Engineering*, vol. 21, pp. 534–542, 2011.
- [14] S. Koziel, L. Leifsson, and S. Ogurtsov, *Surrogate-Based Modeling and Optimization. Applications in Engineering*, S. Koziel and L. Leifsson, Eds. Springer, 2013.
- [15] E. Jonsson, “Aerodynamic optimization by variable-resolution modeling and space mapping,” Master’s thesis, School of Science and Engineering, Reykjavik University, 2012.
- [16] E. Hermansson, “Hydrodynamic shape optimization of trawl doors with three-dimensional computational fluid dynamic models and local surrogates,” Master’s thesis, KTH Royal Institute of Technology, 2014.
- [17] J. D. Anderson, *Fundamentals of Aerodynamics*, 5th ed. McGraw-Hill, 2011.
- [18] *ANSYS FLUENT Theory Guide, Release 14.0*, ANSYS Inc., Southpointe, 275 Technology Drive, Canonsburg, PA 15317, November 2011.
- [19] J. Tannehill and D. Anderson, *Computational Fluid Mechanics and Heat Transfer*, 2, Ed. Taylor & Francis, 1997.
- [20] FLUENT, ver. 14.0, ANSYS Inc., Southpointe, 275 Technology Drive, Canonsburg, PA 15317.
- [21] ANSYS ICEM CFD Help Manual, ANSYS Inc, Southpointe, 275 Technology Drive, Canonsburg, October 2012.
- [22] D. Mavriplis, “Unstructured grid techniques,” *Fluid Mechanics*, vol. 29, pp. 473–514, 1997.

- [23] I. Celik, U. Ghia, P. Roache, C. Freitas, H. Coleman, and P. Raad, “Procedure for estimation and reporting of uncertainty due to discretization in cfd applications,” *ASME Journal of Fluids Engineering*, vol. 130, 2008.
- [24] F. Stern, R. Wilson, H. Coleman, and E. Paterson, “Verification and validation of cfd simulations,” Iowa Institute of Hydraulic Research, Tech. Rep., 1999.
- [25] G. Lombardi, M. Salvetti, and D. Pinelli, “Numerical evaluation of airfoil friction drag,” *Journal of Aircraft*, vol. 37, pp. 354 – 356, 2000.
- [26] F. M. White, *Fluid Mechanics*, 7th ed., J. P. Holman and J. Lloyd, Eds. McGraw-Hill, 2011.
- [27] E. Omar, T. Zierten, M. Hahn, E. Szpizo, and A. Mahal, “Two-dimensional wind-tunnel tests of a nasa supercritical airfoil with various high-lift systems. volume 2: Test data,” NASA, Tech. Rep., 1973.
- [28] S. Koziel and S. Szczepanski, “Accurate modeling of microwave structures using shape-preserving response prediction,” *IET Microwaves, Antennas & Propagation*, vol. 5, pp. 1116–1122, 2011.
- [29] A. Giunta, S. Wojtkiewicz, and M. Eldred, “Overview of modern design of experiments methods for computational simulations,” *American Institute of Aeronautics and Astronautics*, 2003.
- [30] T. Santner, B. Williams, and W. Notz, *The Design and Analysis of Computer Experiments*. Springer, 2003.
- [31] R. Koehler and B. Owen, *Computer experiments, Handbook of Statistics*, S. Ghosh and C. Rao, Eds. Elsevier, 1996.
- [32] M. McKay, W. Conover, and R. Beckman, “A comparison of three methods for selecting values of input variables in the analysis of output from a computer code,” *Technometrics*, vol. 21, pp. 239–245, 1979.
- [33] A. Journal and C. Huijbregts, “Neural network inverse modeling and applications to microwave filter design,” *IEEE Transactions on Microwave Theory and Techniques*, vol. 56, pp. 867–879, 1981.
- [34] T. Simpson, T. Maurey, J. Korte, and F. Mistree, “Kriging models for global approximation in simulation-based multidisciplinary design optimization,” *AIAA Journal*, vol. 39, pp. 2233–2241, 2001.

- [35] J. Kleijnen, “Kriging metamodeling in simulation: a review.” *European Journal of Operational Research*, vol. 192, pp. 707–716, 2009.
- [36] C. Rasmussen and C. Williams, *Gaussian Processes for Machine Learning*. The MIT Press, 2005.
- [37] L. Leifsson and S. Koziel, “Variable-resolution shape optimization: low-fidelity model selection and scalability,” *Int. J. of Mathematical Modelling and Numerical Optimisation*, vol. 6, pp. 1–21, 2015.
- [38] S. Koziel and L. Leifsson, “Knowledge-based airfoil shape optimization using space mapping,” in *30th AIAA Applied Aerodynamics Conference*, 2012.
- [39] L. Leifsson, M. Juliusson, E. Hermannsson, and S. Koziel, “Optimal shape design of multi-element trawl-doors using local surrogate models,” *Journal of Computational Science*, 2013.

Appendices

Appendix A

Initial Optimization Results Using Multi-Point Space Mapping

In this section initial optimization results are presented, where evolution of the pattern search optimization process is shown and a comparisons between the initial and optimized trawl-door design is evaluated. For the initial optimization run all trawl-door shapes with main element and trailing-edge flap or leading-edge slat are considered.

A.1 Main Element With Trailing Edge Flap

In case of the trawl-door with a main element and trailing edge flap, the high-fidelity model were selected with about 400,000 elements (grid 9). The flow solver convergence criteria were set to 5,000 iterations, or when residuals had dropped by five orders of magnitude. The low-fidelity model were the same as the high-fidelity one, but with coarser mesh discretization and relaxed convergence criteria. The selected grid had about 25,000 elements (grid 4) and the model were considered converged after 1,000 iterations, or when residuals had dropped by three orders of magnitude. The low fidelity model resulted in being around 52 times faster than the high-fidelity one.

The objective is to maximize the lift over drag ratio L/D . The design variables are x_{flap}/c and y_{flap}/c locations of the leading edge of the flap with respect to the main element leading edge, rotation of the flap θ with respect to the main-element chord line and the angle attack α . The search domain were set as: $0.90 \leq x_{flap}/c \leq 1.20$, $-0.20 \leq y_{flap}/c \leq 0.0$,

Table A.1: Comparison of initial and optimized results of a trawl-door with a main element and trailing edge flap. The objective is to maximize C_l/C_d with no additional constraints using multi-point space mapping

	Initial	Optimized	Relative difference
x/c_{flap}	1.20	1.00	-
y/c_{flap}	-0.200	-0.0222	-
θ	30.0	17.3	-
α	5.00	5.89	-
C_l	1.30	2.04	36.3%
C_d	0.0180	0.0223	18.8%
C_l/C_d	72.5	91.6	20.9%
Iterations	-	13	-
Evaluations HF/LF	-	13/256	-
Runtime gain ratio	-	≈ 52	-
Total runtime [hours]	-	≈ 39	-

$0.0 \leq \theta_{flap} \leq 30.0$ deg, $0.00 \leq \alpha \leq 15.0$ deg. The initial design were $x_{flap}/c = 1.20$, $y_{flap}/c = -0.20$, $\theta_{flap} = 10.0$ deg and $\alpha = 5.0$ deg. It is known that the initial design is infeasible, the trailing edge flap is placed far behind and under the main element to see how efficiently the algorithm approaches more feasible design. Trust region algorithm were not active during these initial runs.

The initial and optimized results are shown in table A.1 and corresponding trawl-door shapes are shown in figure A.1. The optimized design has $x_{flap}/c = 1.00$, $y_{flap}/c = -0.0222$, $\theta_{flap} = 17.3$ and $\alpha = 5.89$ with $C_l = 2.04$ and $C_d = 0.0222$ giving a lift-to-drag ratio of 91.6. Compared to the initial design that has $C_l = 1.30$ and $C_d = 0.0180$ giving a lift-to-drag ratio of 72.5, the lift coefficient has increased about 36.3% and the drag coefficient increased about 18.8% resulting in an increase of 20.9% of the lift-to-drag ratio. The optimization algorithm required 13 high-fidelity model evaluations and 256 low fidelity ones in a runtime of approximately 39 hours.

Figure A.2 shows convergence history of the optimization process. Initially the design is infeasible and the optimizer quickly approaches more feasible design on the first six iterations. After that oscillations can be observed in the objective function as the model is iterated, and finally converges on the objective value change on a C_l/C_d value slightly under the highest one obtained in the iteration process.

The flow physics behind the hydrodynamic performance increase is seen on figure A.3 that shows velocity contour plots of both the initial and optimized design, and figure A.4 that shows pressure coefficient distribution C_p over the trawl-door surface. The stagnation

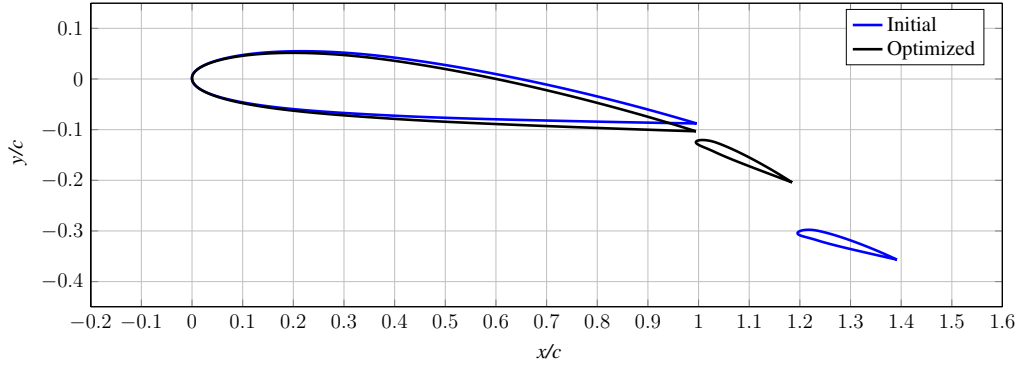
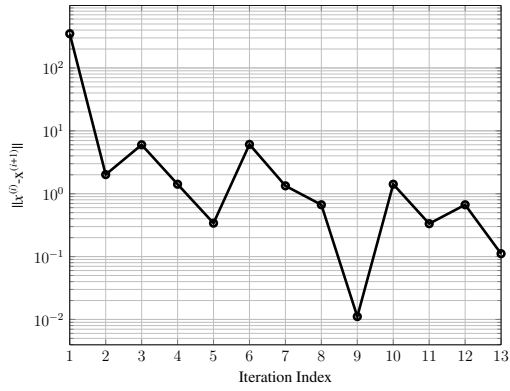
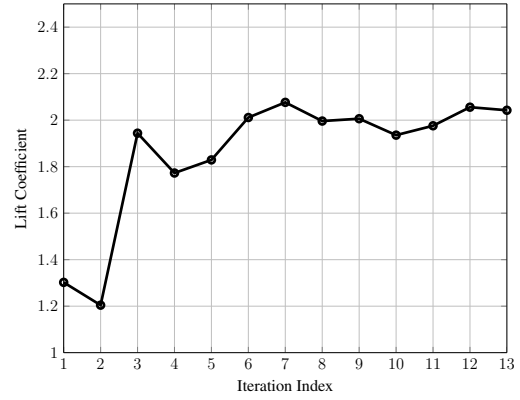


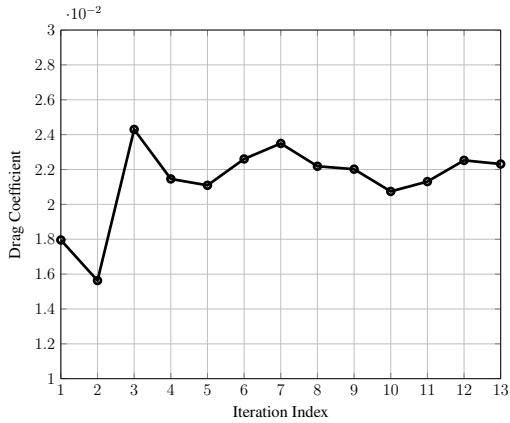
Figure A.1: Comparison of initial and optimized trawl-door shape of a trawl-door with main element and leading edge slat. The objective is to maximize C_l/C_d with no additional constraints, using multi-point space mapping. The flow is parallel to the x/c axis



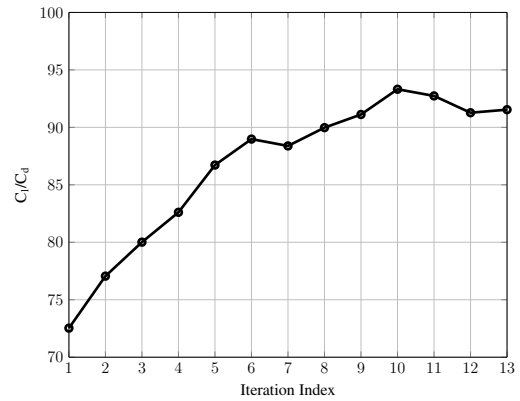
(a) Argument convergence



(b) Evolution of the lift coefficient



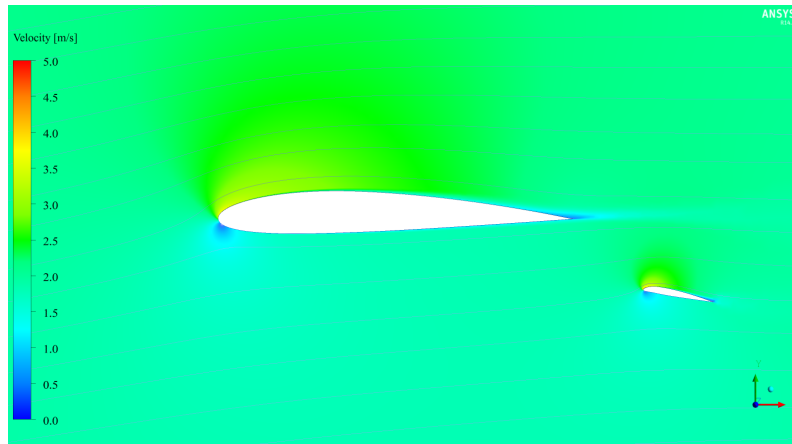
(c) Evolution of the drag coefficient



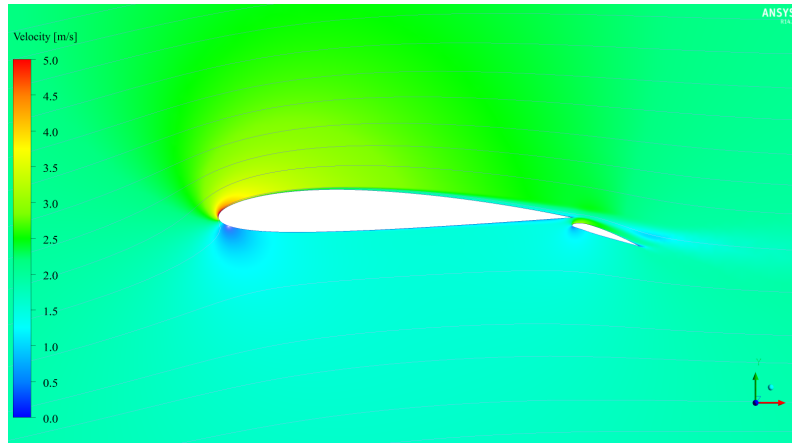
(d) Evolution of lift over drag

Figure A.2: Lift-to-Drag optimization history of a trawl-door with main element and trailing-edge flap. The objective is to maximize C_l/C_d with no additional constraints, using multi-point space mapping.

point has shifted slightly to the right, under the element resulting in velocity increase at the leading edge of the upper surface of the airfoil as the flow accelerates over the leading



(a) Initial



(b) Optimized

Figure A.3: Velocity contour comparison between the initial and optimized design of a trawl-door shape with main element and a trailing edge flap

edge that causes a pressure decrease on the top surface. Effects of the flap can be seen on the pressure distribution on the main element trailing edge where the C_p curves have shifted to both higher negative and positive values, .

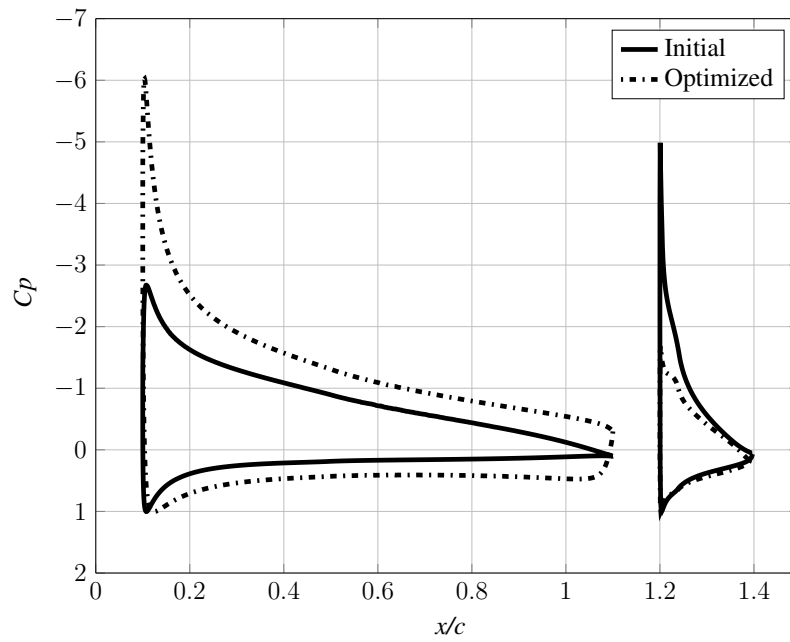


Figure A.4: Pressure distribution comparison between initial and optimized shapes of a trawl-door with main element and trailing edge flap. The objective is to maximize C_l/C_d with no additional constraints, using multi-point space mapping.

A.2 Main Element With Trailing Edge Flap Using Multi-step Approach

Because of convergence oscillations in the results above, a multi-step optimization approach were carried out. The purpose were both to find out if the optimization process would be smoother using fewer design variables in the beginning of the process, and if it would have an effect later in the process if some of the design variables were all ready close to optimum design. The sett up were the same as before, except that the optimization process were carried out in following three steps.

1. **Step 1:** Design variables for the first optimization step are x_{flap}/c and y_{flap}/c locations of the leading edge of the flap with respect to the main element leading edge. The search domain were set as $0.90 \leq x_{flap}/c \leq 1.20$ and $-0.20 \leq y_{flap}/c$ and the initial design were $x_{flap}/c = 1.20$, $y_{flap}/c = -0.20$, $\theta_{flap} = 10.0$ deg and $\alpha = 5.0$ deg where θ_{flap} and α were held constant.
2. **Step 2:** In the second optimization step the design variables are x_{flap}/c , y_{flap}/c and rotation of the flap θ with respect to the main-element chord line. The search domain were set as $0.90 \leq x_{flap}/c \leq 1.20$, $-0.20 \leq y_{flap}/c \leq 0.0$ and $0.0 \leq \theta_{flap} \leq 30.0$. The initial design for x_{flap}/c and y_{flap}/c were based on results obtained in step 1, θ_{flap} were set to 10.0 and the angle of attack were constant as $\alpha = 5.0$ deg.
3. **Step 3:** In the third step the design variables are x_{flap}/c , y_{flap}/c , θ and the angle attack α . The search domain were set as: $0.90 \leq x_{flap}/c \leq 1.20$, $-0.20 \leq y_{flap}/c \leq 0.0$, $0.0 \leq \theta_{flap} \leq 30.0$ deg, $0.00 \leq \alpha \leq 15.0$ deg. The initial design for x_{flap}/c , y_{flap}/c and θ were based on results obtained in step 2 and the angle of attack were set to 5.0 deg.

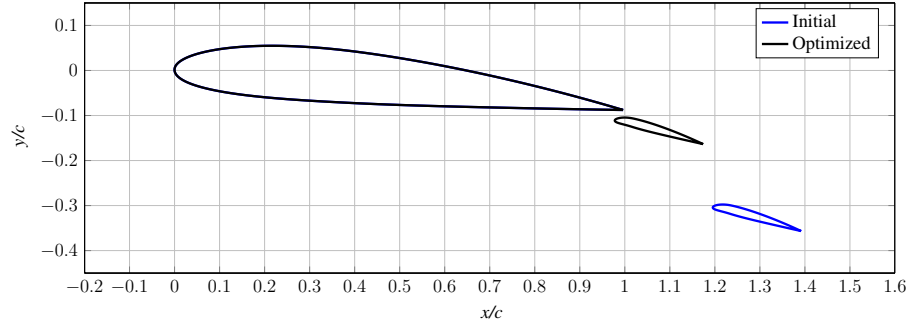
The objective is to maximize the lift-to-drag ratio with no additional constraints.

The optimization results are shown in table A.2, and the initial and optimized trawl-door shapes are shown in figure A.5. The optimized design has $x_{slat}/c = 0.981$, $y_{slat}/c = -0.0259$, $\theta_{slat} = 15.1$ deg, and $\alpha = 3.56$ deg, with $C_l = 1.65$ and $C_d = 0.0179$ giving a lift-to-drag ratio of 91.7. The SM optimizer required 3 high-fidelity model evaluations and 64 low-fidelity ones for the first step, 3 high-fidelity model evaluations and 64 low-fidelity ones for the second step and 6 high-fidelity model evaluations and 118 low-fidelity ones for the last step resulting in a total of 12 high-fidelity model evaluations and 242 low-fidelity ones. The number of high-fidelity evaluations could have been reduced by 2, if

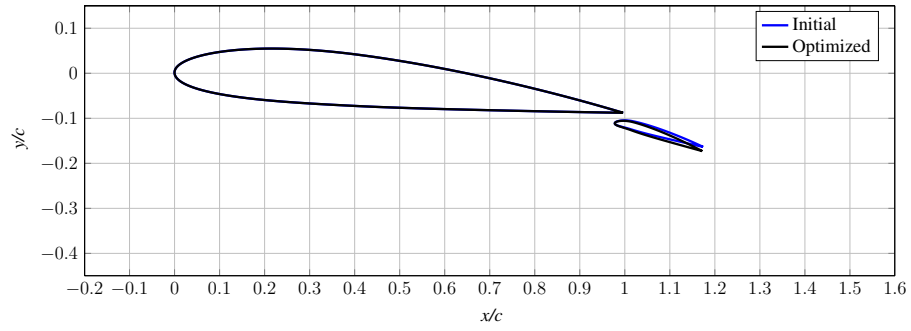
the initial evaluation of runs 2 and 3 would have had knowledge of what happened in steps 1 and 2. The overall runtime were approximately 34 hours, with a runtime gain ratio of 53.9. Figure A.15 shows convergence history of the optimization process for each step.

Table A.2: Comparison of initial and optimized results of a trawl-door with a main element and trailing edge flap. The objective is to maximize C_l/C_d with no additional constraints using multi-point space mapping with multi-step approach

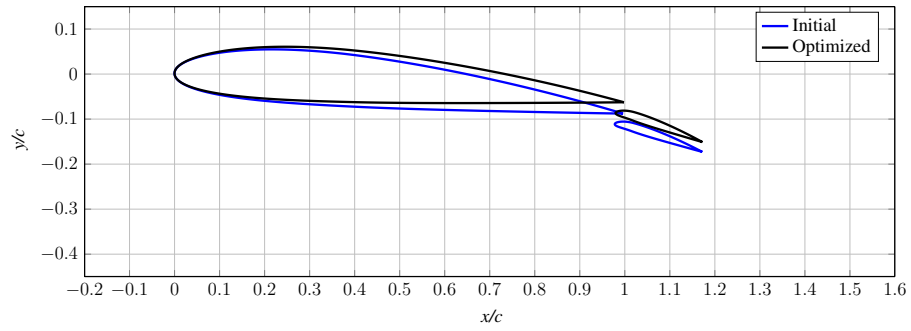
	Step 1	Step 2	Step 3	Total
\mathbf{x}	$[x \ y]^T$	$[x \ y \ \theta]^T$	$[x \ y \ \theta \ \alpha]^T$	-
$\mathbf{x}/\mathbf{c}_{\text{slat}}$	0.981	0.981	0.981	-
$\mathbf{y}/\mathbf{c}_{\text{slat}}$	-0.0259	-0.0259	-0.0259	-
θ	-10.0	-12.8	-15.1	-
α	5.00	5.00	3.56	-
C_l	1.57	1.71	1.65	-
C_d	0.0176	0.0188	0.0179	-
C_l/C_d	89.4	91.0	91.7	-
Iterations	3	3	6	12
Evaluations HF/LF	3/64	3/60	6/118	12/242
Total runtime [hours]	≈ 10.4	≈ 8.1	≈ 15.5	≈ 34.0
Runtime Gain Ratio	≈ 72	≈ 50.3	≈ 46.4	≈ 53.9



(a) Step 1

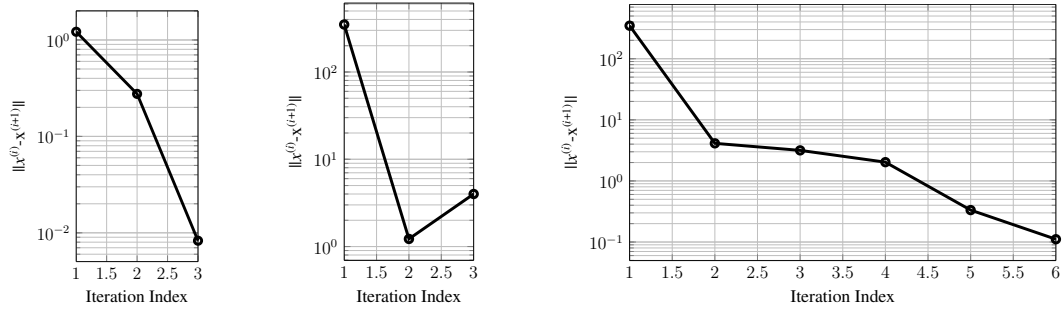


(b) Step 2

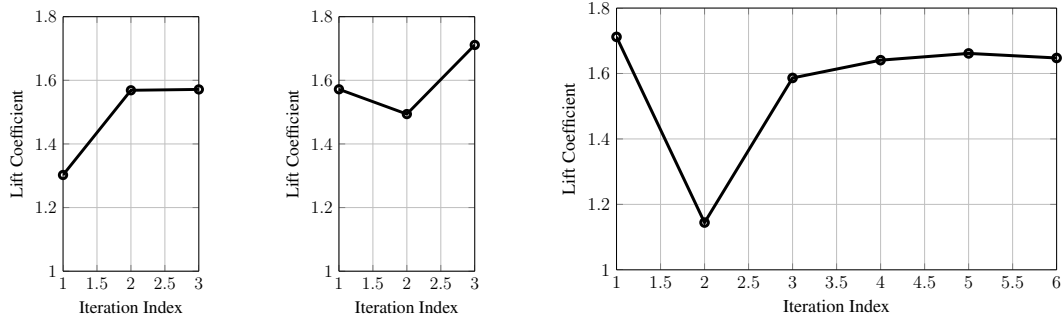


(c) Step 3

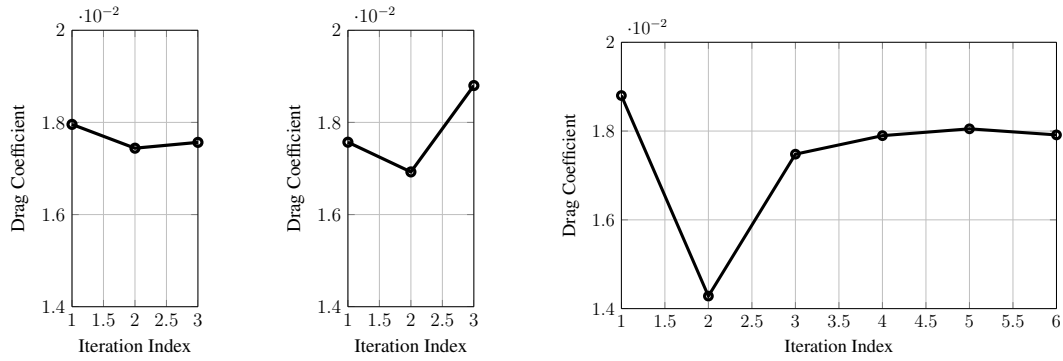
Figure A.5: Comparison of initial and optimized trawl-door shape of a trawl-door with main element and trailing edge flap. The objective is to maximize C_l/C_d with no additional constraints, using multi-point space mapping. The flow is parallel to the x/c axis



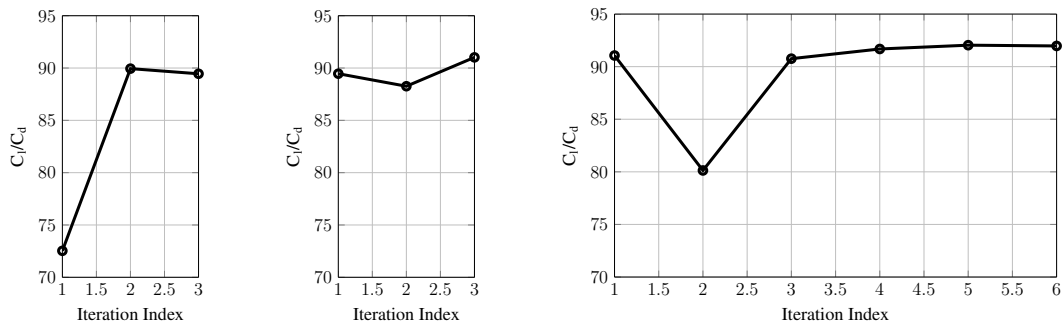
(a) Argument convergence from step 1 to 3



(b) Evolution of the lift coefficient from step 1 to 3

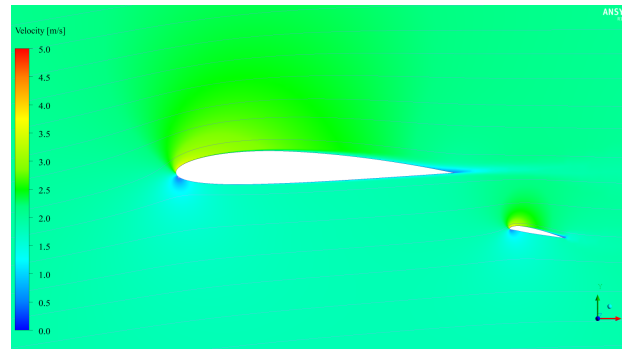


(c) Evolution of the drag coefficient from step 1 to 3

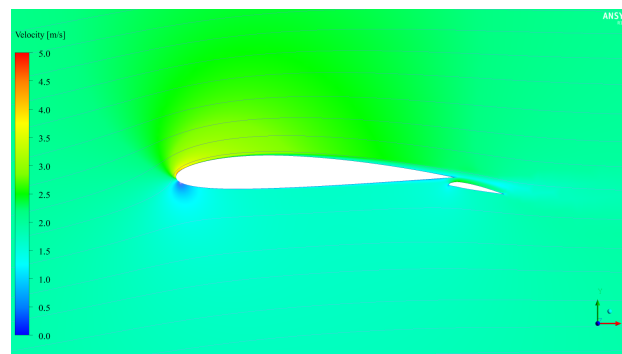


(d) Evolution of lift-to-drag from step 1 to 3

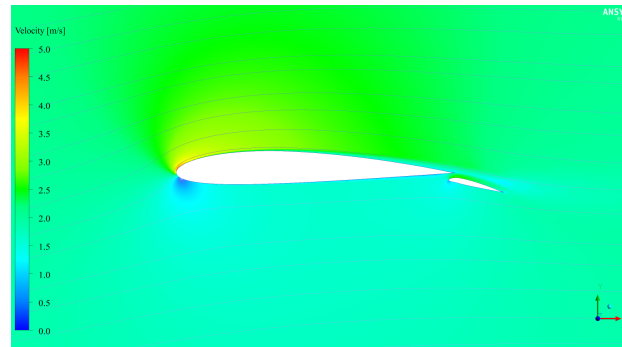
Figure A.6: Lift-to-Drag optimization history of a trawl-door with main element and leading-edge slat. The objective is to maximize C_l/C_d with no additional constraints, using multi-point space mapping.



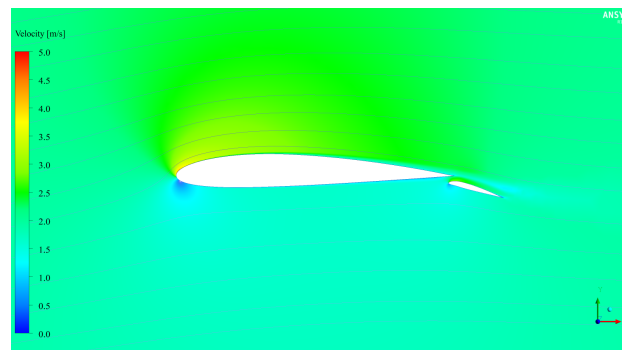
(a) Initial



(b) Optimized, step 1

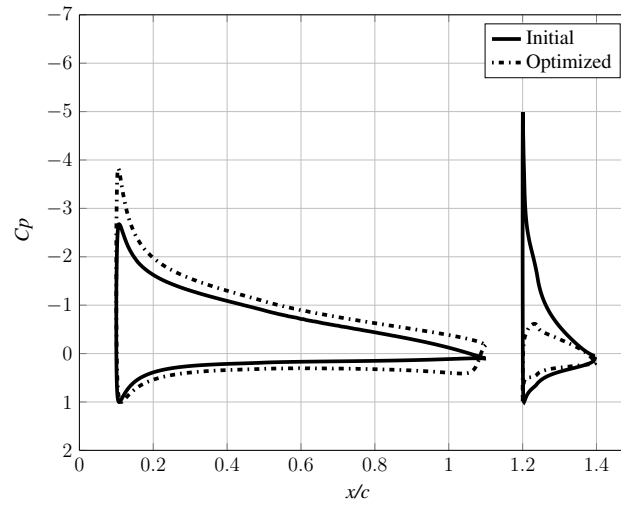


(c) Optimized, step 2

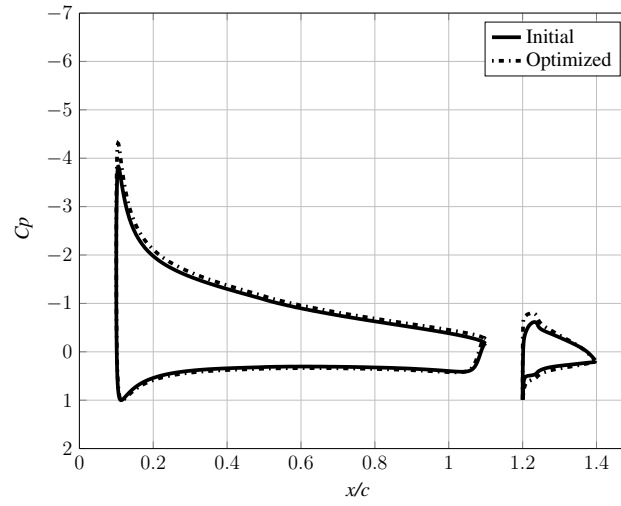


(d) Optimized, step 3

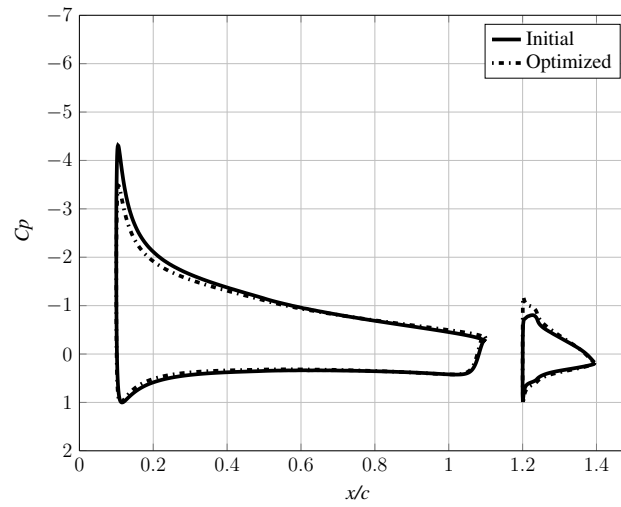
Figure A.7: Velocity contour comparison between the initial and optimized designs of each step in sequential approach.



(a) Step 1



(b) Step 2



(c) Step 3

Figure A.8: Pressure distribution comparison between initial and optimized shapes of a trawl-door with main element and trailing edge flap. The objective is to maximize C_l/C_d with no additional constraints, using multi-point space mapping.

Table A.3 shows comparison between the result obtained by the single- and multi-step approaches. The results are similar regarding location of the flap, but there is some difference in rotation of the flap and angle of attack. Still the lift-to-drag between ratio for these results is similar.

Table A.3: Optimization result comparison for trawl-door with main element and flap with both using the single- and multi-level approaches

	Initial	Optimized	Optimized Multi-step Approach
$\mathbf{x}/c_{\text{slat}}$	1.200	1.00	0.981
$\mathbf{y}/c_{\text{slat}}$	-0.200	-0.0222	-0.0259
θ	-10.0	-17.3	-15.1
α	5.00	5.89	3.56
C_l	1.5	2.04	1.65
C_d	0.0176	0.0223	0.0179
C_l/C_d	89.4	91.6	92.0
Iterations	-	13	12
Evaluations (HF/LF)	-	13/256	12/242
Total runtime [hours]	-	≈ 39.0	≈ 34.0
Runtime Gain Ratio	-	≈ 52.2	≈ 53.9

Figure A.9 show the optimizers path for the first step. Here the cyan circles represents where high-fidelity evaluations were performed in the $x_{\text{flap}}/c, y_{\text{flap}}/c$ plane while the lines represent the path. The magenta dots represent where low-fidelity evaluations were made. The optimizer moves quickly from infeasible initial location of the flap after only few low-fidelity evaluations, to a more feasible area where the model converges. The C_l/C_d contour represents the low-fidelity model.

Figure A.10 shows the performance of C_l/C_d as a function of α (the most sensitive design variable) for the initial, optimized in one step and optimized using multi-step approach trawl-door shapes with main element and flap. We can see that the performance has improved considerably from the initial shape, but still we should be able to obtain even better results. The optimization using single-step approach gives better results, but the peak on C_l/C_d curve were not located by the optimizer. The multi-step approach gives the highest C_l/C_d value and the optimizer locates the top of the curve, but still the one-step shape has more potential in obtaining higher C_l/C_d value

This behaviour is considered to be a cause of numerical noise in the low fidelity model that makes the optimizer oscillate in a noisy solution near the optimum value. It is clear that refinement of the low-fidelity model is needed.

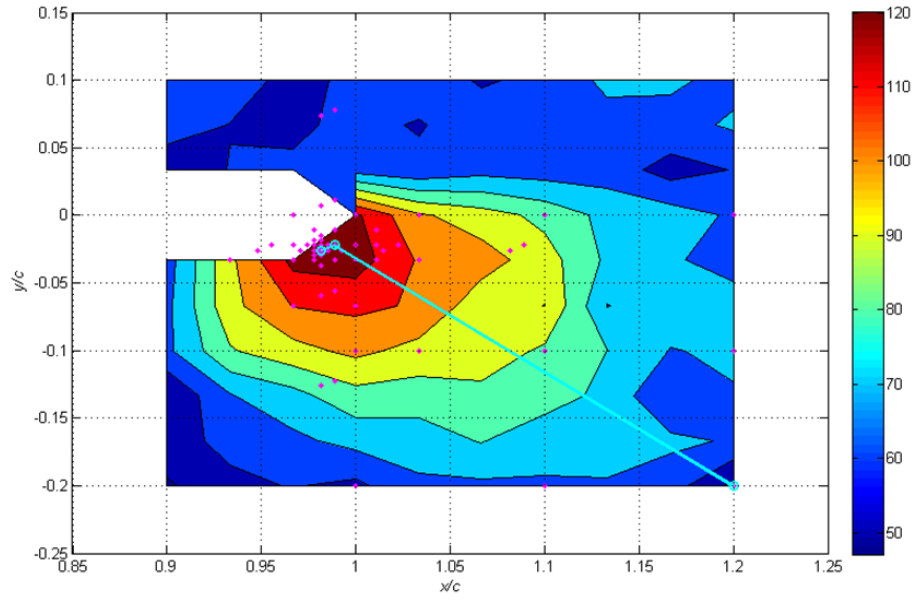
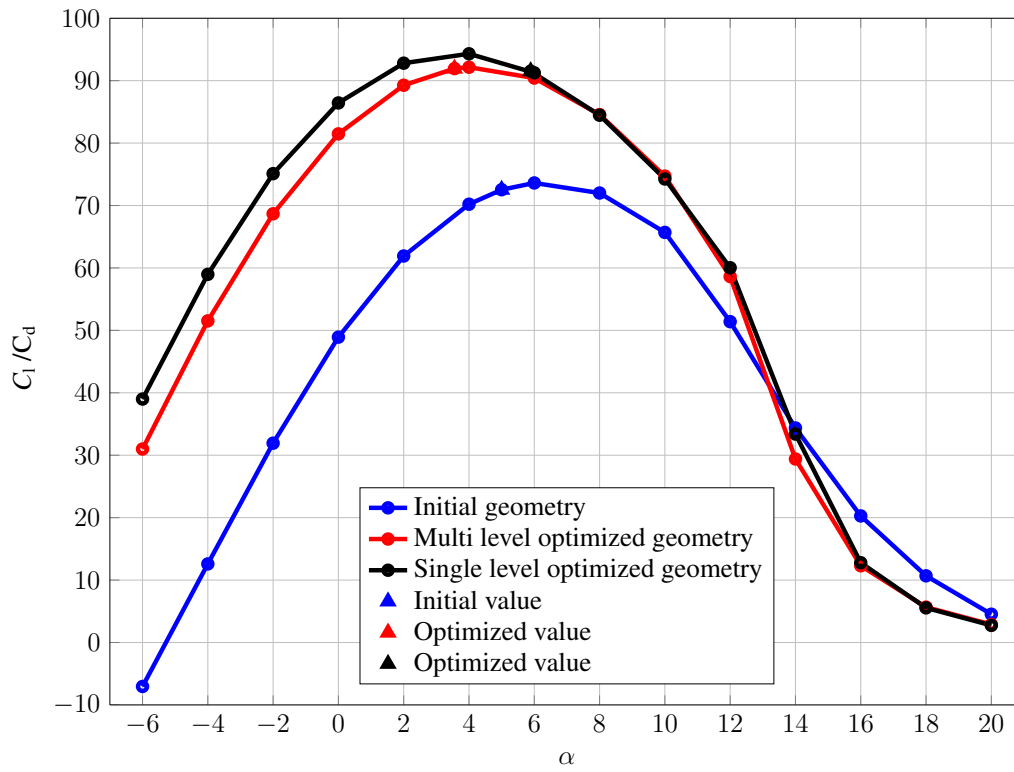


Figure A.9: Optimizers path for step 1 using multi-step approach

Figure A.10: C_l/C_d performance as a function of angle of attack for the optimized trawl-door geometries with main element and trailing edge flap

A.3 Main Element With Leading Edge Slat

Following optimization run has the same trawl-door geometry as the case before. The high-fidelity model were selected with about 517,000 elements (grid 9). The flow solver convergence criteria were set to 5,000 iterations, or when residuals had dropped by six orders of magnitude. The low-fidelity model were the same as the high-fidelity one, but with coarser mesh discretization and relaxed convergence criteria. The selected grid had about 20,000 elements and the model were considered converged after 1,000 iterations, or when residuals had dropped by 3 orders in magnitude. The low fidelity model resulted in being around 75 times faster than the high-fidelity one.

The objective is to maximize the lift over drag ratio L/D . The design variables are x_{flap}/c and y_{flap}/c locations of the leading edge of the slat with respect to the main element leading edge, rotation of the slat θ with respect to the main-element chord line and the angle at attack α . The search domain were set as: $-0.40 \leq x_{flap}/c \leq 0.20$, $-0.20 \leq y_{flap}/c \leq 0.0$, $0.0 \leq \theta_{flap} \leq 30.0$ deg, $0.00 \leq \alpha \leq 15.0$ deg. The initial design were $x_{flap}/c = -0.20$, $y_{flap}/c = -0.08$, $\theta_{flap} = 25.0$ deg and $\alpha = 5.0$ deg.

The initial and optimized results are shown in table A.4 and corresponding trawl-door shapes are shown in figure A.11. The optimized design has $x_{slat}/c = -0.20$, $y_{slat}/c = -0.0467$, $\theta_{flap} = 25.3$ and $\alpha = 9.33$ with $C_l = 1.32$ and $C_d = 0.0165$ giving a lift-to-drag ratio of 79.8. Compared to the initial design that has $C_l = 0.698$ and $C_d = 0.0188$ giving a lift-to-drag ratio of 37.1, the lift coefficient has increased about 47.1% and the drag coefficient decreased about 13.9% resulting in an increase of 53.5% of the lift-to-drag ratio. The optimization algorithm required 4 high-fidelity model evaluations and 78 low fidelity ones in a runtime of approximately 14 hours.

Table A.4: Comparison of initial and optimized results of a trawl-door with a main element and leading edge slat. The objective is to maximize C_l/C_d with no additional constraints using multi-point space mapping

	Initial	Optimized	Relative difference
$\mathbf{x}/c_{\text{slat}}$	-0.200	-0.200	-
$\mathbf{y}/c_{\text{slat}}$	-0.0800	-0.0467	-
θ	25.0	25.3	-
α	5.00	9.33	-
C_l	0.698	1.32	47.1%
C_d	0.0188	0.0165	-13.9%
C_l/C_d	37.1	79.8	53.5%
Evaluations HF/LF	-	4/78	-
Runtime gain ratio	-	≈ 75	-
Total runtime [hours]	-	≈ 14	-

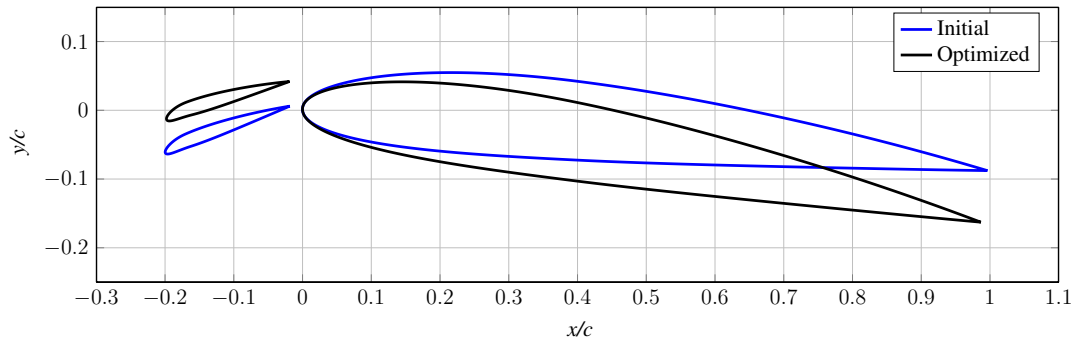
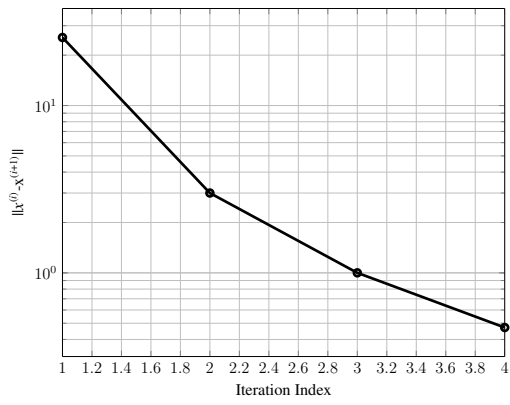
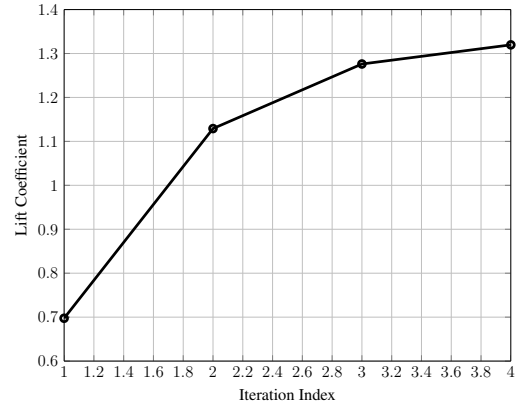


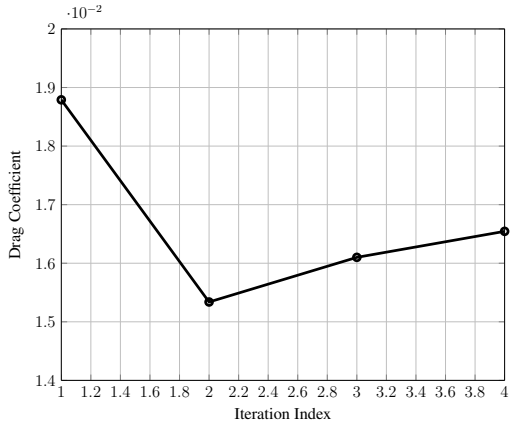
Figure A.11: Comparison of initial and optimized trawl-door shape of a trawl-door with main element with leading edge slat. The objective is to maximize C_l/C_d with no additional constraints, using multi-point space mapping. The flow is parallel to the x/c axis



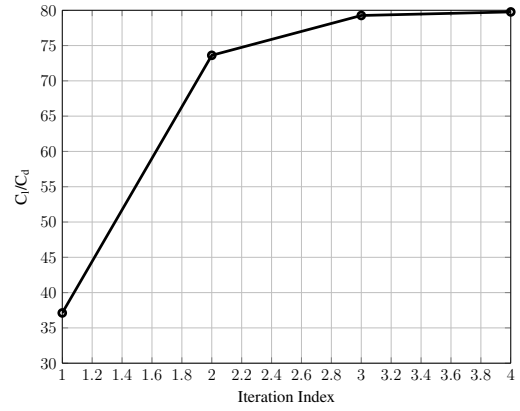
(a) Argument convergence



(b) Evolution of the lift coefficient



(c) Evolution of the drag coefficient



(d) Evolution of lift over drag

Figure A.12: Lift-to-Drag optimization history of a trawl-door with main element and leading-edge slat. The objective is to maximize C_l/C_d with no additional constraints, using multi-point space mapping.

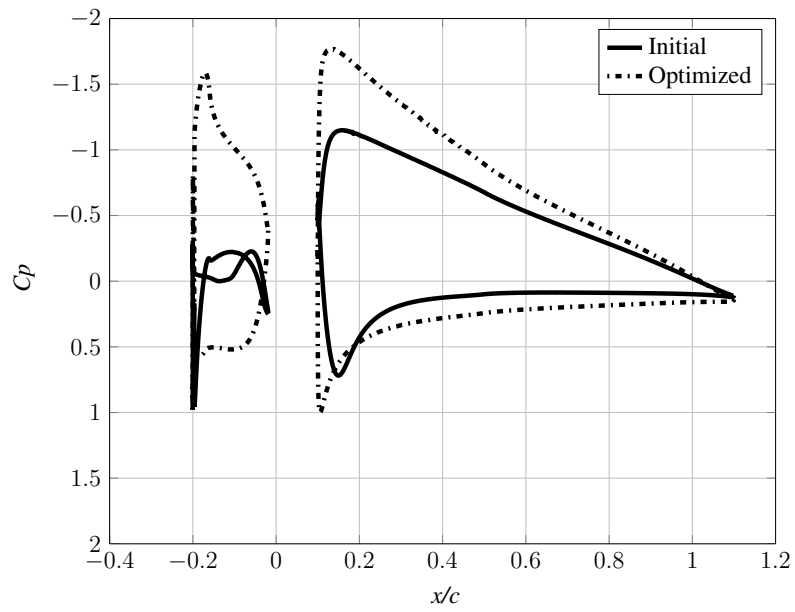


Figure A.13: Pressure distribution comparison between initial and optimized shapes of a trawl-door with main element and leading-edge slat. The objective is to maximize C_l/C_d with no additional constraints, using multi-point space mapping.

A.4 Main Element with Leading Edge Slat Using Multi-Step Approach

Because of convergence oscillations in the results above, a multi-step optimization approach were carried out. The purpose were the same is in the case of main element with leading edge flap, to both to find out if the optimization process would be smoother using fewer design variables in the beginning of the process, and if it would have an effect later in the process if some of the design variables were already close to optimum design. The sett up were the same as before, except that the optimization process were carried out in following three steps.

1. **Step 1:** Design variables for the first optimization step are x_{slat}/c and y_{slat}/c locations of the leading edge of the slat with respect to the main element leading edge. The search domain were set as $-0.40 \leq x_{slat}/c \leq 0.20$ and $-0.30 \leq y_{slat}/c \leq 0.3$ and the initial design were $x_{slat}/c = -0.20$, $y_{slat}/c = -0.08$, $\theta_{slat} = 25.0$ deg and $\alpha = 8.00$ deg where θ_{slat} and α were held constant.
2. **Step 2:** In the second optimization step the design variables are x_{slat}/c , y_{slat}/c and rotation of the slat θ with respect to the main-element chord line. The search domain were set as $-0.40 \leq x_{slat}/c \leq 0.20$ and $-0.30 \leq y_{slat}/c \leq 0.3$ and $20.0 \leq \theta_{slat} \leq 50.0$. The initial design for x_{slat}/c and y_{slat}/c were based on results obtained in step 1, θ_{slat} were set to 25.0 and the angle of attack were constant as $\alpha = 8.0$ deg.
3. **Step 3:** In the third step the design variables are x_{slat}/c , y_{slat}/c , θ and the angle attack α . The search domain were set as $-0.40 \leq x_{slat}/c \leq 0.20$ and $-0.30 \leq y_{slat}/c \leq 0.3$, $20.0 \leq \theta_{slat} \leq 50.0$ deg, $0.00 \leq \alpha \leq 20.0$ deg. The initial design for x_{slat}/c , y_{slat}/c and θ were based on results obtained in step 2 and the angle of attack were set to 8.0 deg.

The objective is to maximize the lift-to-drag ratio with no additional constraints.

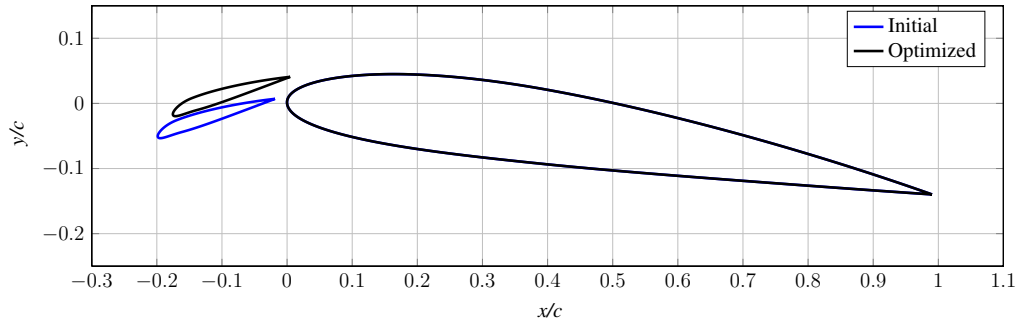
The optimization results are shown in table A.5, and the initial and optimized trawl-door shapes are shown in figure A.14. The optimized design has $x_{slat}/c = -0.180$, $y_{slat}/c = -0.0430$, $\theta_{slat} = 23.7$ deg, and $\alpha = 8.33$ deg, with $C_l = 1.21$ and $C_d = 0.0155$ giving a lift-to-drag ratio of 78.1. The SM optimizer required 3 high-fidelity model evaluations and 66 low-fidelity ones for the first step, 4 high-fidelity model evaluations and 90 low-fidelity ones for the second step and 3 high-fidelity model evaluations and 71 low-fidelity ones for the last step resulting in a total of 10 high-fidelity model evaluations and 227 low-fidelity ones. The number of high-fidelity evaluations could have been reduced by

2, if the initial evaluation of runs 2 and 3 would have had knowledge of what happened in steps 1 and 2. The overall runtime were approximately 35 hours, with a runtime gain ratio of 80. Figure A.15 shows convergence history of the optimization process for each step.

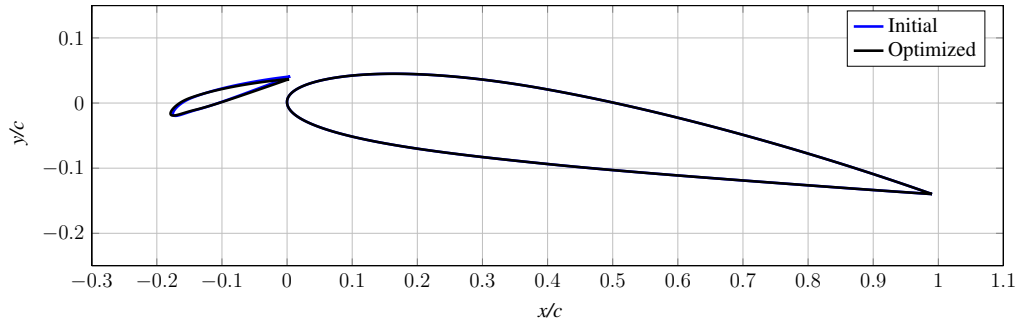
Figure A.17 shows a lift-to-drag contour plot obtained by the low-fidelity model representing solution change as a function of x_{slat}/c and y_{slat}/c for the same trawl-door shape as optimized in run 1. It is emphasized that the low-fidelity model is a cheap representation of the high-fidelity one. According to the plot a feasible area is in vicinity of $x_{slat}/c \approx -0.18$ and $y_{slat}/c \approx -0.04$, Compared to $x_{slat}/c = -0.177$ and $y_{slat}/c = -0.0430$ found by the optimizer.

Table A.5: Comparison of initial and optimized results of a trawl-door with a main element and leading edge slat. The objective is to maximize C_l/C_d with no additional constraints using multi-point space mapping

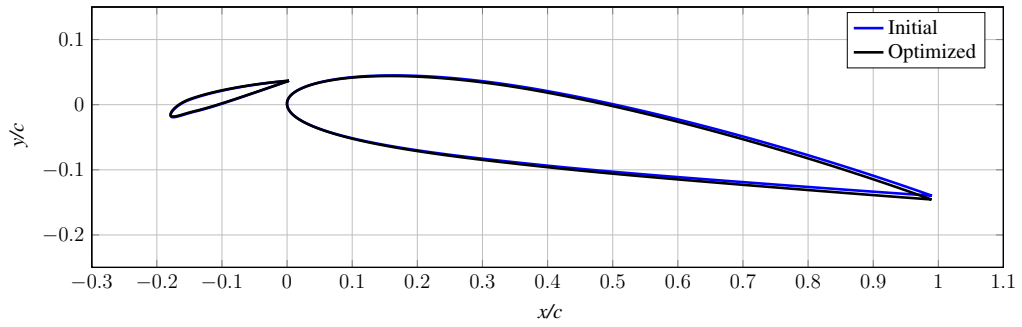
	Step 1	Step 2	Step 3	Total
\mathbf{x}	$[x \ y]^T$	$[x \ y \ \theta]^T$	$[x \ y \ \theta \ \alpha]^T$	-
\mathbf{x}/c_{slat}	-0.177	-0.180	-0.180	-
\mathbf{y}/c_{slat}	-0.0430	-0.0430	-0.0430	-
θ	25.0	23.7	23.7	-
α	8.00	8.00	8.33	-
C_l	1.16	1.17	1.21	-
C_d	0.0153	0.0152	0.0155	-
C_l/C_d	76.1	77.1	78.1	-
Iterations	3	4	3	10
Evaluations HF/LF	3/66	4/90	3/71	10/227
Total runtime [hours]	≈ 10.4	≈ 14.2	≈ 10.4	≈ 35
Runtime Gain Ratio	≈ 85.9	≈ 83.3	≈ 85.7	≈ 80



(a) Step 1

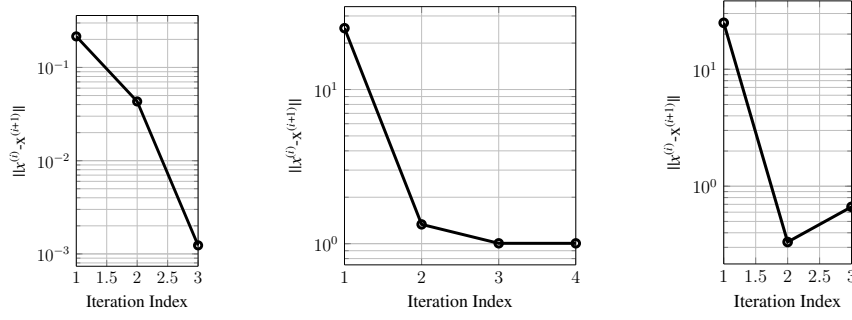


(b) Step 2

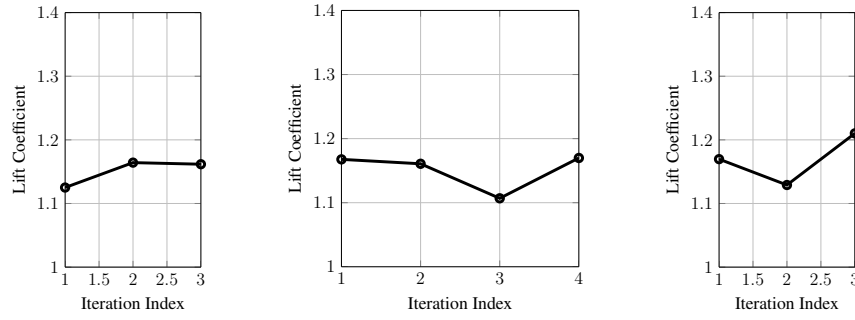


(c) Step 3

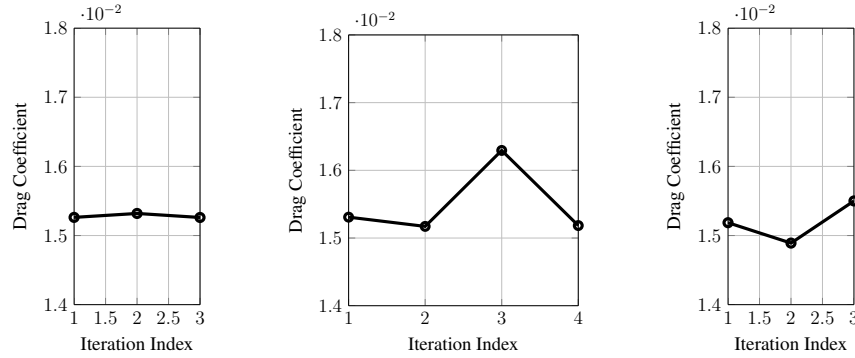
Figure A.14: Comparison of initial and optimized trawl-door shape of a trawl-door with main element and leading edge slat. The objective is to maximize C_l/C_d with no additional constraints, using multi-point space mapping. The flow is parallel to the x/c axis



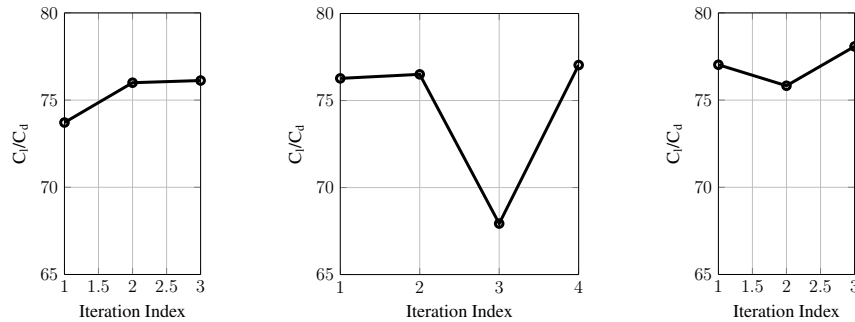
(a) Argument convergence from step 1 to 3



(b) Evolution of the lift coefficient from step 1 to 3

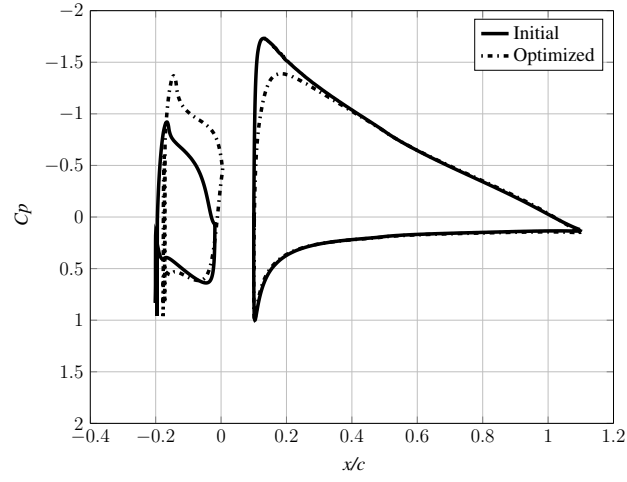


(c) Evolution of the drag coefficient from step 1 to 3

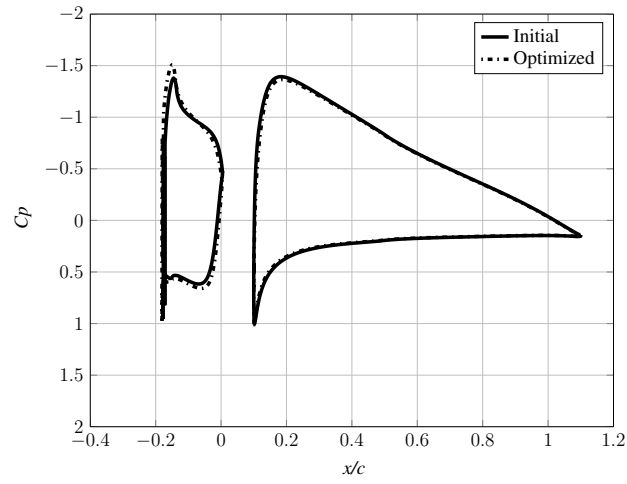


(d) Evolution of lift-to-drag from step 1 to 3

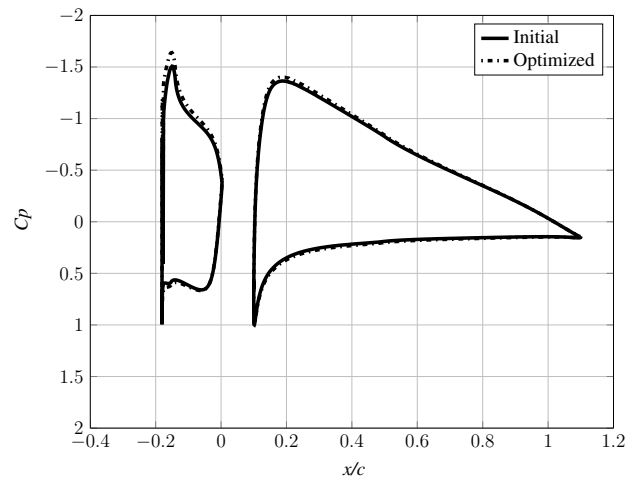
Figure A.15: Lift-to-Drag optimization history of a trawl-door with main element and leading-edge slat. The objective is to maximize C_l/C_d with no additional constraints, using multi-point space mapping.



(a) Step 1



(b) Step 2



(c) Step 3

Figure A.16: Pressure distribution comparison between initial and optimized shapes of a trawl-door with main element and leading-edge slat. The objective is to maximize C_l/C_d with no additional constraints, using multi-point space mapping.

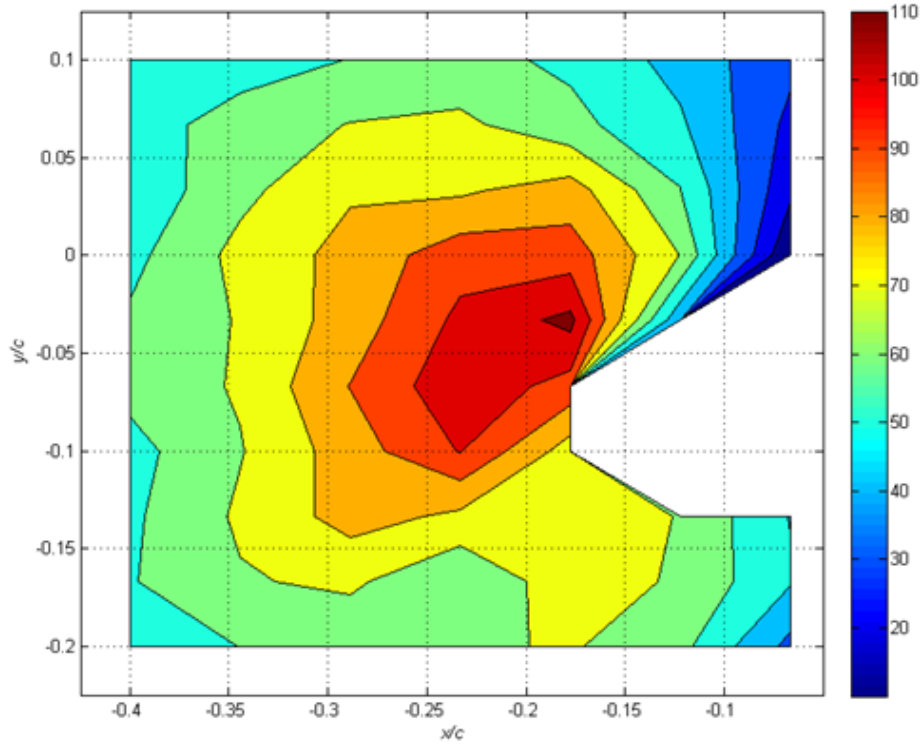


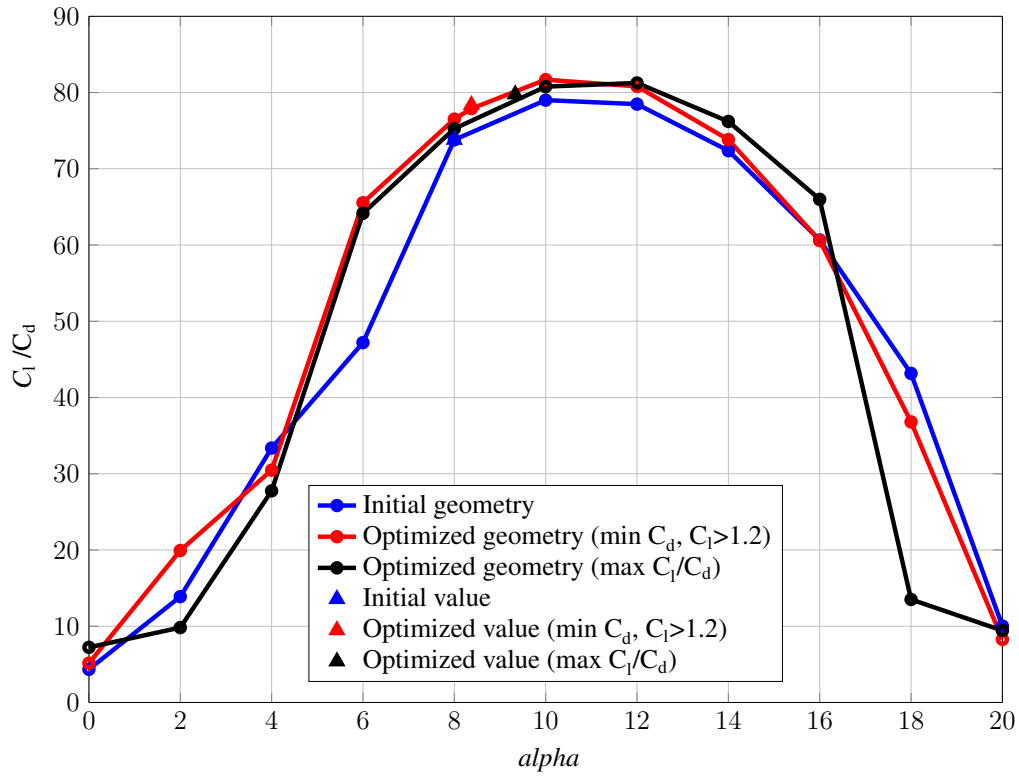
Figure A.17: Lift-to-drag contour plot obtained by the low fidelity model

Table A.6 shows comparison between the result obtained by the single- and multi-step approaches. The results are similar regarding location of the slat in y_{slat}/c , but there are some difference in x_{slat}/c direction, rotation of the slat and angle of attack. Still the lift-to-drag between ratio for these results is similar, but the single-step approach obtains higher lift-to-drag ratio that is in contrast with a trawl-door with main element and trailing edge flap. There is also large difference in computational time where the multi-step approach is more than two times longer to compute than the single-step one.

Figure A.18 shows the performance of C_l/C_d as a function of α for the initial shape, optimized shape for drag minimization subjected to constraints on lift and optimized shape where the objective is to maximize C_l/C_d . The performance has improved considerably from the initial shape, but still we should be able to obtain even better results. Again the optimizer fails to identify the true maximum at the top of the lift-to-drag curve, even further confirming that the noise in the low-fidelity model is unacceptable.

Table A.6: Optimization result comparison for trawl-door with main element and slat between the single- and multi-level approaches

	Initial	Optimized	Optimized Multi-step Approach
x/c_{slat}	-0.20	-0.20	-0.180
y/c_{slat}	-0.080	-0.0467	-0.0430
θ	25.0	25.3	23.7
α	5.00	9.33	8.33
C_l	0.698	1.32	1.21
C_d	0.0188	0.0165	0.0155
C_l/C_d	37.1	79.8	78.1
Iterations	-	4	10
Evaluations (HF/LF)	-	4/78	10/227
Total runtime [hours]	-	≈ 14	≈ 35
Runtime Gain Ratio	-	≈ 75	≈ 80

Figure A.18: C_l/C_d performance as a function of angle of attack for the optimized trawl-door geometries with main element and leading edge slat

Appendix B

Grid Convergence Studies

Grid convergence study results shown here are in accordance with methods described in chapter 3.4.

B.1 Main Element and Trailing Edge Flap

Table B.1 Shows location of design variables during the study.

Table B.1: Location of flap during grid convergence study

Location	
x/c_{flap}	1.02
y/c_{flap}	-0.0200
θ	-10.0
α	8.00

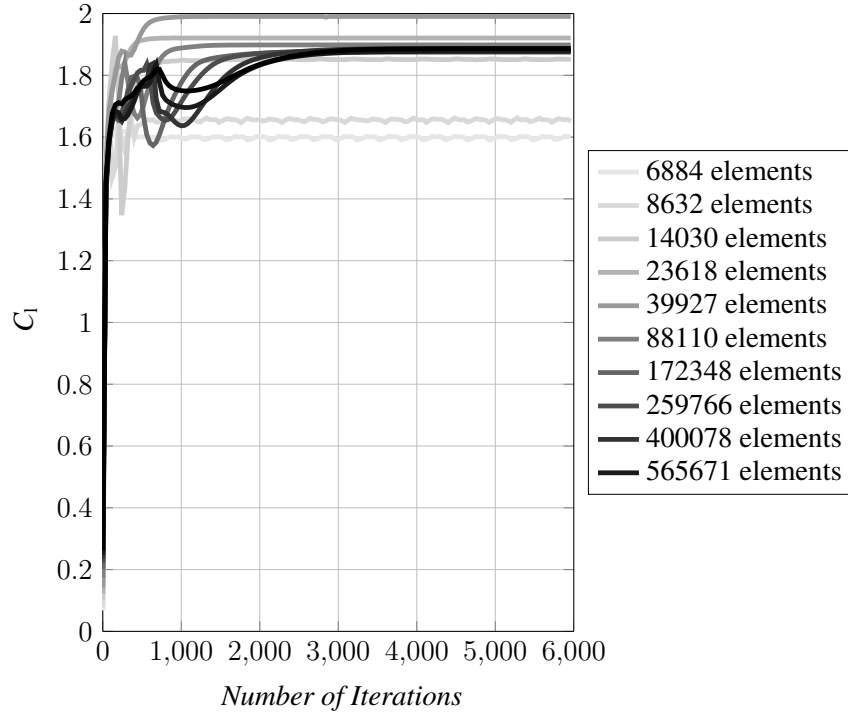


Figure B.1: Convergence of lift coefficient C_l for ten grids with variable density

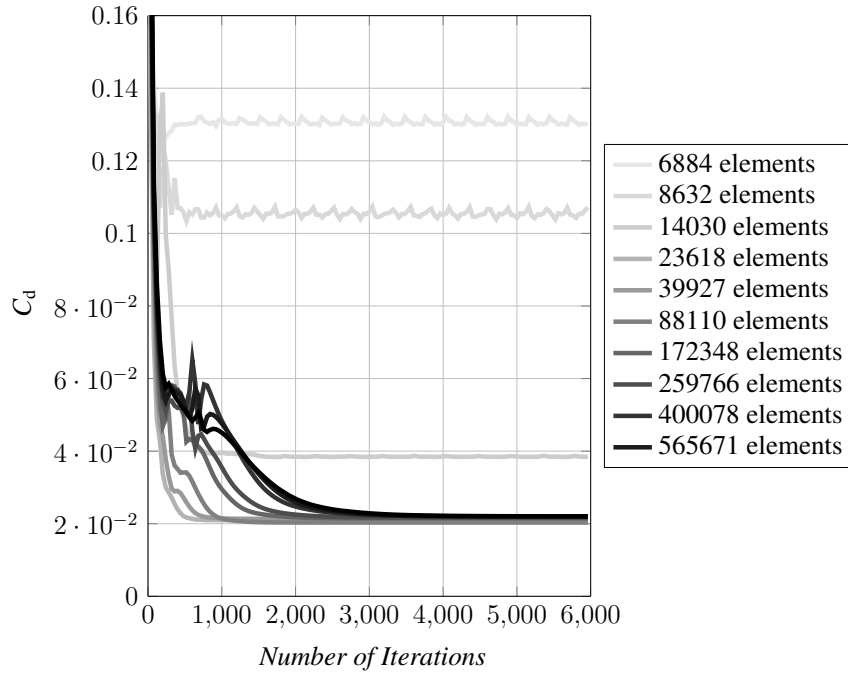


Figure B.2: Convergence of lift coefficient C_d for ten grids with variable density

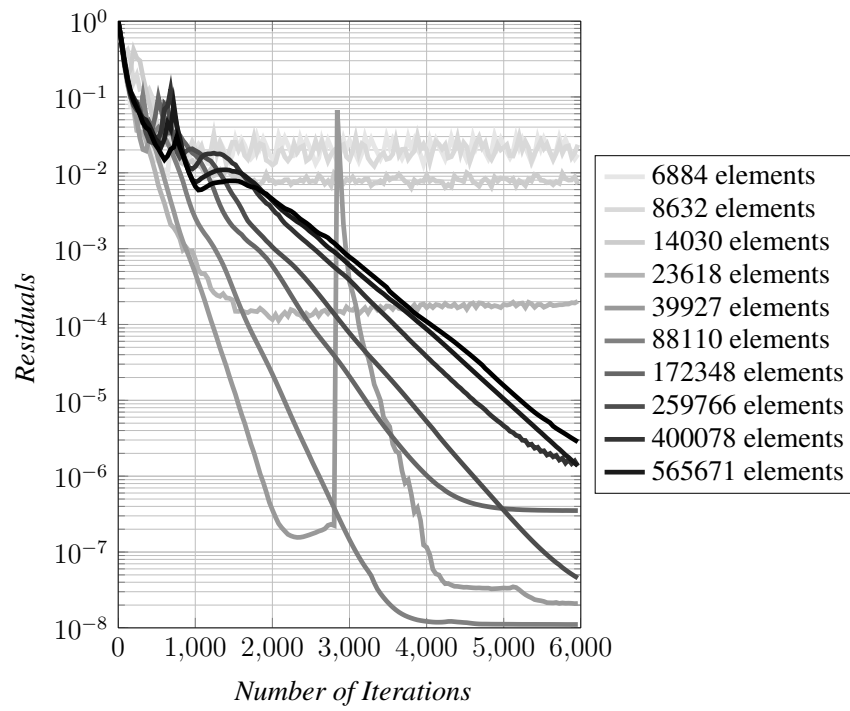


Figure B.3: Solution residuals for ten grids used in the grid convergence study

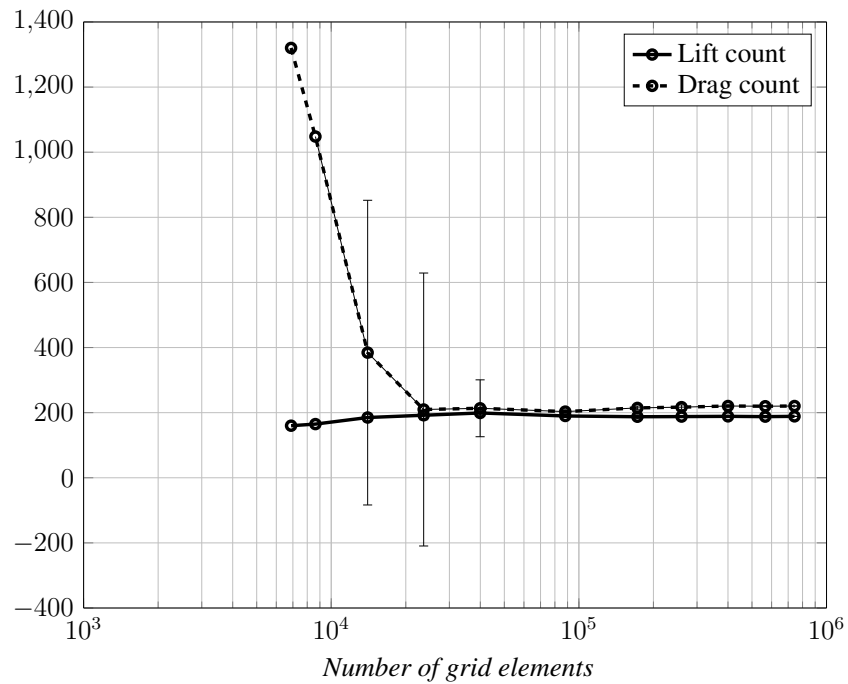


Figure B.4: Grid convergence study for a trawl-door with uncertainty estimation

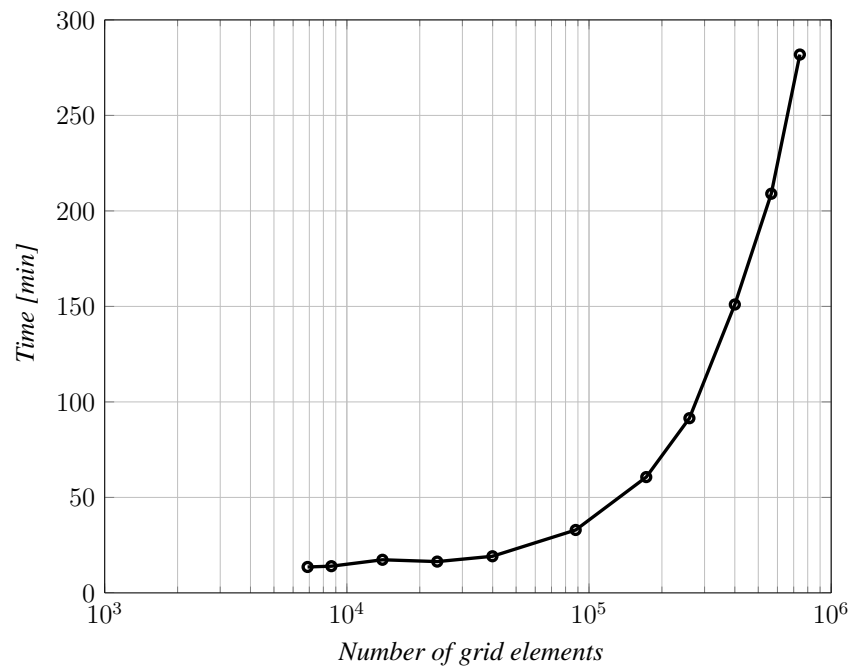


Figure B.5: Computational time as a function of grid density

B.2 Main Element With Leading Edge Slat and Trailing Edge Flap

Table B.2 Shows location of design variables during the study.

Table B.2: Location of slat and flap during grid convergence study

Location	
x/c_{slat}	-0.200
y/c_{slat}	-0.0800
θ_{slat}	25.0
x/c_{flap}	1.01
y/c_{flap}	-0.02
θ	-10.0
α	5.00

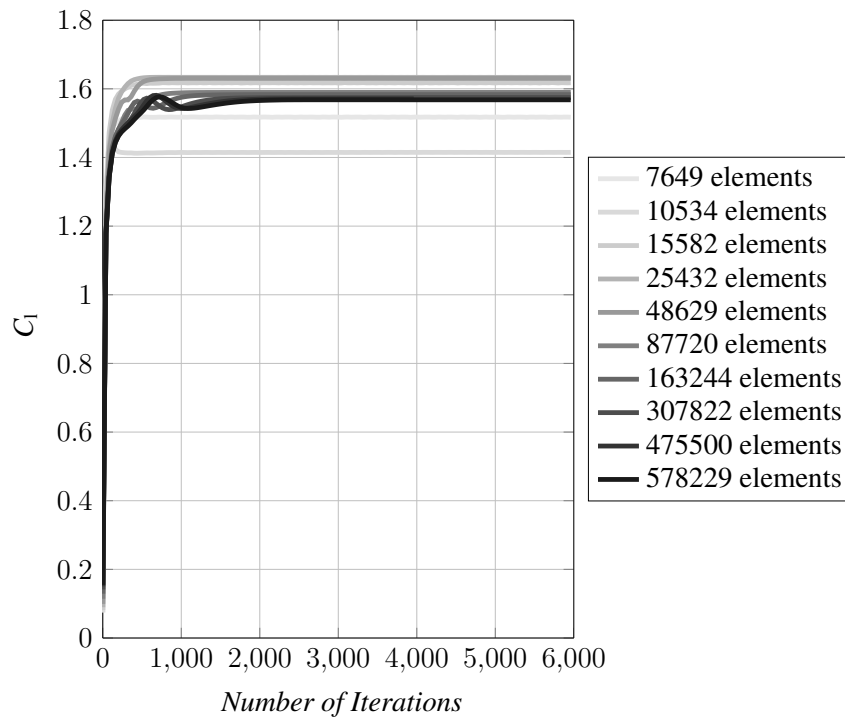


Figure B.6: Convergence of lift coefficient C_l for ten grids with variable density

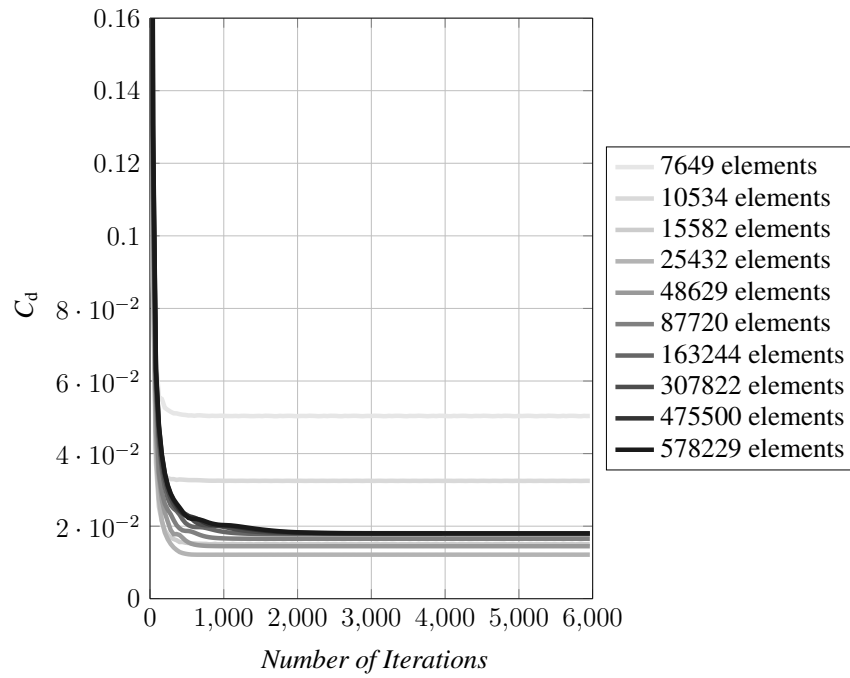


Figure B.7: Convergence of lift coefficient C_d for ten grids with variable density

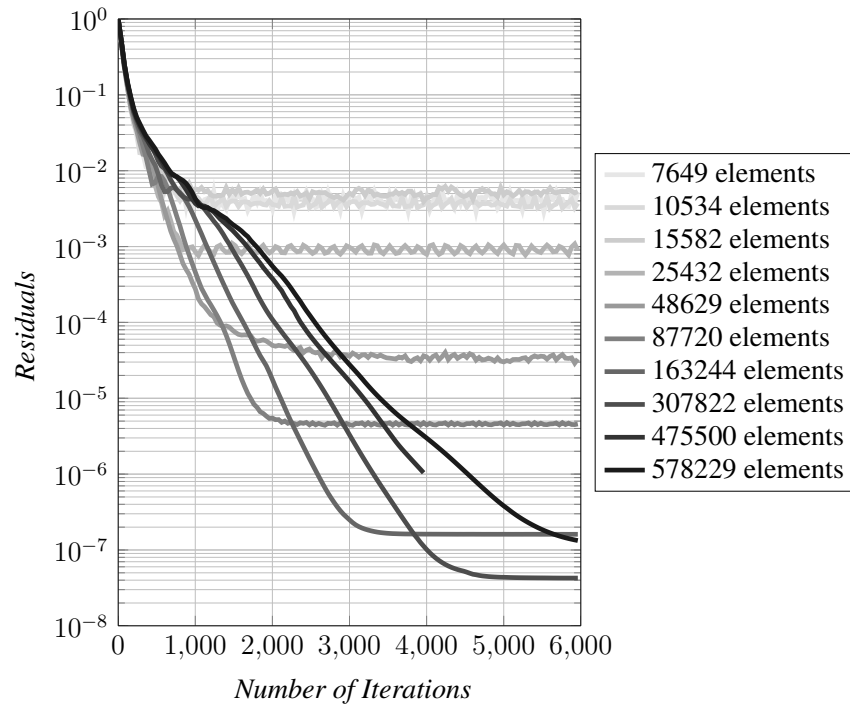


Figure B.8: Solution residuals for ten grids used in the grid convergence study

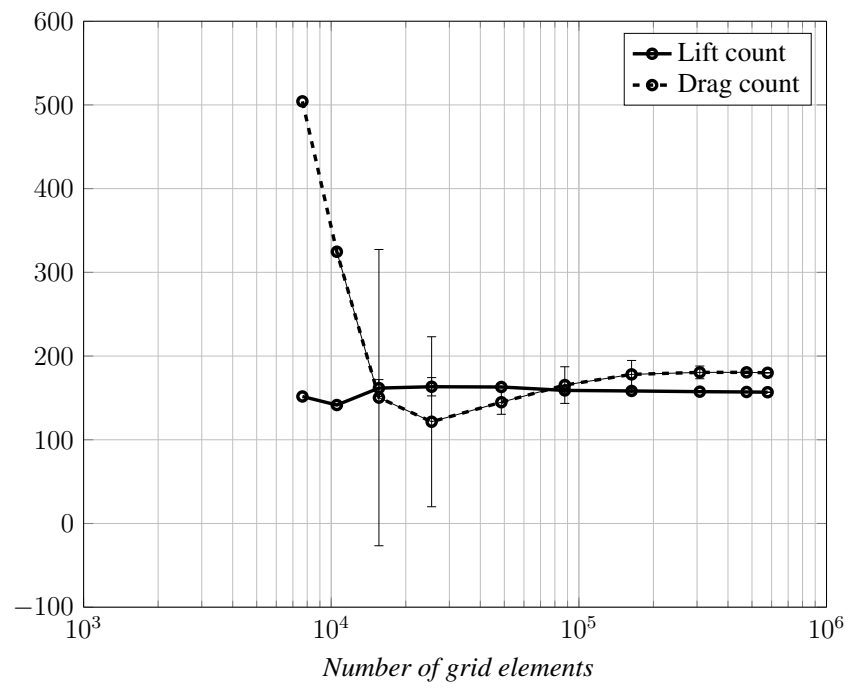


Figure B.9: Grid convergence study for a trawl-door with uncertainty estimation

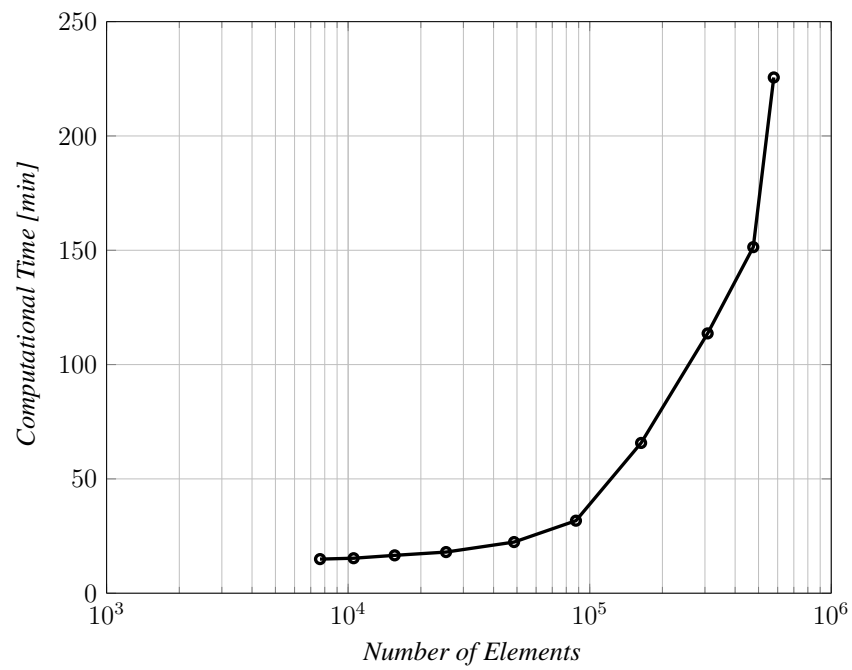
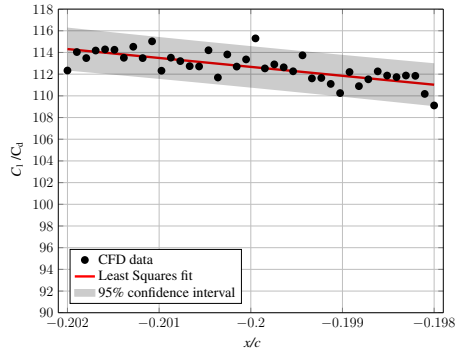


Figure B.10: Computational time as a function of grid density

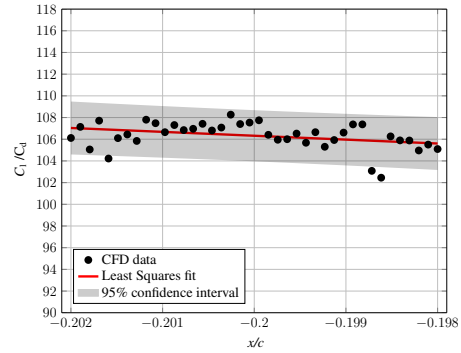
Appendix C

Noise Analysis

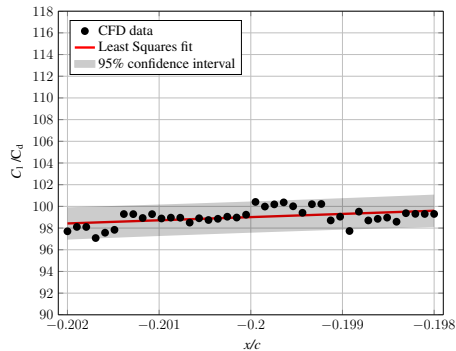
Models in this chapter were considered to have coarse grids, since the level of noise were considerable. The results were obtained according to chapter 3.6, where additional information of the analysis can be found.



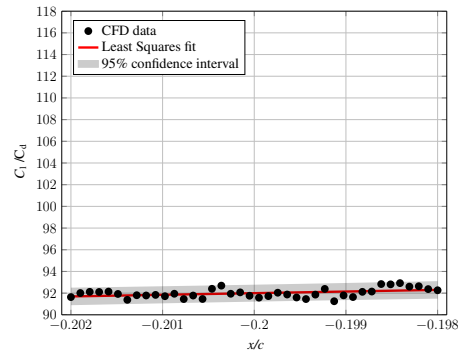
(a) Number of elements ≈ 24.000



(b) Number of elements ≈ 33.000



(c) Number of elements ≈ 42.000



(d) Number of elements ≈ 51.000

Figure C.1: Noise in design variable x/c of the low fidelity model at different grid discretization, the model is considered converged after 1500 iterations or when residuals have reached $5e-3$

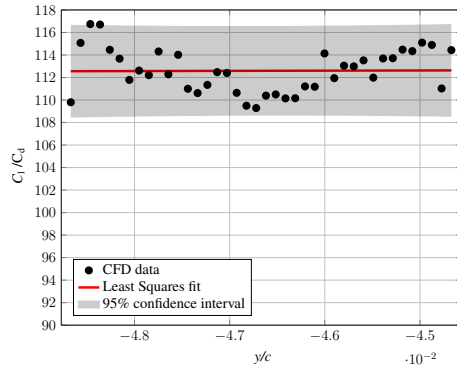
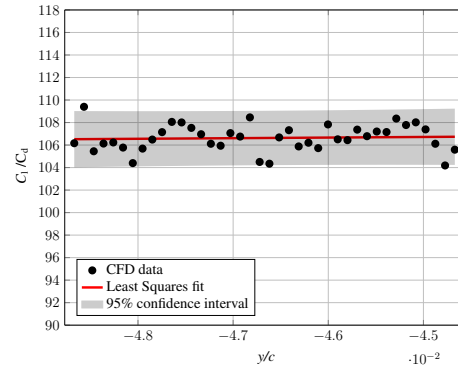
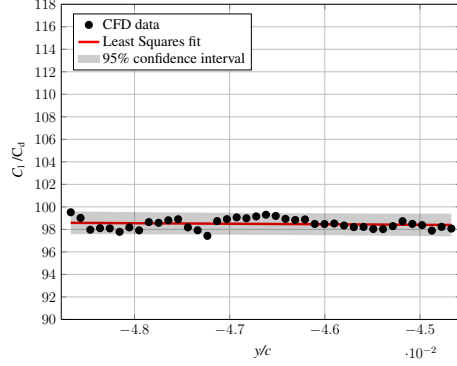
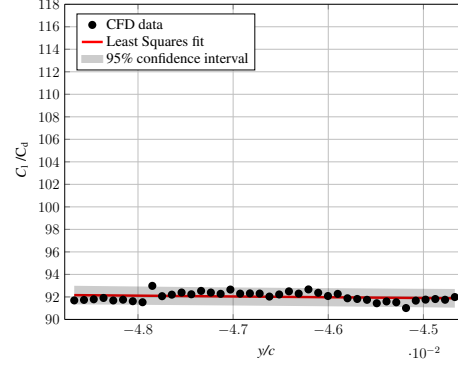
(a) Number of elements ≈ 24.000 (b) Number of elements ≈ 33.000 (c) Number of elements ≈ 42.000 (d) Number of elements ≈ 51.000

Figure C.2: Noise in design variable y/c of the low fidelity model at different grid discretization, the model is considered converged after 1500 iterations or when residuals have reached $5e-3$

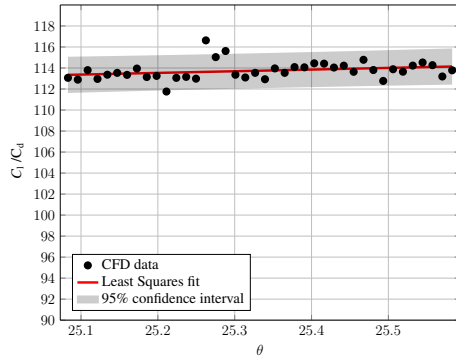
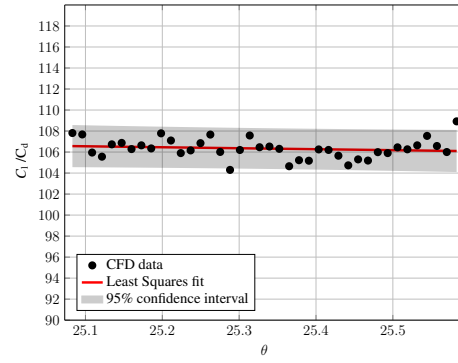
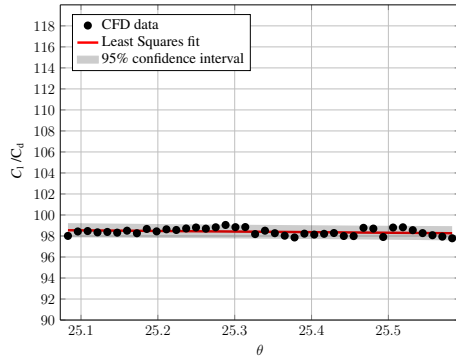
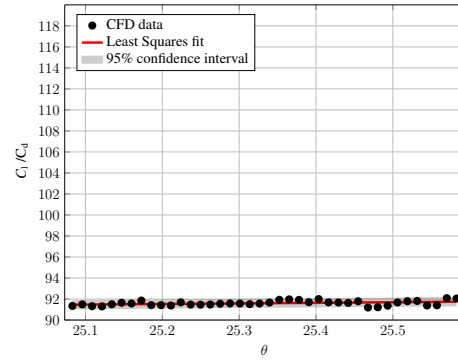
(a) Number of elements ≈ 24.000 (b) Number of elements ≈ 33.000 (c) Number of elements ≈ 42.000 (d) Number of elements ≈ 51.000

Figure C.3: Noise in design variable θ of the low fidelity model at different grid discretization, the model is considered converged after 1500 iterations or when residuals have reached $5e-3$

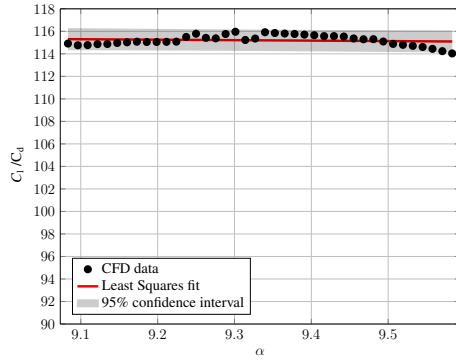
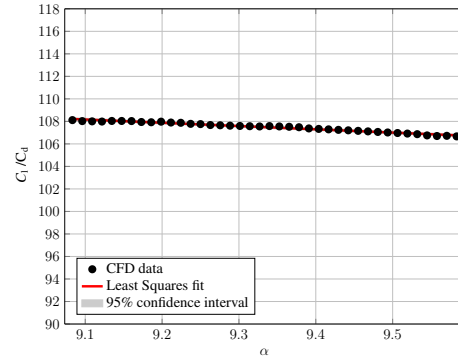
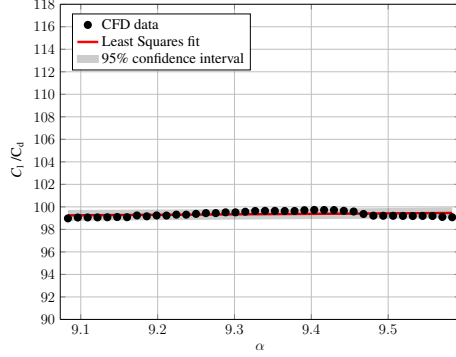
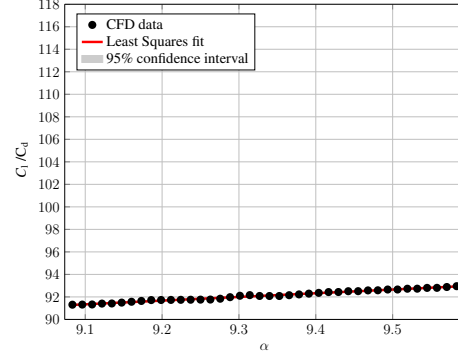
(a) Number of elements ≈ 24.000 (b) Number of elements ≈ 33.000 (c) Number of elements ≈ 42.000 (d) Number of elements ≈ 51.000

Figure C.4: Noise in design variable α of the low fidelity model at different grid discretization, the model is considered converged after 1500 iterations or when residuals have reached $5e-3$

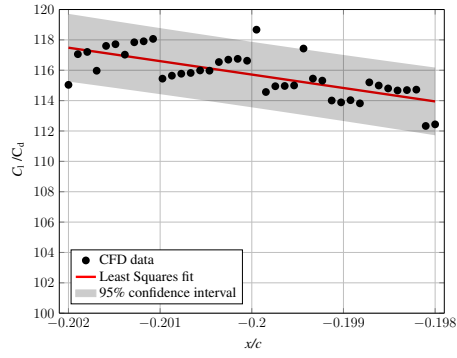
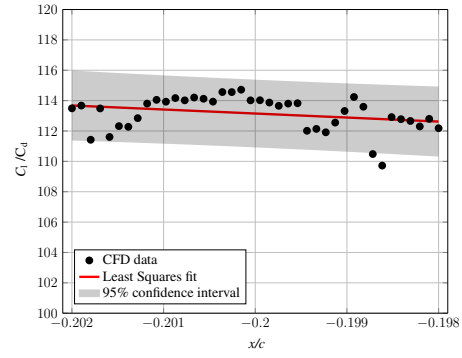
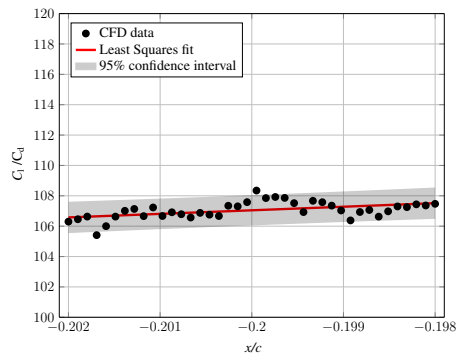
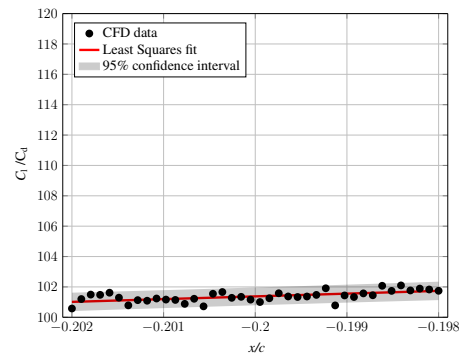
(a) Number of elements ≈ 24.000 (b) Number of elements ≈ 33.000 (c) Number of elements ≈ 42.000 (d) Number of elements ≈ 51.000

Figure C.5: Noise in design variable x/c of the low fidelity model at different grid discretization, the model is considered converged after 2.000 iterations or when residuals have reached $5e-4$

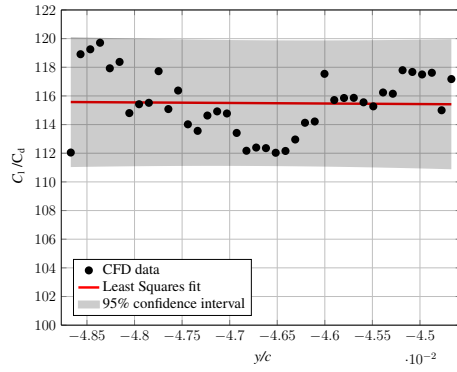
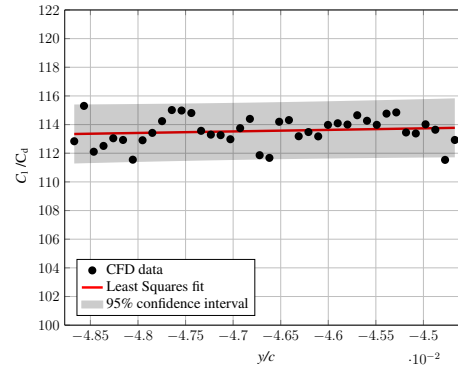
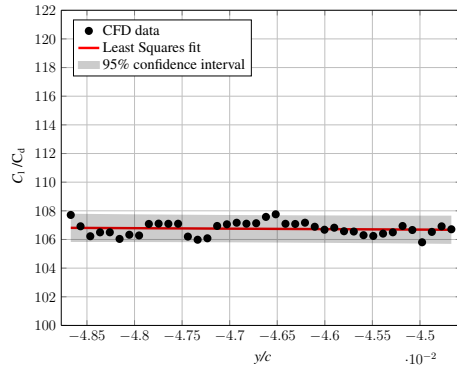
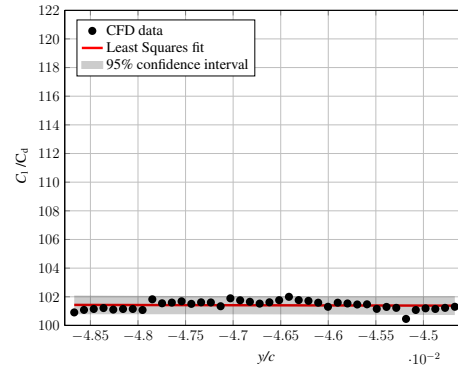
(a) Number of elements ≈ 24.000 (b) Number of elements ≈ 33.000 (c) Number of elements ≈ 42.000 (d) Number of elements ≈ 51.000

Figure C.6: Noise in design variable y/c of the low fidelity model at different grid discretization, the model is considered converged after 2.000 iterations or when residuals have reached $5e-4$

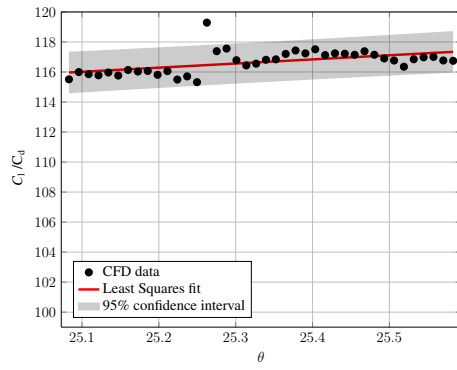
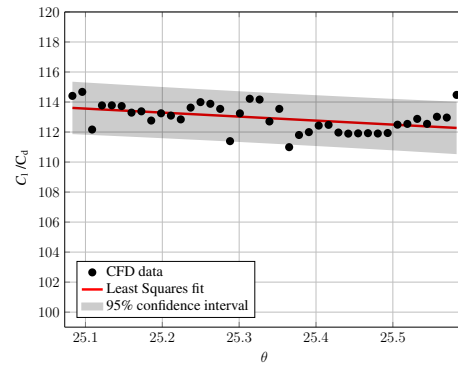
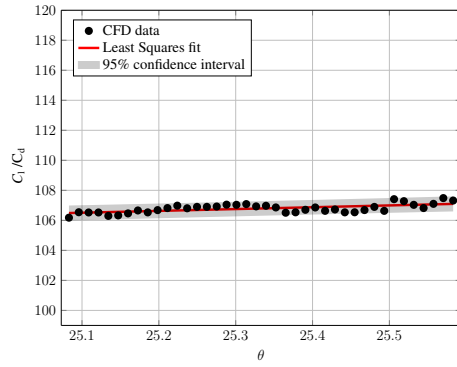
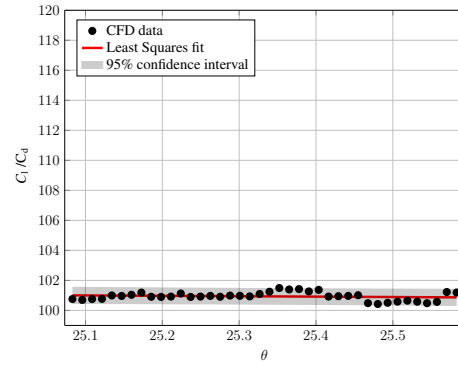
(a) Number of elements ≈ 24.000 (b) Number of elements ≈ 33.000 (c) Number of elements ≈ 42.000 (d) Number of elements ≈ 51.000

Figure C.7: Noise in design variable θ of the low fidelity model at different grid discretization, the model is considered converged after 2.000 iterations or when residuals have reached $5e-4$

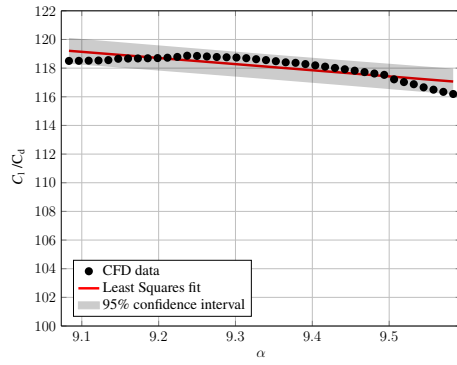
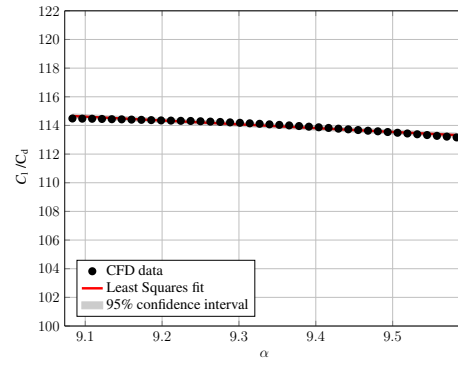
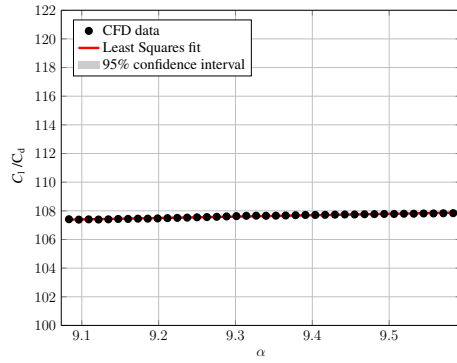
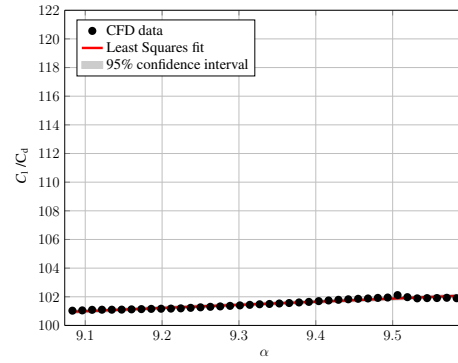
(a) Number of elements ≈ 24.000 (b) Number of elements ≈ 33.000 (c) Number of elements ≈ 42.000 (d) Number of elements ≈ 51.000

Figure C.8: Noise in design variable α of the low fidelity model at different grid discretization, the model is considered converged after 2.000 iterations or when residuals have reached $5e-4$

Appendix D

Additional Validation Data

Validation results shown here are in accordance with methods described in chapter 3.5.

D.1 Model NASA A L1N1WT

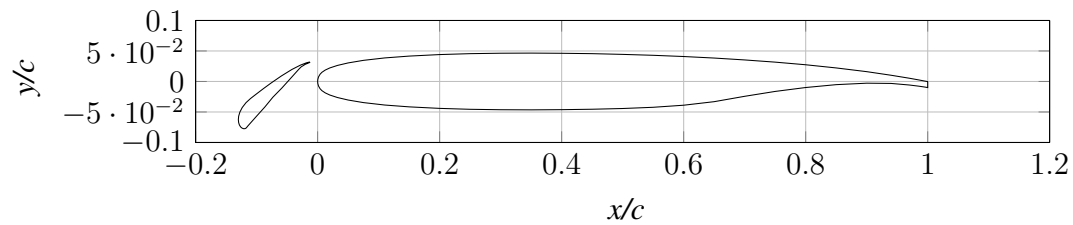


Figure D.1: Geometry of NASA Model A L1N1WT airfoil used for the validation

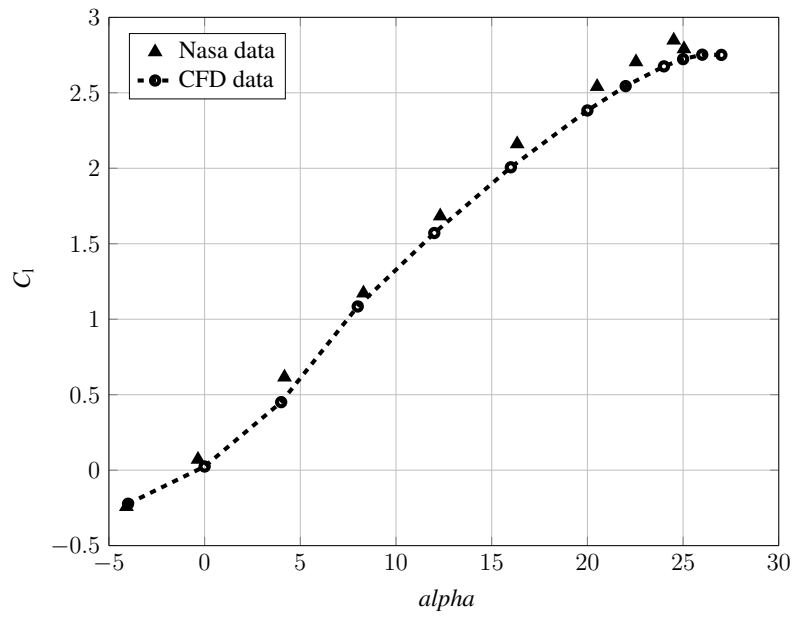


Figure D.2: C_l as a function of α comparison between experimental data using NASA Model A L1N1WT airfoil and the CFD model

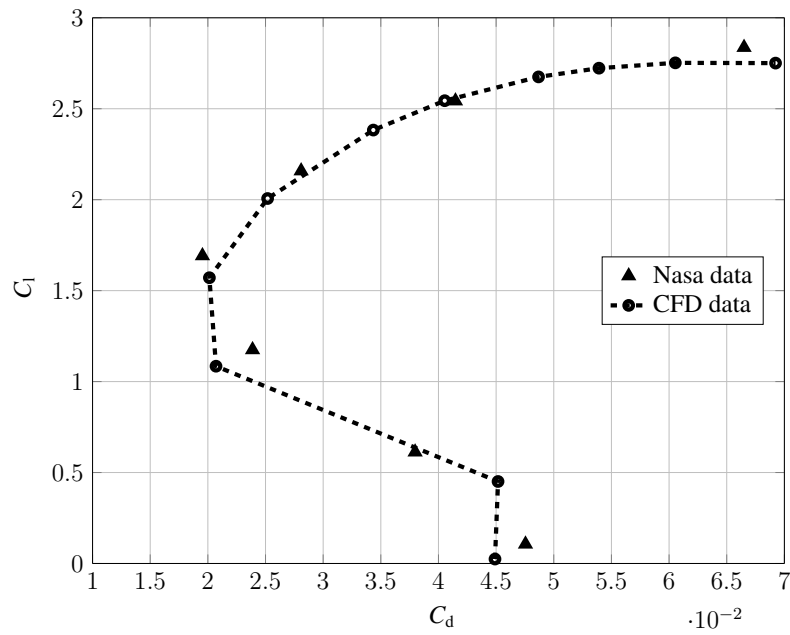


Figure D.3: Drag polar plot comparison between experimental data of NASA Model A L1N1WT airfoil and the CFD model

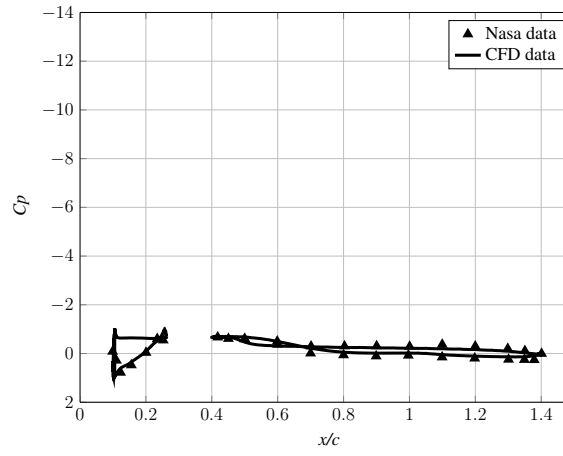
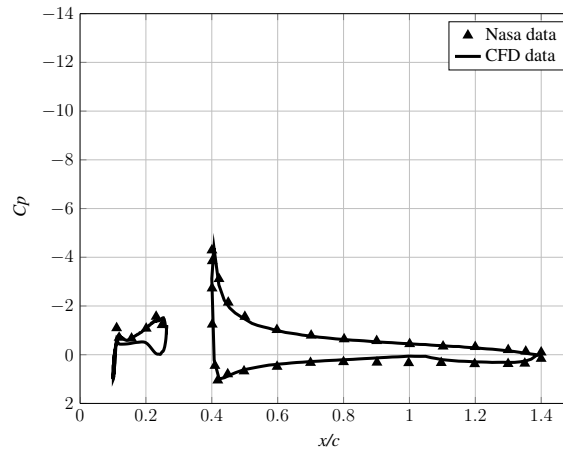
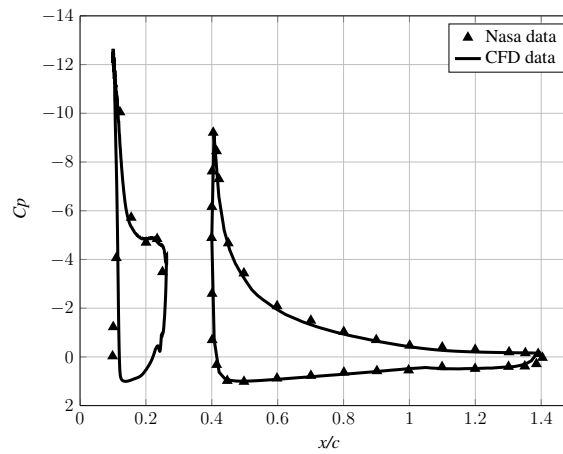
(a) $\alpha = 0^\circ$ (b) $\alpha = 8^\circ$ (c) $\alpha = 27^\circ$

Figure D.4: Comparison between experimental data and the CFD model on pressure coefficient C_p over surface of a NASA Model A L1N1WT airfoil, consisting of a main element and slat at three angles of attack



School of Science and Engineering
Reykjavík University
Menntavegi 1
101 Reykjavík, Iceland
Tel. +354 599 6200
Fax +354 599 6201
www.reykjavikuniversity.is
ISSN 1670-8539